

# ACTA MATERIALIA TRANSYLVANICA

Material Sciences Publications

Volume 4, Issue 1



ERDÉLYI MÚZEUM-EGYESÜLET  
Cluj-Napoca  
2021

A folyóirat megjelenését támogatta a Magyar Tudományos Akadémia, a Bethlen Gábor Alapkezelő Zrt., a Communitas Alapítvány és az EME Műszaki Tudományok Szakosztálya / The publication of this magazine was supported by the Hungarian Academy of Sciences, by the Bethlen Gábor Fund, by the Communitas Foundation and by the TMS – Department of Engineering Sciences.



**Főszerkesztő / Editor-in-Chief:** Bitay Enikő

**Nemzetközi Tanácsadó testület / International Editorial Advisory Board:**

Prof. Biró László Péter, MTA Energiatudományi Kutatóközpont, Budapest, Magyarország  
 Prof. emer. B. Nagy János, University of Namur, Namur, Belgium  
 Prof. Czigány Tibor, Budapesti Műszaki és Gazdaságtudományi Egyetem, Budapest, Magyarország  
 Prof. Diószegi Attila, Jönköping University, Jönköping, Svédország  
 Dobránszky János, MTA–BME Kompozittechnológiai Kutatócsoport, Budapest, Magyarország  
 Prof. Dusza János, Institute of Materials Research of Slovak Academy of Sciences, Kassa, Szlovákia  
 † Prof. Gyenge Csaba, Technical University of Cluj-Napoca, Kolozsvár, Románia  
 † Prof. emer. Gyulai József, Budapesti Műszaki és Gazdaságtudományi Egyetem, Budapest, Magyarország  
 Prof. Kaptay György, Miskolci Egyetem, Miskolc, Magyarország  
 Dr. Kolozsváry Zoltán, Plasmaterm Rt., Marosvásárhely, Románia  
 Prof. Mertinger Valéria, Miskolci Egyetem, Miskolc, Magyarország  
 Prof. Porkoláb Miklós, Massachusetts Institute of Technology, Cambridge, MA, USA  
 Prof. Réger Mihály, Óbudai Egyetem, Budapest, Magyarország  
 Prof. emer. Réti Tamás, Óbudai Egyetem, Budapest, Magyarország  
 Prof. emer. Roósz András, Miskolci Egyetem, Miskolc, Magyarország  
 Dr. Spenik Sándor, Ungvári Nemzeti Egyetem, Ungvár, Ukrajna  
 Prof. Zsoldos Ibolya, Széchenyi István Egyetem, Győr, Magyarország

**Lapszámszerkesztők / Editorial Board:**

Dobránszky János, MTA–BME Kompozittechnológiai Kutatócsoport, Budapest, Magyarország  
 Csavdári Alexandra, Babeş–Bolyai Tudományegyetem, Kolozsvár, Románia  
 Gergely Attila, Sapientia Erdélyi Magyar Tudományegyetem, Marosvásárhely, Románia  
 Kovács Tünde, Óbudai Egyetem, Budapest, Magyarország

**Kiadó / Publisher:** Erdélyi Múzeum-Egyesület

**Felelős kiadó / Responsible publisher:** Biró Annamária

**Olvasószerkesztő / Proofreader:** Szenkovic Enikő (magyar), David Speight (English)

**Szerkesztőségi titkár / Editorial secretary:** Kisfaludi-Bak Zsombor

**Borítóterv / Cover:** Könczey Elemér

**Nyomdai munkálatok / Printed at:** F&F International Kft., Gyergyószentmiklós

**Copyright** © a szerzők / the authors, EME/ TMS 2020

ISSN 2601-1883, ISSN-L 2601-1883

DOI: 10.33923/amt-2021-01

**A folyóirat honlapja:** <https://www.eme.ro/publication-hu/acta-mat/mat-main.htm>

**The journal website:** <https://www.eme.ro/publication/acta-mat/mat-main.htm>

*Acta Materialia Transylvanica. Anyagtudományi Közlemények* az Erdélyi Múzeum-Egyesület (EME) Műszaki Tudományok Szakosztályának folyóirata, amely az anyagtudományok területéről közöl tudományos közleményeket: szakcikkeket, összefoglalókat (szemléket), tanulmányokat. A folyóirat célja összképet adni kiemelten a Kárpát-medencei kutatási irányokról, tudományos eredményeiről, s ezt széles körben terjeszteni is. A folyóirat az EME felváltott céljaihoz híven a magyar szaknyelv ápolását is támogatja, így a nyomtatott folyóirat magyar nyelven jelenik meg, mely az Erdélyi digitális adattárban elérhető (<https://eda.eme.ro/handle/10598/30356>). A széles körű nemzetközi terjesztés érdekében a folyóirat teljes angol nyelvű változatát is közzéteesszük.

*Acta Materialia Transylvanica* – Material Sciences Publications – is a journal of the Technical Sciences Department of the Transylvanian Museum Society, publishing scientific papers, issues, reviews and studies in the field of material sciences. Its mission is to provide and disseminate a comprehensive picture focusing on research trends and scientific results in the Carpathian basin. In accordance with the general mission of the Transylvanian Museum Society it aims to support specialized literature in Hungarian. The printed version of the journal is published in Hungarian and is available in the Transylvanian Digital Database (<https://eda.eme.ro/handle/10598/30356>). However, we would like to spread it internationally, therefore the full content of the journal will also be available in English.

## Tartalom / Content

---

|   |    |
|---|----|
| B. NAGY János .....   | 1  |
| <i>A nanotechnológia múltja, jelene és jövője</i>   |    |
| <i>The Past, the Present and the Future of NanoTechnologies</i>   |    |
| TISZA Miklós .....  | 9  |
| <i>Korszerű, nagy szilárdságú autóiipari acélok fejlesztése</i>   |    |
| <i>Development of Advanced High Strength Automotive Steels</i>  |    |
| BÉRES Gábor J., VÉGVÁRI Ferenc, DANYI József .....  | 18 |
| <i>Nagy szilárdságú acéllemezek és hegesztett terítékek alakítási jellegzetességei</i>  |    |
| <i>Some Formability Aspects of High Strength Steel and of Consisting Tailor Welded Blanks</i>   |    |
| ACÉL Artúr Benjámin, WINDISCH Márk, MALOVECZKY Anna .....   | 24 |
| <i>Vízzáró borítás kialakítása korrózióálló acélfólia lézersugaras hegesztésével</i>  |    |
| <i>Fabrication of a Laser Welded Waterproof Coating Made of Stainless Steel Foil</i>  |    |
| BÍRÓ Tamás, RENKÓ József Bálint .....   | 28 |
| <i>Mikrofluidikai cella tervezése és gyártása spektroszkópiai ellipszométerhez</i>  |    |
| <i>Design and Manufacture of a Microfluidic Cell To Be Used With a Spectroscopic Ellipsometer</i>                                     |    |
| LITAUSZKI Katalin, KMETTY Ákos .....  | 32 |
| <i>Tejsav oligomerrel lágyított, politejsav-alapú biopolimer habok előállítása</i>  |    |
| <i>Production of Biopolymer Foams Based on Polylactic Acid Plasticized With Lactic Acid Oligomer</i>                                  |    |
| NAGY András, JANKOVICS István, MÁTÉ Márton .....  | 38 |
| <i>A szuperkritikus CO<sub>2</sub> erőművi alkalmazásaiban használt, nagy forgássebességű generátorok jövőbeli szerkezeti anyagai</i> |    |
| <i>Future Structural Materials of High Speed Generators Used in Supercritical CO<sub>2</sub> Based Power Plant Applications</i>       |    |
| PÁZMÁN Judit, FEHÉR Jánosné, GONDA Viktor, VERŐ Balázs .....  | 45 |
| <i>Az összetétel és a technológia hatása az EN AW-8006 ötvözet mechanikai tulajdonságaira</i>   |    |
| <i>The Effect of Chemical Composition and Production Technology on the Mechanical Properties of EN AW-8006 Alloy</i>                  |    |

SZABÓ Attila, BÁN Krisztián, HLINKA József, PÁSZTOR Judit, LOVAS Antal ..... 51

*Nagy üvegeképző hajlamú és nagy entrópiájú ötvözetek képződése és stabilitása*

*The Formation and Stability of Bulk Amorphous and High Entropy Alloys*

VIRÁG Ábris Dávid, VAS László Mihály, MOLNÁR Kolos ..... 58

*Üvegszövetek deformációs és tönkremeneteli folyamatának szálkötegcella-elméleten alapuló modellezése*

*Modelling the Deformation and the Failure Process of Glass Woven Fabrics Based on the Fibre-Bundle-Cells Theory*

## A nanotechnológia múltja, jelene és jövője

### The past, the present and the future of nanotechnologies

János B. NAGY

University of Namur, Belgium, [janos.bnagy1@gmail.com](mailto:janos.bnagy1@gmail.com)

#### Abstract

Artists from the time of Mesopotamia or Egypt and in the Middle Ages astonished us with various coloured Stained-glass windows, prepared with the help of metal nanoparticles.

The paper will deal with zeolites, nanoparticles and carbon nanotubes. The latter will be developed more extensively, because we have founded the Nanocyl company, selling carbon nanotubes and it has become the best European company. One carbon nanotube is 100,000 times thinner than a human hair, it is very light – twice as light as aluminium –, its mechanical resistance is much higher than that of steel and it conducts electricity better than metal conductors. The use of carbon nanotubes is very important in nanotechnology. For example, with the help of coiled carbon nanotubes, the weight of a single nanoparticle can be measured, it is equal to one femtogram ( $10^{-15}$  gram). Carbon nanotubes are used in car spray painting to cancel the build-up of static electricity. With the help of carbon nanotubes, it is possible to decrease the velocity of flame propagation, when they are included in composite materials. Carbon nanotubes are also very good as sensors for toxic gases. Their uses will take up the most part of this paper.

The future of nanotechnology will be illustrated by nanomachines, by the lift between the Earth and the Moon, and by graphene (one single sheet of graphite). The use of carbon nanotubes will be evoked in waste water cleaning, in the production of drinking water from seawater.

**Keywords:** nanoparticles, carbon nanotubes, coiled carbon nanotubes, nanotechnology.

#### Results and discussion

Nanoparticles have two essential properties: the very high surface area and the physical properties that depend on the size of the particles.

**Figure 1.** illustrates the importance of the surface area. Let us start with a cube of 1 m edge. This gives a surface area of  $6 \text{ m}^2$ . If we divide the edge by 1,000, we get a cube of  $1 \text{ mm}^3$  with a surface of  $6 \text{ m}^2$ . As we can form 1,000,000,000 cubes from the initial one - the total volume being kept constant – the total surface becomes equal to  $(6 \times 10^9) \text{ m}^2$  or  $6,000 \text{ m}^2$ .

If we continue to divide by 1,000,000,000 we arrive at cubes each of  $1 \text{ nm}$  edge. The total surface area becomes in this case  $6,000,000,000 (6 \times 10^9) \text{ m}^2$ .

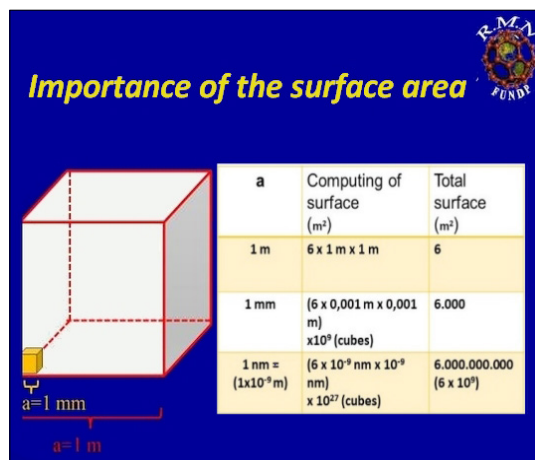


**Figure 1.** The importance of the surface area.

As a consequence, the total surface increases always by the same amount as the number used to divide the initial edge.

The change of the physical properties is illustrated in **Figure 2**.

This shows the change of colour of the fullerenes – which are balls formed only by carbon atoms – as a function of their size [1].

The zeolites are aluminium silicates either in natural or in synthesized form [2]. They are composed of cavities and channels of nanoscopic size (**Figure 3**). They are used as adsorbents, as ionic exchanger due to the presence of cations neutralizing the negative charges linked to aluminium and as catalyst. Those who drive a car can be sure that their gasoline has seen zeolites in their life as they are used to cut the long chains of the molecules composing the crude petroleum.

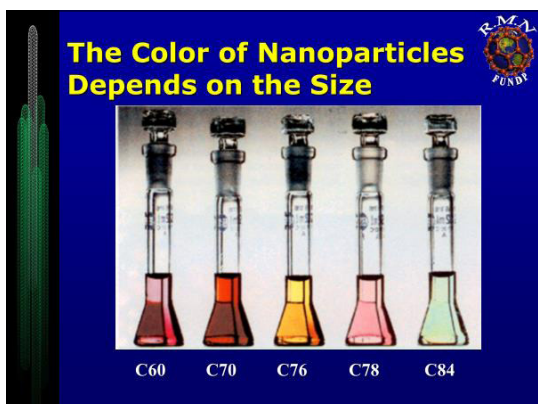


**Figure 2.** The colour of nanoparticles depends on their size.



**Figure 3.** Natural and synthesized zeolites.

Inorganic nanoparticles can be prepared by reducing the cations dissolved in microemulsions formed by three components, water, surfactant and organic solvent [3]. The water dispersed in the organic solvent – thanks to the surfactant – forms nanocages where the reaction of reduction occurs and the so-formed nano-particles are stabilized by the surfactant.

**Figure 4**, represents the formation of AgBr nanoparticles in two different conditions. In the first case a kinetic control takes place and the colliding nanoparticles form a fractal structure (in black in the figure). In the second case, thermodynamic control occurs and the nanoparticles tend to form a more stable structure, i.e. a sphere. The reaction has not completely finished and as an intermediate state a heart-like structure is formed (in red in the figure). This figure could finally be red as „I love nano-particles”.

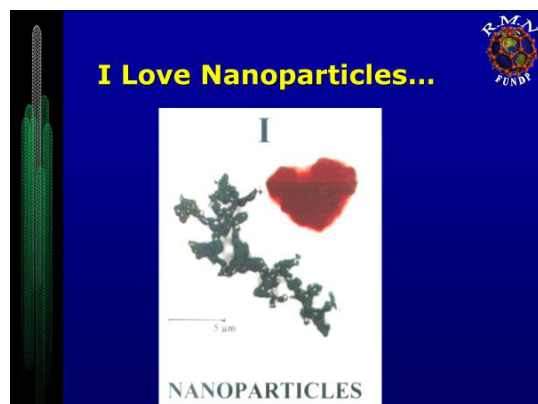


**Figure 4.** AgBr nanoparticles forming a fractal structure (in black) and controlled by thermodynamic stability tending to a spherical form (in red).



**Figure 5.** Stained – glass windows of the Middle Age (Sainte Chapelle, Paris, XII. Century).

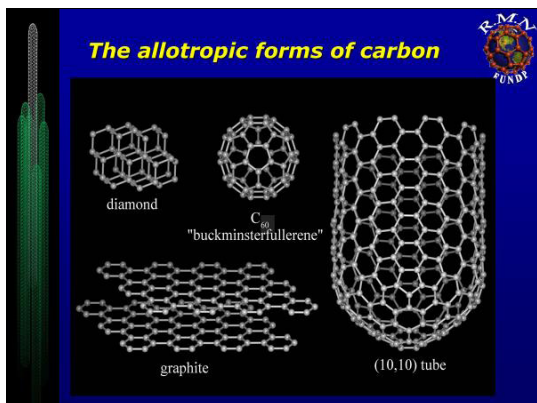


Figure 6. The allotropic forms of carbon.

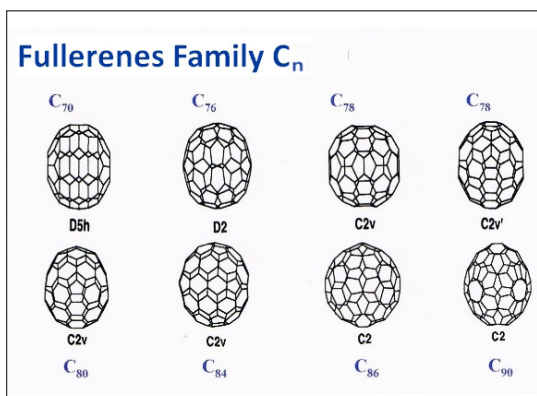


Figure 7. Fullerenes family.

As the past of nanotechnology, we show a beautiful picture composed of nano-particles of silver (giving the yellow colour) and of copper (giving the red colour) leading to the stained – glass windows in the Middle Age (Figure 5).

This is proof that nanotechnology was discovered prior to the twentieth century.

Figure 6. shows the various allotropic forms of carbon.

Diamond is formed by a tetrahedral structure linking every carbon atom. It has a beautiful colour and is one of the hardest materials. When all the carbon atoms are linked to three other neighbours, a plane structure is obtained formed by six - membered rings. This is graphite, and it is quite breakable, because the planes can slip over each other. We know this from the way a pencil usually breaks easily. Fullerenes are balls formed only from carbon atoms and the carbon nano – tubes were initially considered as elongated fullerenes.

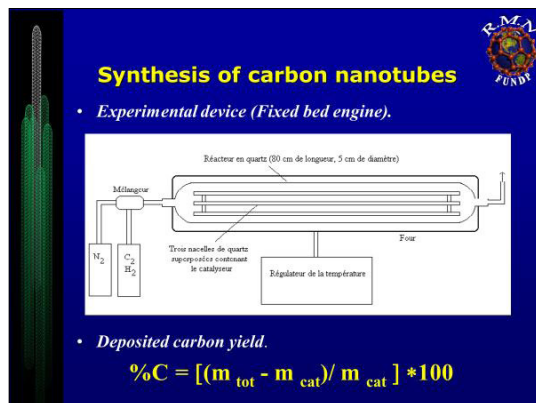


Figure 8. Synthesis of carbon nanotubes by Chemical Vapour Deposition.

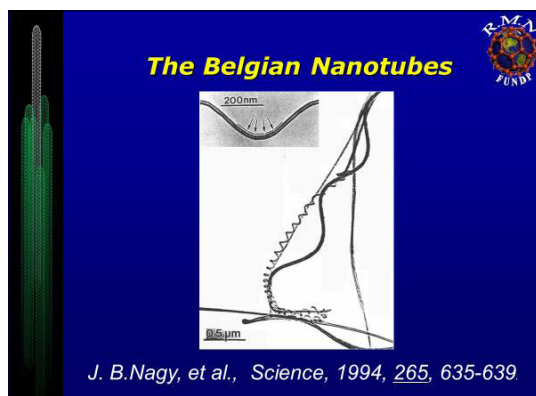


Figure 9. The Belgian nanotubes: Nanoharp.

Figure 7. Illustrates some members of the fullerenes family [4].

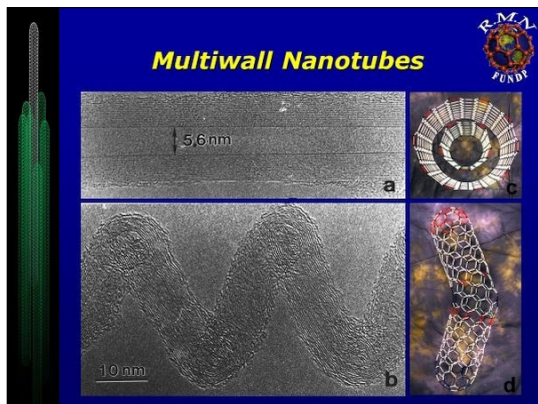
Bob Curl, Harry Kroto and Rick Smalley received the Nobel Prize in chemistry in 1996 for the discovery of C<sub>60</sub> fullerenes.

The main part of the paper will be occupied by the synthesis and use of carbon nanotubes.

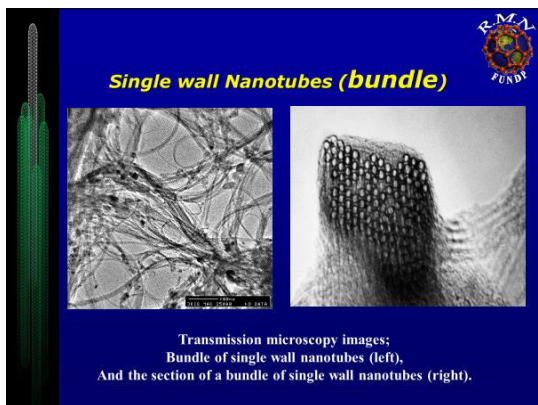
We used a very simple method to prepare carbon nanotubes. A hydrocarbon, for example acetylene, is decomposed on supported metal nanoparticles at high temperature, i.e. 700 °C. The generally used metal particles are Fe, Co or Fe – Co, supported on various solids such as zeolites or silica gel. The method is called Catalytic Vapour Deposition (CVD) (Figure 8).

Figure 9. shows various multiwalled carbon nanotubes obtained on a Co/silica catalyst. We can see linear nanotubes and coiled nanotubes [5].

The figure could represent a „nanoharp”.



**Figure 10.** High resolution Transmission Electron Microscope (TEM) pictures of Multi Walled Nanotubes (MWNT) in the linear form and in the coiled form.



**Figure 11.** Single Walled Nanotubes (SWNT) forming bundles.

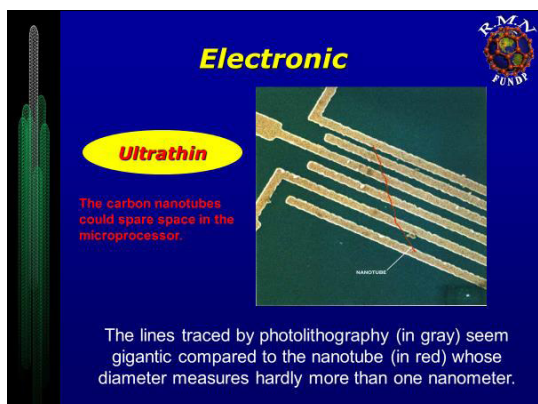


**Figure 12.** The very thin size of Single Walled Carbon Nanotubes

**Table 1.** Properties of Single Walled Carbon Nanotubes.

| Nanotube Properties  |  |  |  |
|--|--|--|--|
| Properties   | SWNTs  | For memory   |  |
|  <b>SIZE</b>              | 0.6 to 1.8 nm in diameter.   | The lithography by electron beam can create broad lines of 50 nm and of some nm of thickness.                |  |
|  <b>DENSITY</b>           | 1.33 to 1.40 g/cm <sup>3</sup> .   | Aluminium has a density of 2.7 g/cm <sup>3</sup> .   |  |
|  <b>STRENGTH</b>          | 45 billion Pascal.   | The strongest steel alloys break at approximately two billions of Pascal.                                    |  |
|  <b>ELASTICITY</b>        | They can be strongly curved without irreversible deformation.  | Metals and the carbon fibers are fractured at the limits between the grains.                                 |  |
|  <b>CURRENT TRANSPORT</b> | Estimated at one billion A/cm <sup>2</sup> .   | The copper wire roasts at approximately one million A/cm <sup>2</sup> .                                      |  |
|  <b>FIELD EMISSION</b>    | They can activate phosphorus with a tension ranging between 1 and 3 volts when the electrodes are distant by 1 μm. | Molybdenum tip requires electric fields from 50 to 100 volts per micrometer and have very limited life time. |  |
|  <b>HEAT TRANSFER</b>     | It would be 6000 W/m.K at ambient temperature.   | A quasi pure diamond transmits 3320 W/m.K.   |  |
|  <b>THERMAL STABILITY</b> | Stable up to 2800 ° C in vacuum and to 450 ° C in air.   | The metal wire of micro chips melts between 600 and 1000 ° C.  |  |

**Figure 10.** illustrates a high resolution transmission electron microscope picture of a coiled multiwalled carbon nanotube. The tube is formed by some 10 concentric layers. The coiled carbon nanotubes were called « Belgian tubes » by Japanese and South – Korean scientists as we synthesized them for the first time. We have founded the Nanocyl company in order to prepare various carbon nanotubes in large amounts.

Single walled carbon nanotubes can also be prepared and they form bundles, because the van der Waals attraction is very high between the tubes (**Figure 11.**).

The carbon nanotubes can be used in nanotechnology. They are thinner than the frame obtained by lithography and one can put many more electric conductors in the same volume (**Figure 12.**).

**Table 1.** compares the various properties of carbon nanotubes with other known materials. They are thinner than the wire made by silicon to be used in computers.

They are twice as light as the corresponding light metal aluminium used in aeroplane parts. They are more resistant than steel and they conduct electricity better than known metallic conduc-

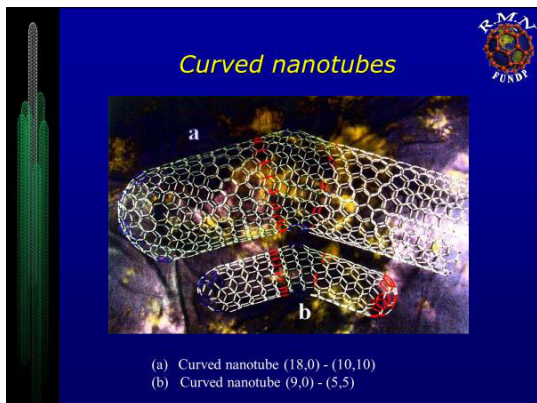


Figure 13. Curved nanotubes.

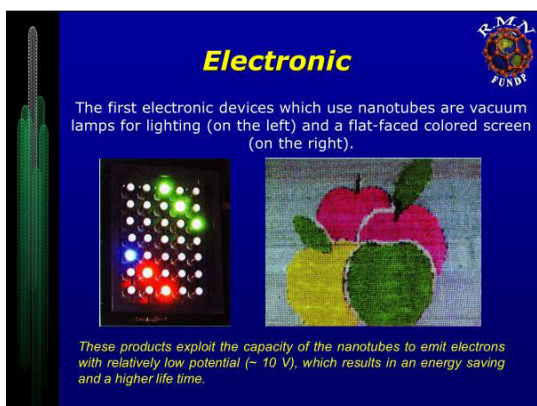


Figure 14. Light emitting properties of carbon nanotubes.

tors. They emit electrons easily and are already used in car painting in order to reduce the static electricity on the surface. They are very flexible, and they come back to the initial position after cancelling the initial force. Their heat transfer is twice as good as the best material known so far. The thermal stability is high in vacuum, stable up to 2,800 °C, but in air it is oxidized at 450 °C. It should be noted that metal microchips melt between 600 °C and 1,000 °C.

Figure 10. also shows models to illustrate the two concentric layers in a MWNT. Let us concentrate now on the curved nanotubes of Figure 13. We can distinguish clearly two different structures formed by the six – membered rings. When the sides of the six – membered rings are perpendicular to the tube axis, it is a metal conductor, while when the sides of the six – membered rings are parallel with the tube axis, it is a semi – conductor. This curved nanotube can hence be used in nanotechnology, as a switch, letting the current

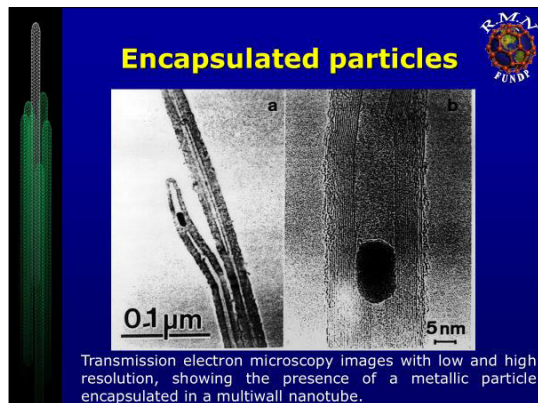


Figure 15. Encapsulated particles.

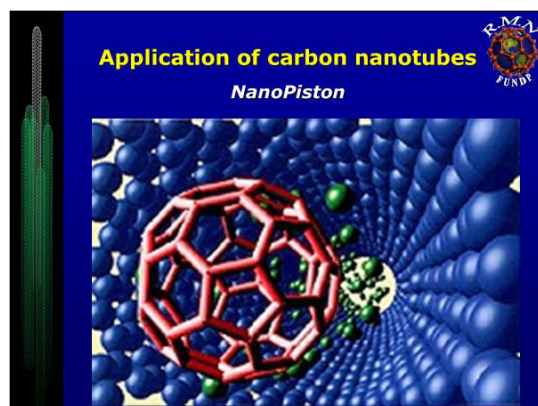
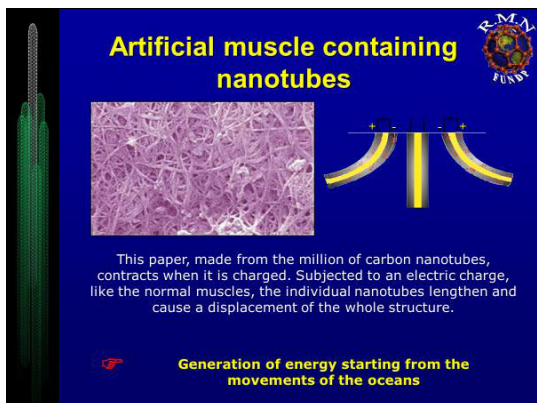


Figure 16. NanoPiston

pass in one tube and cutting it in the other.

The electron emitting properties can be used in vacuum lamps for lighting and in a flat – faced coloured screen (Figure 14.). Indeed, the first lamps used carbon fibres, but they had only a short life, that is why one replaced them by tungsten used until recently. Nowadays, one could come back to carbon, because the lifetime of carbon nanotubes is much longer.

Metal particles used as catalysts are sometimes encapsulated in the nanotube (Figure 15.). In addition, the figure shows that the end of the nanotube is closed. We have to open the nanotube by gentle oxidation and this way we can use them as sorbents. Hence, we can eliminate toxic gases, and for example, the carbon nanotubes adsorb dioxine 1,000 times better than the adsorbents known at present. In the open form, nanotubes are also used as sensors because their electric conductivity depends not only on the nature of the gases, but also on their quantity.



**Figure 17.** Artificial muscle containing carbon nanotubes.

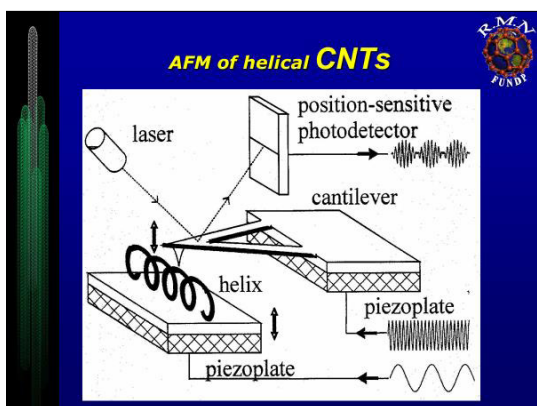


**Figure 18.** Atomic Force Microscopy of helical MWNTs.

Carbon nanotubes can also be used as a Nanopiston. **Figure 16.** Illustrates the Nanopiston functioning, where a fullerene molecule pushes the other molecules in the internal tube of a MWNT.

With the help of the carbon nanotubes, it is possible to realize an artificial muscle (**Figure 17.**).

Two sheets formed by carbon nanotubes are attached on an isolating plastic sheet. Into one sheet, a positive charge is introduced – hence the valence bond lengths are decreased -, while into the other, a negative charge is introduced – hence the valence bond lengths are increased. This provokes a bending imitating the movement of a muscle. Conversely, one could generate electricity by bending the sheet suspended in the sea. This experiment has already been realized near Lisbon in Portugal.

It is also possible to write on a silicon plate using carbon nanotubes, this is thus the NanoPencil [6].

We made the first NanoBalance using helical or coiled carbon nanotubes (**Figures 18.** and **19.**).

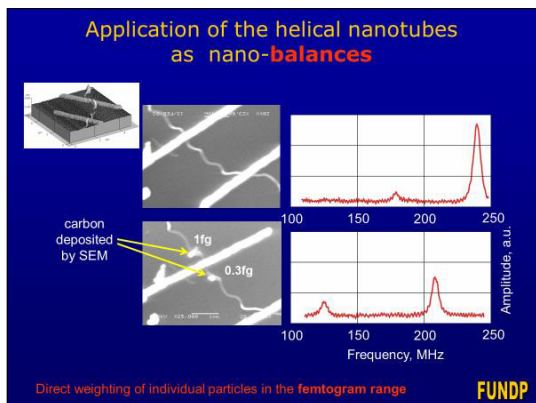


**Figure 19.** Use of helical carbon nanotube as a Nano-Balance.



**Figure 20.** Dispersion in polymeric chains.

A coiled multiwalled carbon nanotube is deposited on the piezo plate of the Atomic Force Microscopy. With the tip of the cantilever one taps on the nanotube (**Figure 18.**). The basic frequencies in MHz are registered (**Figure 19.**).

When a nanoparticle is deposited on the coiled carbon nanotube, the basic frequencies are diminished due to the weight of the nanoparticle. From the differences in the frequencies it is possible to compute the weight of a single nano-particle: it is in the femtogram range ( $10^{-15}$  g).

It is also possible to make a NanoSpring using coiled carbon nanotubes, by attaching one end to a fixed material [7]. One can measure the elastic modulus of the tube that is in the TPa range. Introducing current into a coiled nanotube, quite large magnetic fields can be induced leading to a NanoSolenoid [8].

The preparation of composite materials is very interesting. The dispersion of the nanotubes should be as good as possible in order to increase

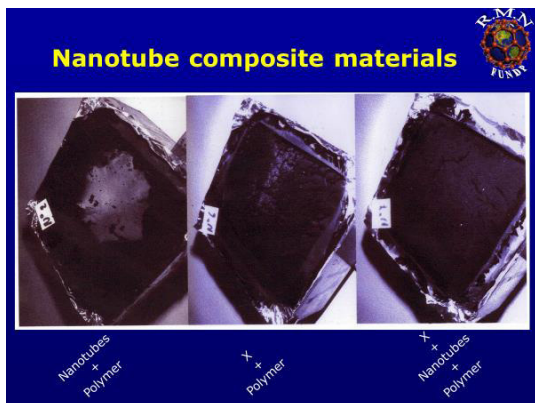


**Figure 21.** Flame retardant properties of composite materials.

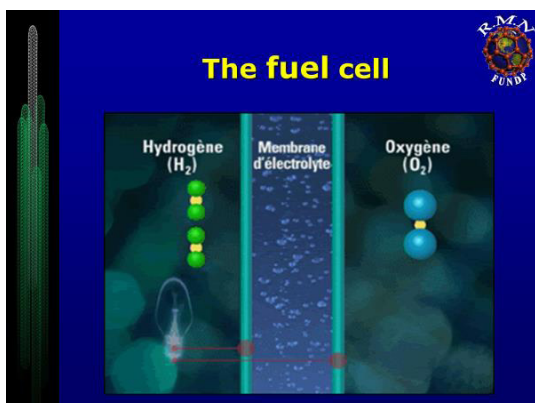


**Figure 22.** The fuel cell where the electrolyte membrane contains carbon nanotubes.

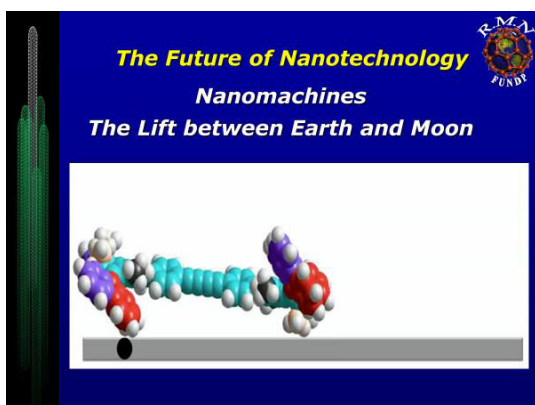


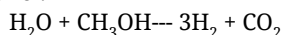
**Figure 23.** The future of nanotechnology.

the interaction between the polymeric chains and the nanotubes (Figure 20.) [9].

The presence of nanotubes is also responsible for the flame – retardant properties of the composite material. The carbon nanotubes dispersed alone in the polymer have no flame – retardant properties (Figure 21. left picture). When some layered silicate is added to the polymer, the flame – retardant property is improved (Figure 21. middle picture). However, when both carbon nanotubes and layered silicate are dispersed, the result due to synergistic effects is excellent (Figure 21. right picture) [10].

Carbon nanotubes are also used in fuel cells where the membrane is composed of carbon nanotubes favouring the transfer of the hydrogen atoms towards the oxygen molecules that are reduced, thereby producing electric current (Figure 22.). These fuel cells are becoming increasingly important, because electric cars help to reduce CO<sub>2</sub> content in the air.

Hydrogen can be directly produced by a heterogeneous catalytic reaction between water and methanol:



The future of nanotechnology can be illustrated by the nanomachine formed by Prof. Jean – Pierre Sauvage, Nobel Prize in Chemistry in 2016 and the lift between Earth and Moon imagined by Rick Smalley, Nobel Prize in Chemistry in 1996 (Figure 23.).

The physics and chemistry of graphene (one single graphite sheet) are developing fast and are very promising. New sensors are found to detect the toxic gases. The use of carbon nanotubes in purifying waste waters is increasing in the scientific literature [11], as well as their use in preparing drinking water from sea water [12].

## Conclusions

Nanoparticles were used in ancient times to prepare, for example, various coloured stained – glass windows.

The endless applications of carbon nanotubes include nanoelectronics, nanosolenoids, nanosprings, nanobalances, flat – faced screens, composite materials, sensors, fuel cells...

The future of nanotechnology deals with nanomachines, graphene and its application, including water purification

## References

- [1] Baggott J.: *Perfect symmetry. The accidental discovery of Buckminsterfullerene*. Oxford University Press, 1996.

- [2] For a short introduction see B. Nagy J., Bodart P., Hannus I., Kiricsi I.: *Synthesis, characterization and use of zeolitic micro – porous materials*. Deca-Gen Ltd., Szeged, Hungary, 1998.
- [3] B. Nagy J., Barette D., Fonseca A., Jeunieu L., Monnoyer Ph., Piedigrosso P., Ravet-Bodart I., Verfaillie J.-P., Whatelet A.: *Nanoparticles in microemulsions: a general approach*. In: *Nanoparticles in solids and solutions*. (eds: Fendler J. H., Dékány I.) NATO ASI Series, 3. High Technology – Vol. 18. Kluwer Academic Publishers, Dordrecht, 1996.
- [4] *In Building on fullerenes*. Nature, 363. (1993) 60–63.
- [5] Amelinckx S., Zhang X.B., Bernaerts D., Zhang X. F., Ivanov V., B. Nagy J., Lucas A. A., Lambin Ph.: *A formation mechanism of catalytically grown helix shaped graphite nanotubes*. Science, 265. (1994) 635–639.
- [6] Dai H., Franklin N., Han J.: *The high aspect – ratio nanopencil takes advantage of the small nanotube electrode size*. Applied Physics Letters, 73. (1998) 1508–1510.
- [7] Bernaerts D., Zhang X. B., Zhang X. F., Amelinckx S., Van Tendeloo G., Van Landuyt J., Ivanov V., B. Nagy J.: *Electron microscope study of coiled carbon tubules*. Philosophical Magazine A, 71. (1995) 605–630.
- [8] Volodin A., Van Haesendonck C., Terbiainen R., Ahlskog M., Fonseca A., B. Nagy J.: *AFM detection of mechanical resonances of coiled carbon nanotubes*. Applied Physics, A72. [Suppl] (2001) S75–S78.
- [9] Coleman J. N., Cadek M., Blake R., Nicolosi V., Ryan K. P., Belton C., Fonseca A., B. Nagy J., Gun'ko Y. K., Blau W. J.: *High-performance nanotube-reinforced plastics understanding the mechanism of strength increase*. Advances in Functional Materials, 14 /8. (2004) 791–798.
- [10] Peeterbroeck S., Alexandre M., B. Nagy J., Pirlot C., Fonseca A., Moreau N., Destrée A., Philippin G., Delhalle J., Mekhalif Z., Sporken R., Beyer G., Dubois Ph.: *Polymer – layered silicate – carbon nanotube nano-composites: unique nanofiller synergistic effect*. Composites Science Technology, 64. (2004) 2317–2323.
- [11] De Luca P., B. Nagy J.: *Treatment of water contaminated with Reactive Black-5 Dye by carbon nanotubes*. Materials, 13. (2020) 5508. <https://doi.org/10.3390/ma13235508>.
- [12] Grosso V., Vuono D., Bahattab M. A., Di Profio G., Curcio E., Al-Jilil S.A., Alsubaie F., Alfife M., B. Nagy J., Drioli E., Fontananova E.: *Polymeric and mixed matrix polyimide membranes*. Separation Purification Technology, 132. (2014) 684–696.

# Development of Advanced High Strength Automotive Steels

Miklós TISZA

*University of Miskolc, Faculty of Mechanical Engineering, Institute of Materials Science and Engineering, Miskolc, Hungary, [tisza.miklos@uni-miskolc.hu](mailto:tisza.miklos@uni-miskolc.hu)*

---

## Abstract

In recent decades, the automotive industry has faced ever-increasing demands. Increasing requirements can be observed in terms of both consumer expectations and legal requirements. On the consumer side, there is a demand for cars that are as economical as possible with lower fuel consumption, but providing also greater comfort and safety. These requirements are accompanied, from a legal point of view by more rigorous environmental regulations and requirements concerning the reduction of harmful emissions. Meeting these often-contradictory requirements is a growing challenge for car manufacturers and raw material suppliers, as well. Meeting the requirements in the most versatile way has resulted in tremendous progress over the last 40-50 years, both in the automotive industry and in the production and development of raw materials. The first part of this series of papers summarizes the main requirements in the automotive industry, as the main driving forces for material developments. Furthermore, the main types and properties of traditional high-strength steels, as well as the so-called first-generation Advanced High-Strength Steels will be introduced. In the second part, the main types and manufacturing processes of second generation advanced high-strength steels will be analyzed and some of the current steel developments will be presented through the results of the three generations of Advanced High-Strength Steels.

**Keywords:** *Advanced High Strength Steels, AHSS, automotive industry applications.*

---

## 1. Introduction

Due to the increasing global competition in the automotive industry, reducing the manufacturing costs is a key objective: this is closely linked to reducing the weight of vehicles for a number of reasons.

Mass reduction in car manufacturing is also at the heart of research activities internationally. This can be explained by a number of factors, some of which are highlighted here: due to the ever increasing strict emission standards and environmental restrictions, vehicle weight reduction plays a key role in meeting consumer demands for cars that can be operated as economically as possible.

Regarding the total weight of a car, the car body plays a crucial role. The body parts – the so-called Body-in-White – in the manufacture of sheet metal forming is one of the most important manufacturing processes. This also justifies the development of new, innovative, low-cost manufacturing

processes in sheet metal forming as well. The two main directions in the production of lightweight automotive components are the use of high-strength steels and light metals, with a particular emphasis on various high-strength aluminium alloys [1].

In this paper, we focus on the development of high-strength steel materials and the results of these developments. This several decades-long development activity is best characterized by the development results of advanced high-strength steels, which appear in the international literature as AHSS, so we will often use the commonly accepted short designation in this work.

Developments in this area can be clearly defined into three major groups, namely the so-called first, second and third generation advanced high-strength steels. These developments are also closely related to the requirements of the automotive industry, which are also the driving forces behind material developments.

## 2. Driving forces in car manufacturing

The main driving forces of material development in the automotive industry are from the one hand the consumer expectations (more economical, safer, more comfortable cars, with better performance); on the other hand, it is supplemented by several legal requirements (more rigorous environmental standards, lower emissions, increased crash test standards).

These two large groups represent partly similar and partly contradictory requirements. Due to global competition, the automotive industry needs to find appropriate responses for these challenges. Developments in recent decades have clearly shown that weight reduction plays a key role in meeting this diverse set of requirements.

Considering the proportion of different structural elements in the total weight of cars, it can be concluded that the reduction of the weight of Body-in-White elements, the various chassis and suspensions – i.e. the sheet parts – plays a key role. Reducing the weight of the sheet metal components requires the reduction in the thickness of the sheet materials and thus an increase in strength.

However, an increase in strength is usually accompanied by a decrease in formability, which in turn raises fundamental technological problems. Steel developments in recent decades have sought to balance these contradictory requirements, i.e. to develop high-strength steels that also meet the needs of the automotive industry in terms of formability.

### 2.1. Classification of automotive steel developments

The most commonly used classification in steel development in recent decades – the so-called Advanced High Strength Steels (AHSS) grouping – distinguishes three main groups, namely, first, second and third generation high strength steels. This classification is illustrated graphically in **Figure 1**. This figure also shows the well-known regularity of metallic materials, according to which, as the strength increases, the deformability decreases following a hyperbolic relationship. This is illustrated by the  $R_m \times A_{80} = C$  (constant) curves showing the product of tensile strength and total elongation, which play an important role in the classification of advanced high-strength steels.

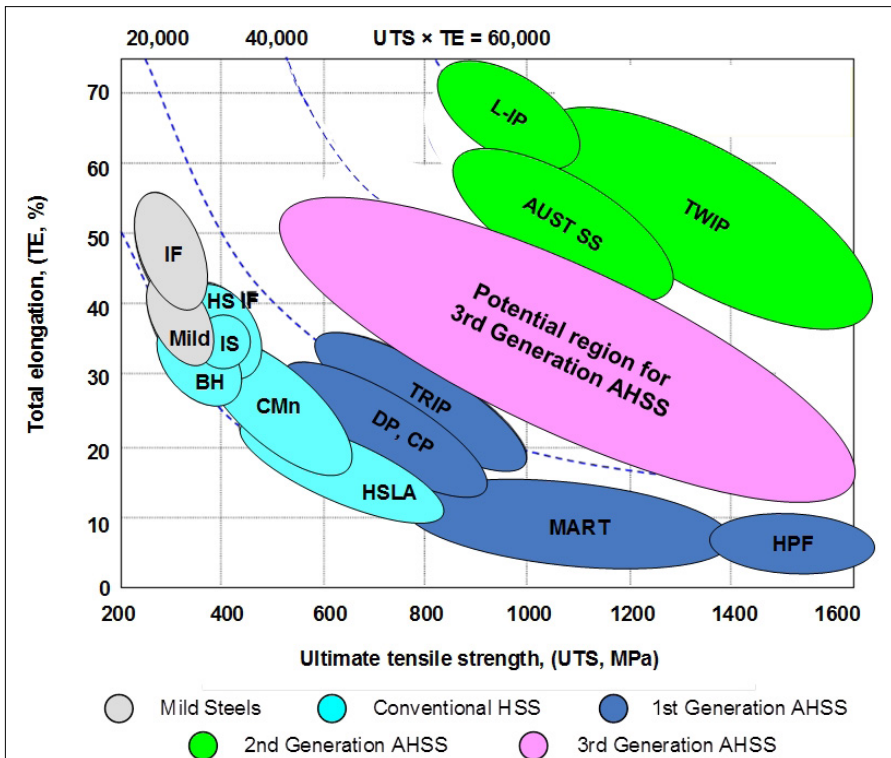


**Figure 1.** Ultimate Tensile Test vs Total Elongation including the classification of Advanced High Strength Steels. [2]

**Figure 1.** shows the mild steels (IF, Mild) that have played a key role in the automotive industry for several decades, the traditional high-strength steels (HS-High Strength Interstitial Free, BH-Bake Hardening, CMn-Carbon Manganese), which also have significant automotive applications, and finally HSLA, i.e. High Strength Low Alloyed steels, which is the main representative of this group).

The next group is the 1<sup>st</sup> generation of advanced high-strength steels (1G-AHSS). This group includes dual-phase DP steels, phase transformation induced plasticity TRIP steels, complex phase CP steels, and martensitic, MS steels. These steels are in the range of  $C = 10,000\text{--}25,000$  (MPa %) with respect to the previously introduced  $R_m \times A_{80} = \text{Constant}$  curves.

The 2<sup>nd</sup> generation of advanced high-strength steels is represented by steel developments in the range  $R_m \times A_{80} = 40,000\text{--}65,000$  (MPa %) (2G-AHSS). The most characteristic members of this group are the Twinning Induced Plasticity (TWIP) steels with twin-induced plasticity behaviour, but this group also includes corrosion-resistant austenitic steels with high-Mn content (e.g. AUST SS) and L-IP steels called Lightweight Induced Plasticity. These steels provide an excellent combination of strength and formability, however, despite their excellent properties, this group has not achieved a real breakthrough in automotive applications, mainly due to low productivity and high production costs.

The next stage of development of advanced high-strength steels (AHSS) led to the development of so-called 3<sup>rd</sup> generation high-strength steels (3G-AHSS), which is still in the development and first industrial implementations stage, however, steelmakers have already achieved a number of remarkable achievements in this field, too.

The basic idea behind these developments is to provide properties in the range between the 1<sup>st</sup> and 2<sup>nd</sup> generation high-strength steels, which can be interpreted on the basis of **Figure 1.**

In the development of this group, it is of paramount importance that excellent mechanical properties are achieved with less alloying elements and thus at a lower cost, especially compared to 2<sup>nd</sup> generation steels.

The microstructure of these steels typically consists of multiple phases (e.g., nano / ultra-fine-grained ferrite, martensite, or bainite) and, when combined with an additional phase (e.g., austenite), provides increased formability and higher strain hardening. With this development concept,

high-strength steels in the GPa range can be produced with remarkable formability at the same time [3].

In the following, we analyse the recent major steel development efforts and achievements through the presentation of some representatives of these three generations.

### 3. Main types of Advanced High Strength Steels

The most important feature of the different generations of advanced high-strength (AHSS) steels is that they have a complex, carefully selected chemical composition and a multiphase microstructure that can be produced as a result of precisely controlled heating and cooling processes. Various strength-enhancing mechanisms are used to achieve significantly increased strength, better formability, increased toughness and fatigue properties to meet, as far as possible, the complex requirements for car components.

#### 3.1. First Generation Advanced High Strength Steels

The most characteristic and already widely used types of this group are the DP and TRIP steels, but in this group it is definitely worth mentioning the martensitic steels recently with growing application developed specifically for hot sheet forming in the automotive industry. These steels are referred to as Press Hardening Steels (PHS) in the international literature. In order to utilize their excellent properties, special new technological processes have been developed particularly for the processing of this type of steel.

##### 3.1.1. Dual Phase (DP) steels

Dual-Phase (DP) steels play an important role in both first-generation high-strength steel developments and in automotive applications. DP steels evolved from early research on dual phase steels in the late 1970s and early 1980s. Their widespread application is mainly due to the fact that their favourable strength and formability parameters result in a significantly more favourable property combination compared to conventional high-strength steels, such as HSLA.

DP steels have high specific strength, good initial deformation hardening together with excellent formability. These properties make it particularly suitable for the production of vehicle body parts, various enclosures and fuel tanks by forming [4].

**Figure 2.** shows temperature-time diagrams of different production possibilities of DP steels (processes A, B and C). In each procedure, the

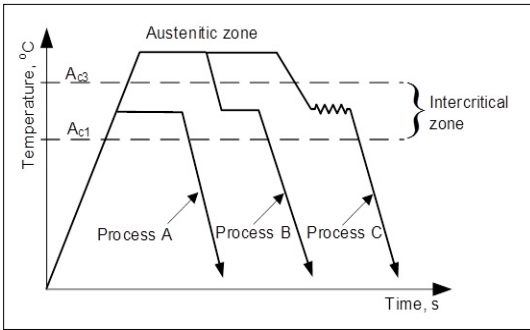


Figure 2. Processing routes of DP-steels.

so-called intercritical temperature is of paramount importance.

Dual Phase (DP) steels contain mainly martensite islands (in some cases bainite) embedded in a ferrite matrix as the second phase. It is characteristic that the continuous ferrite particles provide excellent formability. During forming, the deformation is concentrated on the low-strength ferrite phase surrounding the martensite islands; in addition to the excellent formability, this microstructural feature is also the basis for the significant deformation hardening experienced in DP steels [5].

### 3.1.2. TRIP steels

These steels utilize the phenomenon of transformation-induced plasticity. (The abbreviation TRIP is formed from the initials of the English words Transformation Induced Plasticity). These steels are also excellent for the production of body elements / structures that focus on weight reduction, and at the same time provide additional benefits in terms of increased safety.

One of the main characteristics of TRIP steels is that the transformation of residual austenite present in the microstructure, during processing due to deformation, results in a significant increase in strength, while also having a relatively significant formability depending on the manufacturing process [6].

The microstructure of TRIP steels contains martensite, bainite and residual austenite embedded in a ferrite matrix. Their excellent formability and high strength can be explained by the transformation of residual austenite to martensite due to deformation. This transformation of the phases due to deformation is called the TRIP effect, and results in an excellent combination of strength and deformation, as well as good resistance to dynamic effects.

The typical manufacturing process for TRIP steels is as follows: the steel is heated up to the austenitic zone and kept for the time required to achieve a homogeneous austenitic state. This is followed by cooling to the intercritical temperature and then hot forming the sheet at that temperature. The next step is rapid cooling to the bainite zone and keeping in the bainite range to get bainite in the required amount.

TRIP steels are characterized by a relatively low alloy content. For example, in TRIP 790 steel ( $R_m \approx 790$  MPa), the total amount of alloying elements is about 3.5 weight percent. The selection of the appropriate alloying elements and the amount required to achieve the desired properties are critical to the intended mechanical properties of the alloy. TRIP steels generally have a higher carbon content than DP steels [7].

### 3.1.3. Press Hardening Steels – PHS

Among advanced high-strength steels, the application of Press Hardening Steels and Hot Press Forming (HPF) technology is a very special, unique group of advanced high-strength steels. These are mostly manganese steels with different boron content and a wide range of high-strength structural elements (e.g. A-pillars and B-pillars for passenger cars) can be produced from them. Several types are known, of which 22MnB5 is considered the basic type of PHS steels.

A typical temperature-time diagram of the hot press forming + hardening in the tool process is shown in Figure 3.

With the appropriate combination of heating, holding, forming and rapid cooling, complex components with excellent strength properties can be produced by the process shown in Figure 3. [8]. There are various technological variants of the process, including so-called direct and indirect hot forming.

In addition to these two basic processes, there are other process variants: the final microstructure and the mechanical properties of the component can be controlled very effectively depending on the holding temperature and the cooling process. Depending on the holding temperature, two further process variants can be derived: complete austenitisation can be considered as the basic variant, i.e. when the holding temperature is chosen in the homogeneous  $\gamma$ -zone. Depending on the holding temperature, a further process variant can be used if the holding temperature is chosen in the intercritical range (i.e. between  $A_1$  and  $A_3$  temperatures), which means that there

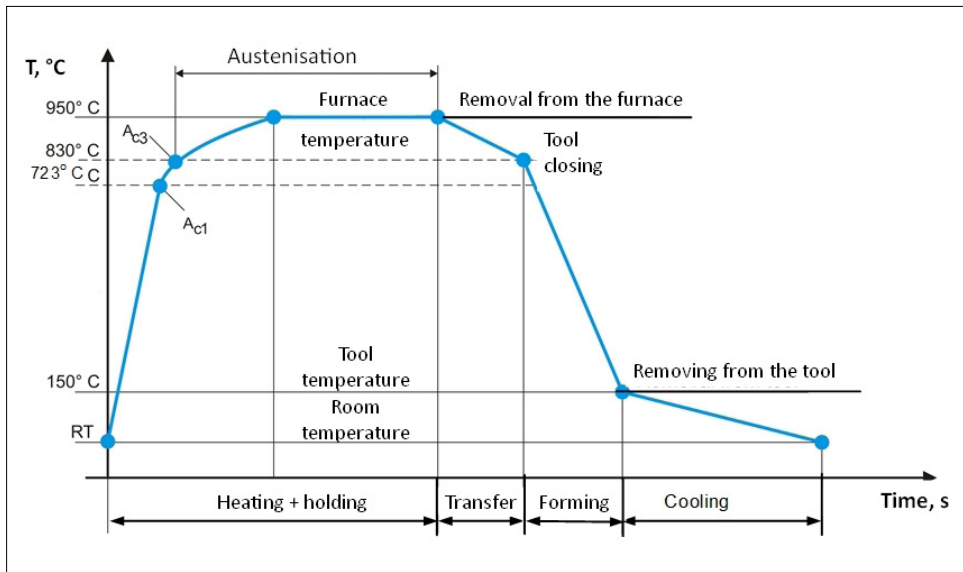


**Figure 3.** Time-temperature diagram of Hot Press Forming.

is no complete austenitisation. The initial microstructure at this holding temperature contains ferrite and austenite, in quantities depending on the position of the actual holding temperature between the critical temperatures  $A_1$  and  $A_3$ . In this case only the austenite content can be converted to martensite and the final microstructure will contain a certain amount of ferrite after forming and rapid cooling. Obviously, this variant results in lower strength compared to total austenitisation, while also providing better formability and better toughness characteristics.

Additional process variants can also be derived by varying the cooling rate after forming. If the cooling rate is lower than the upper critical one, the final microstructure contains bainite in addition to martensite. This results in lower strength depending on the amount of bainite, but together with increased toughness; bainite may be advantageous due to its better energy absorption properties in parts where impact resistance and fracture safety play a key role, increasing the fracture toughness of the part.

It is important that the forming should be completed above the  $M_s$  line (i.e. above the initial temperature of martensitic transformation): these material qualities still have sufficient formability at this stage. After forming, the part is cooled together with the tool: this cooling must provide the critical cooling rate in order to obtain the required amount of martensitic microstructure. With this process, post-forming springback can

be reduced significantly and parts with excellent strength properties can be transformed into complex geometries.

Typical hot-pressed steels (PHS) also have a tensile strength of  $R_m = 1500\text{--}2000$  MPa. In recent decades, these process variants have been widely used in various safety and impact-resistant body parts. The new generation PHS steels even reach strengths above 2000 MPa. These PHS steels and the process variants analysed above are mainly used in the production of elements where, in addition to increased fracture safety, small deformations are typically allowed (e.g. A- and B-column reinforcements, various sill elements, floor panels, etc.).

### 3.2. Second Generation Advanced High Strength Steels

The 2<sup>nd</sup> generation of advanced high-strength steels (2G-AHSS) are represented by steel developments in the range  $R_m \times A_{80} = 40,000\text{--}65,000$  (MPa·%). The most characteristic representatives of this group are the TWIP steels with twin-induced plasticity, but also some corrosion-resistant austenitic steels (AUST SS) with high Mn-content and L-IP steels called Lightweight Induced Plasticity steels belong to this group. These steels provide an excellent combination of strength and formability, however, despite their excellent properties, this group has not yet achieved a real breakthrough in automotive applications, mainly due to low production productivity and high production costs.

### 3.2.1. TWIP steels

TWIP steels are based on the special mechanism by which an outstanding balance between strength and formability characteristics can be achieved by utilizing the deformation twin mechanism. The name of the steel group is also derived from this characteristic mode of deformation, i.e. the acronym abbreviation for the English name for twin-induced plasticity (TWIP). Twin formation results in a significant increase in the hardening exponent, the  $n$ -value, due to the increasingly fine microstructure associated with the twin formation mechanism.

TWIP steels typically have a high manganese content ( $Mn=17\text{--}24\%$ ), as a result of which the steel is completely austenitic even at room temperature. These steels have an outstanding strength-formability combination (for example, even with a tensile strength above  $R_m > 1000$  MPa, a total elongation of up to 50% can be achieved), i.e. TWIP steels also show extremely high formability in addition to very high strength [9].

Another feature of TWIP steels is the high hardening exponent, which can reach  $n \geq 0.4$ . For TWIP steels, the stability of the strain hardening is closely related to the Stacking Fault Energy (SFE). This parameter basically determines the deformation behaviour of TWIP steels.

The characteristics outlined above result in a very exceptional combination of strength and formability, which places the constant value of  $R_m \times A_{80} = \text{Constant}$  in the range  $C = 40,000\text{--}65,000$  MPa% outlined in [Figure 1](#). Despite these outstanding mechanical properties, TWIP steels have not achieved breakthrough application success in the automotive industry, mainly due to low productivity and high costs.

### 3.2.2. Austenitic corrosion-resistant steels

The excellent properties of austenitic stainless steels are well known and are used in many fields. Their use in the automotive industry came to the forefront of research during the development of 2<sup>nd</sup> generation high-strength steels.

Austenitic stainless steels typically have a high chromium and nickel content. Their most typical representatives are the classic 18/8 stainless steel with 18% Cr and 8% Ni, which, in addition to its excellent corrosion resistance, also has excellent mechanical properties. In this respect, their significant cold strain hardening capacity is particularly remarkable. These steels are characterized by low yield strength, high ductility, high tensile

strength and excellent toughness properties.

The excellent formability characteristics of such steels are due to the 12 sliding system resulting from the face centred cubic crystal system. In addition, the minimum amount of interstitial elements should be mentioned, as this also contributes to the operation of the barrier-free dislocation sliding mechanism and thus to the excellent plasticity characteristics.

AUST SS steels are typically produced by continuous strip casting and hot sheet rolling. The sheets thus produced are cold-rolled to the desired thickness and the resulting hardening is achieved in a hydrogen / nitrogen protective atmosphere. During the recrystallization, a sufficiently fine particle structure and the dissolution of any carbide precipitates are ensured by an appropriate thermal program. After annealing, cooling should be performed at a sufficient rate to avoid precipitation of carbides.

### 3.2.3. Lightweight Induced Plasticity – L – IP steels

Special types of weight reduction induced plasticity steel developments are Lightweight Induced Plasticity steels, which are referred to as L-IP steels. This designation is mainly used for the Fe-Mn-Al-C alloy type, for which the Al content is a special feature: Al is the key alloying element in providing mass reduction [10].

In terms of alloying elements, Mn and C are austenite forming and Al are ferrite-stabilizing and increase the metastable dissolution of C by reducing the diffusion capacity. L-IP steels with a suitable chemical composition result in a triplex microstructure containing austenite, ferrite and  $\kappa$ -carbides – (Fe, Mn)<sub>3</sub>AlC.

## 3.3. Third generation advanced high strength steels

The main goal of the development of 3<sup>rd</sup> generation high strength steels (3G-AHSS) is to achieve mechanical property combinations in the range of 1<sup>st</sup> and 2<sup>nd</sup> generation AHSS steels with less alloying quantities and consequently more economical, lower cost production with a wide range of applications achieved in a short time. We present some recent development results from this group.

### 3.3.1. Quenching & Partitioning – Q&P steels

Steels produced by rapid cooling (quenching) and partitioning are the result of the latest developments in third generation AHSS steels: they are

referred as Q&P steels, i.e. Quenched and Partitioned steels. Q&P steels typically contain alloys of carbon, manganese, silicon, nickel and molybdenum. Depending on the strength requirements, they contain around 4% alloying elements, which is much less than for second-generation AHSS steels, making it a less expensive manufacturing process [11].

During the heat treatment of Q&P steel, rapid cooling, i.e. quenching is interrupted and the steel is reheated for partitioning. This results in 5–12% stable residual austenite, 20–40% ferrite and 50–80% martensite. The Q&P process can produce steels with a tensile strength above 2100 MPa with a uniform elongation of 9% and a total elongation of about 13%. The deformation behaviour of this steel is comparable to that of DP 980 steel, which can be considered cold-formable.

Q&P steels are a series of C-Si-Mn, C-Si-Mn-Al, or other similar compositions produced by the quenching and partitioning (Q&P) heat treatment process. The microstructure of Q&P steels is ferrite (in the case of partial austenitisation), martensite and residual austenite, which results in excellent strength and deformation characteristics. These properties allow them to be used as automotive parts. Q&P steels are suitable for the cold-forming production of relatively complex automotive components, while increasing fuel economy and passenger safety.

Two basic versions of the Quenching & Partitioning procedure have been developed. The basic version includes a quenching followed by partitioning. The newer version uses the so-called Double-Stabilization Thermal Cycle (DSTC) [12].

The Double Stabilization Thermal Cycle (DSTC), aims to provide a high volume of residual austenite and martensite with sufficient carbon content to provide high strength. Similar to the basic variant analysed above, the aim is also to prevent carbide formation in order to allow as much carbon diffusion from martensite into austenite as possible during the partitioning process. The temperature-time cycle of this process is shown in Figure 4.

The production steps for Q&P steels produced with a double stabilization thermal cycle (DSTC) can be summarized as follows:

1. *Austenitisation.* The first step in the Double Stabilization Thermal Cycle is a full austenitisation process.
2. *Initial rapid cooling.* Austenitisation is followed by a sufficiently rapid, first cooling to prevent possible bainite transformation. This

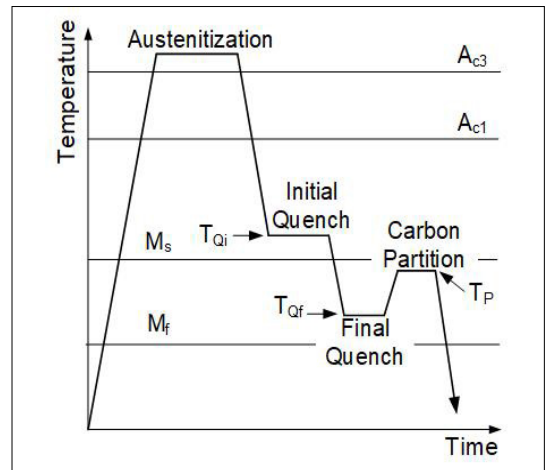


Figure 4. Q&P with Double Stabilization Thermal Cycle).

cooling is continued down to slightly above the initial temperature ( $M_s$ ) of the martensitic transformation. At this temperature, austenite is primarily stabilized.

3. *Finishing fast cooling.* The initial rapid cooling is then followed by rapid cooling to a temperature above  $M_f$ , where the austenite / martensite ratio is adjusted by the appropriate holding time.
4. *Carbon partitioning.* Partitioning is carried out below the temperature  $M_s$ : the purpose of this is a secondary stabilization in which carbon diffuses from the martensite into the austenite, increasing the carbon content of the austenite and thus increasing its stability. As a result, the resistance of austenite to martensite is further increased.
5. *Air cooling.* The steel containing about 30% austenite, 23% ferrite and 47% martensite is then cooled down to room temperature in air. Additional Si and Al alloys are added to prevent carbide formation.

### 3.3.2. Bainite-ferrite steels utilizing the TRIP effect

Third-generation high-strength steels represent a further remarkable development of low-alloy bainite-ferrite (TBF) steels utilizing the TRIP effect. Various literature refers to TBF steels utilizing the TRIP effect, some literature refers it as  $\delta$ -TRIP steels, referring to lower density based on aluminium content.

The microstructure of TBF steels consists of a bainite-ferrite matrix with residual austenite

particles. The typical chemical composition of TBF steels contains as main alloying elements C, Si and Mn. Other common alloys are Al, Nb and Cr in various composition combinations [13]. Si inhibits carbide formation during bainite phase transition, which increases the C content of residual austenite and thus allows stabilization of residual austenite with carbon.

One of the major advantages of these steels over Q&P steels is that they can be produced in conventional heat treatment facilities, while the production of Q&P steels has required significant conversion of heat treatment facilities. They are produced from the fully austenitic microstructure by isothermal heat transfer in the bainite range after rapid cooling.

### 3.3.2. Nano Steels

Another group of third-generation, high-strength steels, is the so-called Nano-steel®, which is still mostly in the development stage, and is not commercially available yet. This type is characterized by a nano-crystalline structure created by a special chemical composition and heat treatment. After casting, the steel has a predominantly austenitic microstructure with some boride. After heat treatment, the austenite is refined to a nanometer scale. During plastic deformation, stress-induced nano-scale phase formation increases the ability of the deformation to harden, i.e. the strain hardening ability [14].

## 4. Conclusions

The automotive industry is facing increasing demands in recent decades. Growing demands can be observed in terms of both users and legal requirements. On the consumer side, there is a need for passenger cars that are increasingly economical, lower in consumption, but at the same time offer a higher level of comfort and safety. This is complemented on the legal side by increased environmental standards aimed at achieving the lowest possible emissions. In meeting these requirements, weight reduction plays a key role in the automotive industry. Weight reduction needs increasingly necessitate the use of high strength sheet materials.

The development of high-strength steels is of paramount importance for mass reduction needs. In recent decades, three generations of the development of high-strength steels - first, second and third generation, have been observed in the development of advanced high-strength steels.

In this paper, we have reviewed three generations of steel developments, presenting the key representatives of each generation, analysing the key characteristics of each high-strength steel, their manufacturing processes and their applications in the automotive industry.

Some of these developments (eg DP and TRIP steels) have already been widely used in the automotive industry, while some types (mainly the second generation developments such as TWIP steels) have not yet been used due to lower production productivity and higher production costs.

The latest, promising phase of the developments is the elaboration of third-generation high-strength steels, which aims to bridge the gap between first- and second-generation developments. In the development of this group, it is of paramount importance that the designed excellent mechanical properties are achieved with fewer alloys and thus at a lower cost, especially compared to 2<sup>nd</sup> generation steels.

### Acknowledgement

The research work described in this paper is partly elaborated in the project “AutoTech - Development of metal forming, welding and heat treatment in the Hungarian automotive industry” (Ref. no. : TÁMOP-4.2.2 / A-11/1-KONV-2012-0029).

In this paper, the results of the projects Horizon 2020 “Low Cost Materials Processing Technologies for Mass Production of Lightweight Vehicles – LoCoMa-Tech” (EU Grant No: H2020-NMBP-723517-GV-2016) is also summarized.

Research participants would like to express their gratitude to both the Hungarian Government and the European Commission for their financial support.

### References

- [1] Tisza M.: *Képlékenyalakítás az autóiparban*. Miskolci Egyetemi Kiadó, 2015. 294.
- [2] Tisza M.: *Development of Lightweight Steels for Automotive Applications*. In: Ashutosh Sharma (ed.): *Engineering Steels and High Entropy-Alloys*. IntechOpen, 2020 <https://doi.org/10.5772/intechopen.91024>
- [3] Nanda T., Singh V., Singh V., Chakraborty A., Sharma S.: *Third generation of advanced high-strength steels: Processing routes and properties*. Journal of Materials: Design and Applications, 233/2. (2019) 209–238. <https://doi.org/10.1177/1464420716664198>
- [4] Li C., Li Z., Cen Y., Ma B., Huo G.: *Microstructure and mechanical properties of dual phase strip steel in the over-aging process of continuous annealing*. Materials Science and Engineering: A, 627 (2015) 281–289. <https://doi.org/10.1016/j.msea.2014.12.109>

- [5] Meng Q., Li J., Wang J., Zhang Z., Zhang L.: *Effect of water quenching process on microstructure and tensile properties of alloy cold rolled dual-phase steel*. Materials & Design, 30/7. (2009) 2379–2385. <https://doi.org/10.1016/j.matdes.2008.10.026>
- [6] Rana R., Liu C., Ray R. K.: *Evolution of microstructure and mechanical properties during thermo-mechanical processing of a low-density multiphase steel for automotive application*. Acta Materialia, 75 (2014) 227–245. <https://doi.org/10.1016/j.actamat.2014.04.031>
- [7] Kuziak R., Kawalla R., Waengler S.: *Advanced high strength steels for automotive industry*: Archives of Civil and Mechanical Engineering, 8/2. (2008) 103–117. [https://doi.org/10.1016/S1644-9665\(12\)60197-6](https://doi.org/10.1016/S1644-9665(12)60197-6)
- [8] Tisza M.: *Hot forming of boron alloyed Manganese steels*. Materials Science Forum, 885 (2015) 25–30. <https://doi.org/10.4028/www.scientific.net/MSF.885.25>
- [9] Chung K., Ahn K., Yoo D. H., Chung K. H., Seo M. H., Park S. H.: *Formability of TWIP (twinning induced plasticity) automotive sheets*. International Journal of Plasticity, 27/1. (2011) 52–81. <https://doi.org/10.1016/j.ijplas.2010.03.006>
- [10] Scott C., Remy B., Collet J. L. et al: *Precipitation strengthening in high manganese austenitic TWIP steels*. International Journal of Materials Research, 102/5. (2011) 538–549. <https://doi.org/10.3139/146.110508>
- [11] Wang, J., Yang, Q. et al.: *A phenomenon of strain induced bainitic transformation and its effect on strength enhancement in a lightweight transformation-induced-plasticity steel*. Materials Science & Engineering A, 751. (2019) 340–350. [doi.org/10.1016/j.msea.2019.02.057](https://doi.org/10.1016/j.msea.2019.02.057)
- [12] Speer J. G., Edmonds D. V., Rizzo F. C., Matlock D. K.: *Partitioning of carbon from supersaturated plates of ferrite, with application to steel processing and fundamentals of the bainite transformation*. Current Opinion in Solid State and Materials Science, 8/3–4. (2004) 219–237. <https://doi.org/10.1016/j.cossms.2004.09.003>
- [13] Bachmaier A., Hausmann K., Krizan D., Pichler A.: *Development of TBF steels with 980 MPa tensile strength for automotive applications*. In: Proceedings of Int. Conf. on New Developments in Advanced High Strength Steels. Colorado, June 2013.
- [14] Singh H.: *Nanosteel Intensive Body-in-White*. Research Study. EDAG Inc. August 2013.

# Some Formability Aspects of High Strength Steel and of Consisting Tailor Welded Blanks

Gábor J. BÉRES,<sup>1</sup> Ferenc VÉGVÁRI,<sup>2</sup> József DANYI<sup>3</sup>

John von Neumann University, GAMF Faculty of Engineering and Computer Science, Department of Innovative Vehicles and Materials, Kecskemét, Hungary

<sup>1</sup> [beres.gabor@gamf.uni-neumann.hu](mailto:beres.gabor@gamf.uni-neumann.hu)

<sup>2</sup> [vegvari.ferenc@gamf.uni-neumann.hu](mailto:vegvari.ferenc@gamf.uni-neumann.hu)

<sup>3</sup> [danyi.jozsef@gamf.uni-neumann.hu](mailto:danyi.jozsef@gamf.uni-neumann.hu)

## Abstract

In recent years, the demand for a reduction in pollutant emission has become extremely important in the vehicle industry. It can be achieved through fuel consumption reduction, which is a direct function of the vehicle's weight. Nowadays weight is widely controlled by the use of advanced- and ultra-high strength steels (AHSS and UHSS) in vehicle body construction. With the application of such steel sheets as chassis elements, crashworthiness can be maintained next to reduced sheet thicknesses, too. In this paper, the deep-drawability and springback after V-die bending is monitored for three types of AHSS grades, namely DP600, DP800 and DP1000 materials. The investigations are extended to tailor welded blanks (TWBs), made by the aforementioned steels coupled with a cold rolled steel sheet (DC04). Our results show that deep-drawability reduces with both the increase in strength and the increase in strength difference between the components in the TWBs. Furthermore, the higher strength is shown to cause higher spring-back. The TWBs have unique spring-back behavior around the weld line.

**Keywords:** high strength steels, tailor welded blanks, deep-drawability, springback.

## 1. Introduction

Advanced high strength steels are widely used as body-in-white elements in the automotive industry, however, parts made by welded blanks are no longer uncommon. This reflects the aim of achieving idealized material distribution within the chassis. Since the elements' destination is a function of the location, the principle of the best material to the best place can be fulfilled also within a piece part if tailor welded blanks are used. At the same time, the different properties in such a complex blank can lead to different problems during the manufacturing processes, such as dimensional accuracy and unique failure modes [1].

Manufacturing using high strength steels can basically raises formability problems. Figure 1. shows that an increase in strength is accompanied by a reduction in formability [2].

In our work we focus on the deep-drawability and spring-back of three types of AHSS grades in the frames of a research project jointly with the Department of Mechanical Technologies at the University of Miskolc. This paper gives a brief insight

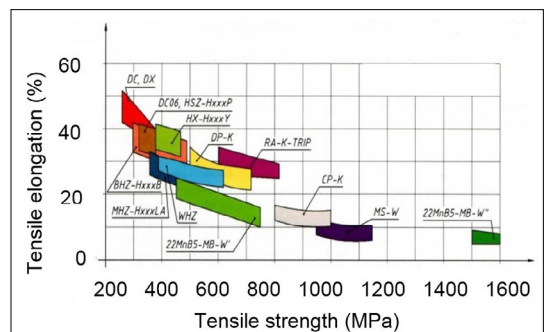


Figure 1. The relation of the strength and formability (through elongation) of today's automotive steel sheets.

into the experimental formability behaviour of dual phase steel sheets, furthermore the question of TWBs is also discussed if such materials are coupled with a cold rolled quality, namely with the DC04 sheet.

## 2. Investigated materials

The applied materials were three types of commercial, non-covered dual phase steels, Docol DP600, DP800 and DP1000 as well as a cold rolled steel grade, DC04. The last one is specially recommended for deep-drawing [3]. The DP abbreviation refers to the dual phase microstructure of the material, in which the soft ferrite and the hard martensitic phases together provide the high strength and the relative good formability [4]. The basic mechanical properties (yield strength, ultimate tensile strength, uniform- and total elongation) are listed in Table 1. The tensile experiments were carried out in accordance with the MSZ EN ISO 6892 standard requirement at room temperature, on three parallel specimens. The sheets had 1 mm thickness ( $t$ ) uniformly.

**Table 1.** The basic mechanical properties of the applied materials.

|        | $R_{p0.2}$<br>(MPa) | $R_m$<br>(MPa) | $A_g$<br>(%) | $A_{80}$<br>(%) |
|--------|---------------------|----------------|--------------|-----------------|
| DC04   | 238                 | 336            | 22.6         | 37.9            |
| DP600  | 444                 | 656            | 13.6         | 20.6            |
| DP800  | 570                 | 789            | 10.8         | 16.0            |
| DP1000 | 758                 | 1099           | 7.0          | 10.6            |

## 3. Investigation of springback after free bending

It is well known that the bending angle changes following the bending tools release in a bending process, i.e. in the unloading stage. On one hand, this is caused by the elastic region near to the natural axis, which takes an elastic moment in the opposite direction to the bending. On the other hand, the total strain is the sum of the elastic and plastic strains, thus the elastic proportion tries to return the workpiece into the initial geometry [5]. As a result, the extent of the springback ( $\beta$ ) is primarily influenced by the strength, the elastic modulus and the thickness of the material, as well as the bending geometry, such as punch corner ( $r$ ) radius and bending angle [6, 7, 8, 9]. For the most comprehensive investigations of these factors, different grades of DP steels were applied with different punch corner radiuses, in this study. The

bending investigations were performed on three parallel workpieces with constant 20 mm/min stroke by an AMADA HFE 50-20 CNC machine (Figure 2.).

The side view sketch of the bending tools (punch and V-die) can be seen in Figure 3. Using 3 mm and 5 mm punch corner radiuses, different  $r/t$  (punch corner radius/sheet thickness) ratios could be obtained during the experiments. All the samples were bent to 90°, which was controlled by the punch motion.

Figure 4. shows the measurement results of the base materials' mean springback angles, at 3 and at 5  $r/t$  ratios. The indicated data points were determined on the edges of the sheets by a workshop angle meter with 15' precision. Generally, no higher than  $\pm 0,5^\circ$  average deviation was recorded for all materials and geometries.



**Figure 2.** The applied Amada bending machine.

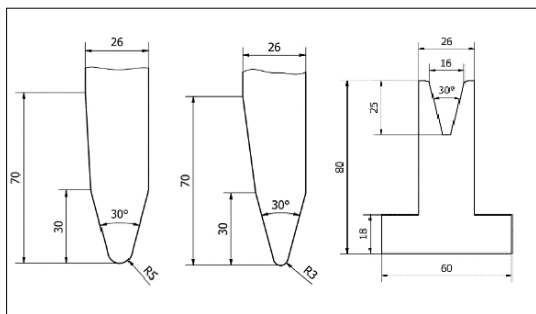


**Figure 3.** The applied punch and die geometry.

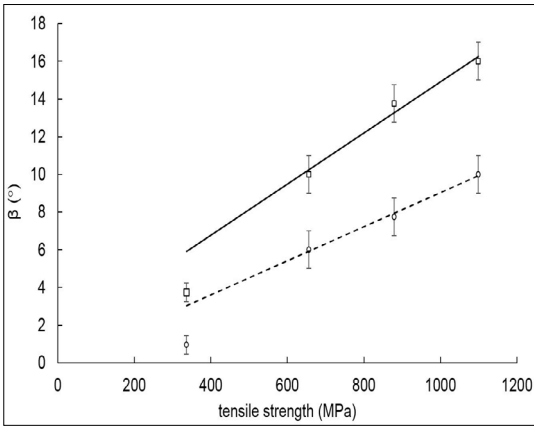


Figure 4. The experimental spring-back angles of the base materials.

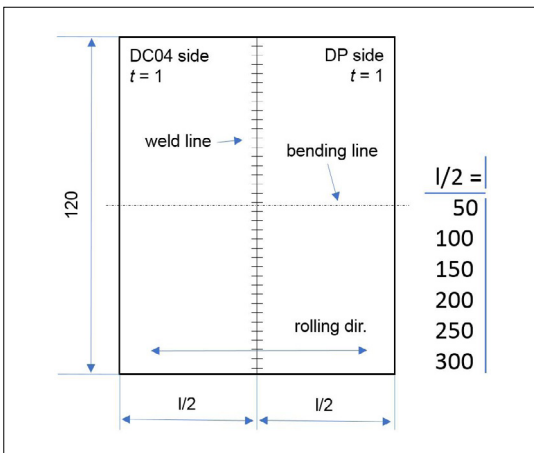


Figure 5. Schematic drawing of the TWB samples. Units in (mm).

The base materials had 120mm width and 600mm length, in which the length direction coincided with the rolling direction. The bending line was always perpendicular to the rolling direction. From the results it can be seen that both the strength and the  $r/t$  ratio increase the spring-back angle ( $\beta$ ).

In case of the tailor welded blanks, all samples contained a DP steel grade coupled with the DC04 steel. This means that the DP side was changed from part to part, but the DC04 was constantly used. The blanks were created by laser beam welding at the Zoltán Bay Applied Research Non-profit Ltd. The detailed characterization of the weld can be found in [10]. The aim of the experiments was to monitor the interaction between the different sides of the welded blank. The spring-back measurements were carried out on samples

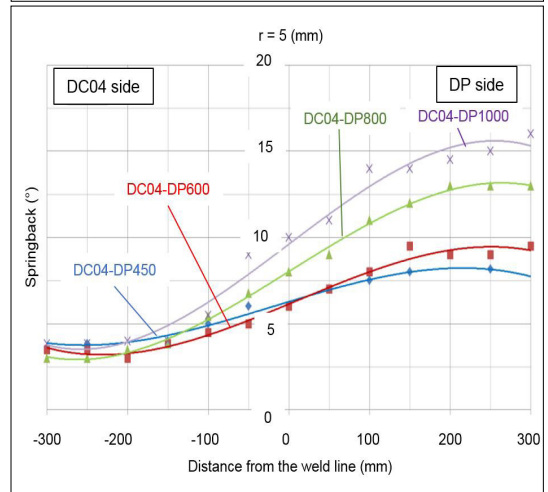
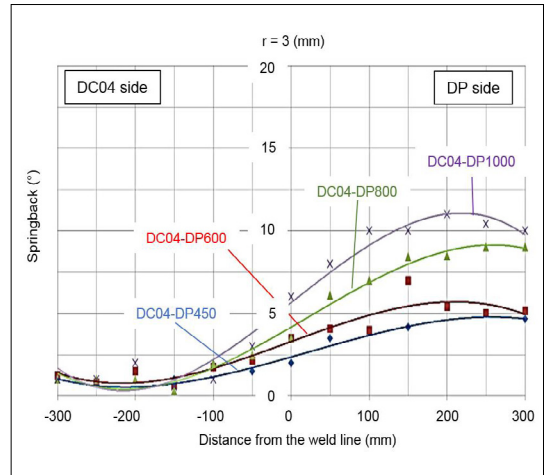


Figure 6. Experimental spring-back angles of TWBs.

with different lengths to make the welded zone's effect visible, in the function of the distance from the weld line. The schematic view of the welded sample design can be seen in Figure 5.

Figure 6. shows the average experimental springback tendency of the tailor welded blanks. The final angles after elastic unloading were measured at the edges of the workpieces, i.e. at different distances from the weld line. The measurement method was equal to that applied at the base materials. According to the diagrams, none of the components show their characteristic springback value near to the weld line, rather a transition zone is developed.

It is noteworthy that the distinct spring-back angles within a work-piece actually create a shape error.



Figure 7. The applied universal sheet metal tester equipment.

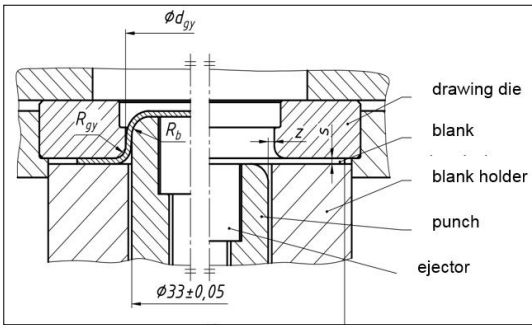


Figure 8. Schematic illustration of the deep-drawing tools.

#### 4. Experimental results of deep-drawability

The deep-drawing tests of both the base and the welded materials were carried out by an Erichsen 142-20 universal sheet metal tester (Figure 7). The tooling was matched with the Swift cup drawing test's [11] tools, in accordance with the MSZ 5731-68 standard. The arrangement of the blank and the tools are depicted schematically in Figure 8.

In this testing method, the diameter of the blank ( $D$ ) is increased in 2 mm increments until crack occurrence. The circular blanks with 56, 58, 60, ... 80 mm diameter were manufactured by blanking and then turning with at least  $\pm 0.1$  mm precision. Three parallel measurements were performed in this case as well, with  $0.012 \text{ g/cm}^2$  oil lubricant on the die side (as suggested by [12]) and with the optimal blank holder forces according to Siebel [13]. A sequence of DC04 deep-drawn cups can be seen in Figure 9.



Figure 9. The sequence of drawn cups, DC04 material.

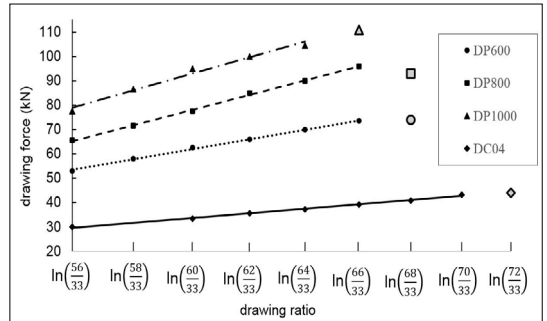
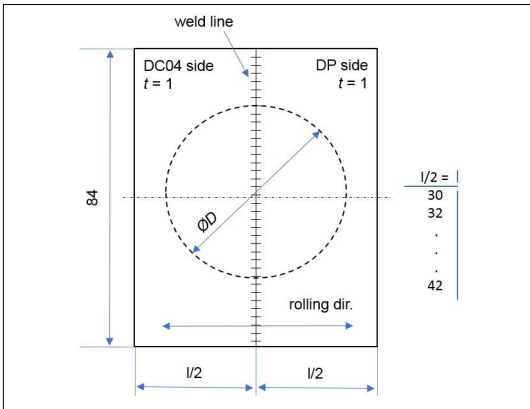


Figure 10. The limited drawing ratios and the corresponding drawing forces of the different base materials.

The average values of the biggest diameters, that could be drawn without failure (dashed mark) and the corresponding drawing forces are shown in Figure 10. It can be concluded that the increase in strength causes a decrease in the limited drawing ratio as well as an increase in the drawing force.

It is not necessary to explain in detail that the deep-drawing operation is accompanied by the most complicated stress and strain state in sheet metal forming. It is especially true for the welded blanks due to the inhomogeneous deformation of each segment and the different optimal blank holder forces of each side. However, the lower strength component has higher resistance to thinning (see Figure 10), its load carrying capacity is questionable if the drawing force is dictated by the higher strength part.

Workpiece manufacturing from the welded blanks is shown schematically in Figure 11. The mean measurement results are added in Figure 12. As a conclusion of the previous line of thought, it can be seen that the deep-drawability is neither influenced directly by the lower, nor the higher strength component, but is instead determined by the strength difference between each part.



**Figure 11.** Schematic drawing of the welded specimens for the deep-drawing experiments.

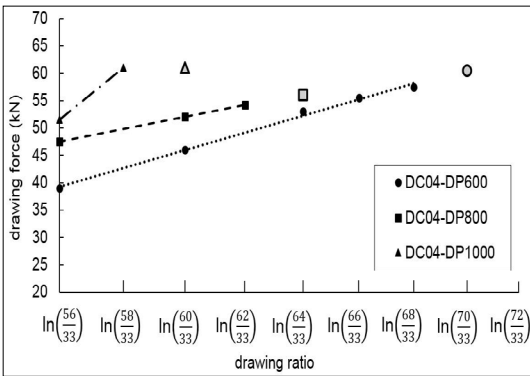


**Figure 12.** Experimental drawability results of the TWBs.



**Figure 13.** Picture of cups made by TWBs.

In contrast to the base materials, the drawability limit of the TWBs is restricted by the crack occurrence next to the weld line at the lower strength side, instead the cracking at the punch corner radius. It can be monitored in the pictures of the cups made by DC04-DP1000 TWBs (Figure 13.) that the lower strength side had stronger defor-

mation thus earlier thinning occurred as well, due to the coercive effect of the higher strength component.

## Conclusion

In this study we focused on the springback and deep-drawability behavior of three types of advanced high strength steels (DP600, DP800 and DP1000) and tailor welded blanks consisting the same materials extended by a cold-rolled, mild steel, DC04. Our results show that springback is increased with the strength of the applied material on its own. However, using tailor welded blanks, springback is developed especially in a transition zone, in which the final angle differs from both components' characteristic values. In the field of deep-drawability it is shown that the higher the strength the lower the limited drawing ratio for the base materials. In the case of the tailor welded blanks, it is not the strength of the components but the strength difference between them that determines the maximum drawing ratio, i.e. the formability.

## References

- [1] Merklein M., Johannes M., Lechner M., Kuppert A.: *A review on tailored blanks-Production, applications and evaluation.* Journal of Materials Processing Technology, 214. (2014) 151–164. <https://doi.org/10.1016/j.jmatprotec.2013.08.015>
- [2] Keeler S., Kimchi M.: *Advanced High-Strength Steels Application Guidelines Version 6.0. 3S-Superior Stamping Solutions.* LLC., WorldAutoSteel, 2017. 1–17.
- [3] Kuziak R., Kawalla R., Waengler S.: *Advanced high strength steels for automotive industry.* Archives of Civil and Mechanical Engineering, 8/2. (2008) 103–117. [https://doi.org/10.1016/S1644-9665\(12\)60197-6](https://doi.org/10.1016/S1644-9665(12)60197-6)
- [4] Thyssenkrupp: *Deep-drawing steels DD, DC and DX.* Production information, 2018. 2–9.
- [5] Danyi J., Végvári F.: *Lemezmegmunkálás.* Kecskeméti Főiskola, 1<sup>st</sup> ed., Kecskemét, 2011. 97–104.
- [6] Marciniak Z., Duncan J. L., Hu S. J.: *Mechanics of Sheet Metal Forming.* Butterworth-Heinemann, Oxford, 2002. 82–107.
- [7] Lange K.: *Handbook of Metal Forming.* SME, Dearborn: Michigan, 1985. 19.1–19.23.
- [8] Pearce R.: *Sheet metal forming. Adam Hilger Series on new manufacturing processes and materials.* IOP Publishing Ltd., 1991. 79–88.
- [9] *Metals Handbook* Vol. 4. Forming, 8<sup>th</sup> ed. American Society for Metals, Ohio: Metals Park, 1969.
- [10] Kovács Zs. F., Béres G., Weltsch Z.: *Autóipari DC és DP acélok lézersugaras hegeszthetőségének vizsgálata.* Gradus, 4 (2017) 311–317.

- [11] Swift, H. W.: *Drawing tests for sheet metal*. Proceedings Institution of Automobile Engineers, 34:361 (1939)
- [12] Siebel E., Beisswanger H.: *Deep Drawing*. Carl Hanser, München, 1955.
- [13] Altan T., Tekkaya A. E.: *Sheet Metal Forming – Fundamentals*. ASM International, 2012. 105–127.

# Fabrication of a Laser Welded Waterproof Coating Made of Stainless Steel Foil

Artúr Benjámín ACÉL,<sup>1</sup> Márk WINDISCH,<sup>2</sup> Anna MALOVECZKY<sup>3</sup>

*Bay Zoltán Nonprofit Ltd. for Applied Research. Budapest, Hungary*

<sup>1</sup> [artur.ancel@bayzoltan.hu](mailto:artur.ancel@bayzoltan.hu)

<sup>2</sup> [mark.windisch@bayzoltan.hu](mailto:mark.windisch@bayzoltan.hu)

<sup>3</sup> [anna.maloveczky@bayzoltan.hu](mailto:anna.maloveczky@bayzoltan.hu)

---

## Abstract

The purpose of this engineering design was to fabricate a waterproof coat for a carbon fibre reinforced polymer component. Austenitic stainless steel foil with 50µm thickness was used as the raw material. Deep-drawn elements that fit the geometry of the given part were welded together to form the coat. The deep drawing tools and the welding machine were self-designed and manufactured. The cutting of the blank and then the welding technology of the deep-drawn tablecloths were carried out with a TruMark 5010 marking laser made by Trumpf

**Keywords:** *laser welding, stainless steel, thin foil, micro-welding.*

---

## 1. Introduction

Currently, a trend can be observed in the development and application of increasingly compact and smaller-sized instruments. For this reason, there is a greater need for welding thin steel foils (<100µm). Several articles have been written on the implementation of low power laser beam welding of steel foils. [1, 2, 3]

Based on the welding results of thin films, we have developed a solution for the watertight coating of a carbon fibre reinforced automotive component. Considering the installation requirements, a 50µm thick stainless steel foil was used to form the watertight cover.

## 2. Applied materials and methods

Trumpf TruMark 5010 laser marking equipment was used to cut and weld the films. The solid-state resonator of the laser equipment had a pulse time of 250 ns, an average power of 18.5 W, a beam wavelength of 1064 nm, a repetition frequency of 20 kHz for cutting and 100 kHz for welding.

Later, the average power of 18.5 W was used to determine the welding powers.

A Keyence VHX 2000 digital optical microscope was used to examine the cross section of the

seams. The metallographic preparation of the seams was performed by sanding and polishing, followed by etching with royal water to show the fabric structure.

## 3. Technological steps

The carbon fibre reinforced plastic part to be covered was cylindrical and had a shoulder. Due to the geometry of the part, there were two possibilities for forming the cover. As a first solution, we designed 2 parts. One part was the cover of the cylindrical part, the other part was the shell and the flange. However, these two-part versions were discarded due to the poor deformation properties of the 50µm thick corrosion-resistant film. Due to the poor deformation property, the film is easily torn during shaping. As a second solution, three components were designed. In this case, we also kept the cover part, but we designed two parts to cover the mantle and the shoulder. To make the part, we needed tablecloths. These tablecloths were deep-drawn with the tools, and then the deep-drawn pieces were welded together using the welding device.

### 3.1. Cutting of blanks

The cutting of the tablecloths was carried out using the TruTops Mark program of the laser beam equipment used.

The laser beam cutting power was determined at 18.5 W and the welding speed at 200 mm/s in order to cut the film safely with the laser beam (sublimation cutting). The laser beam treatment was repeated ten times in succession on a sample at the same setting.

### 3.2. Deep—drawn tools

Due to the possible wrinkling of the plate during deep drawing (due to the design of the deep drawing tools), the size of the drawing gap was optimized for the appropriate clamping force. The centering of the discs was achieved with a 100 $\mu$ m shoulder prepared for this purpose. The tension and guide rings were bolted together.

The following parts were made from the tablecloths after deep drawing. **Figure 3.** shows the deep-drawn flange and **Figure 4.** shows the deep-drawn cover. **Figure 5.** shows the welded mantle.



**Figure 3.** The successfully deep-drawn ring.



**Figure 4.** The successfully deep-drawn cover.

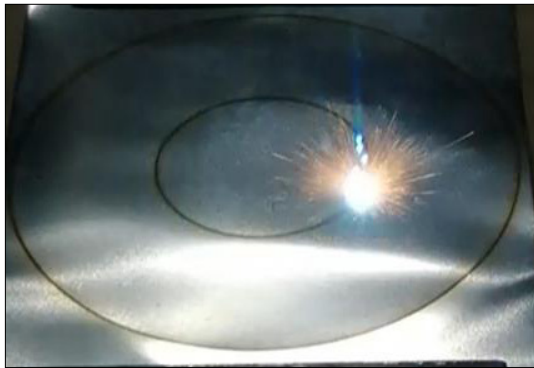


**Figure 1.** Blank cutting with TruMark 5010.

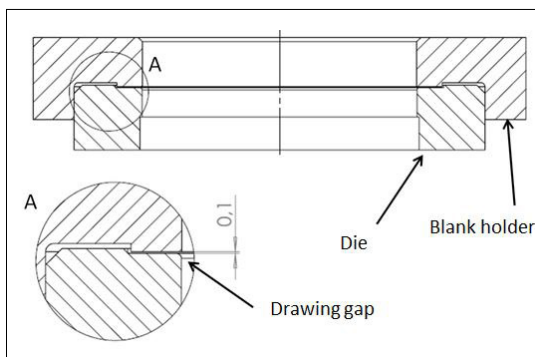


**Figure 2.** Sketch of a deep drawing tool.



**Figure 5.** Successfully welded mantle with mantle welder fixture.

### 3.3. Welding

Two devices were designed for welding the parts. With the help of one device, the seam of the mantle was formed, while with the other, the finished piece was welded together from the three parts. During welding, the average power of the laser beam was determined to be 16.65 W and the welding speed of 55 mm/s to form the sheath seam. To form the seam of the cylinder shell, the average power of the laser beam was determined to be 17.58 W and the welding speed determined to be 55 mm/s. **Figure 6.** shows the welding of the finished part.

### 3.4. Presentation of formed seams

Deep seam laser welding usually requires a so-called continuous laser beam. In our case, the laser beam equipment was pulsed. In order to make the laser beam as close as possible to continuous operation decoupling, we used the largest possible pulse mode of 100 kHz. In the series of experiments, the welding speed and the average power of the laser beam were optimized.

The optimum average power of the pulsed laser beam was found to be between 16.65 W and 17.58 W. The welding speed was chosen to be 55 mm/s. **Figure 7.** shows the geometry of a weld welded with a laser power with an average power of 16.65 W. The lack of material on the crown side is not relevant to the function of the seam. The overlapping thin films were fused to their full thickness by the laser beam. The cross-sectional shape of the seam made with a power of 17.58 W can be observed in **Figure 8.** In this case, like the crown side, the lack of material appears on the root side. Considering the total thickness of the films, the material fused.

## 5. Conclusions

With the Trumpf TruMark 5010 laser device, it was possible to cut out geometries with a defined geometry from a 50µm thick stainless steel foil. These placemats were formed with our own deep drawing tool. The deep-drawn parts were successfully welded together. The finished part is shown in **Figure 10.**

The water tightness of the finished parts is currently being tested. In the future, part of the test plan will be to increase seam overlap on the Trumpf TruMark 5010. A limitation of the further development of the technology is the lack of synchronous control of the laser beam coupling and the CNC rotary shaft.

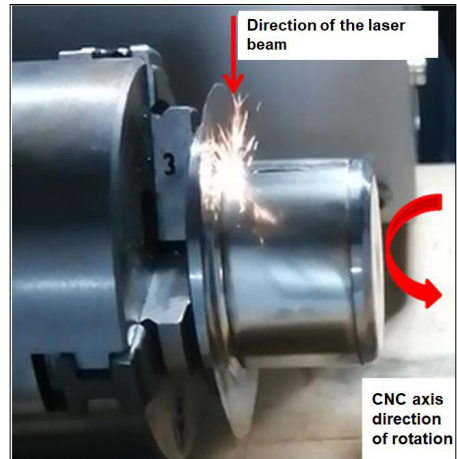


**Figure 6.** Circular seam welding of the mantle and flange.

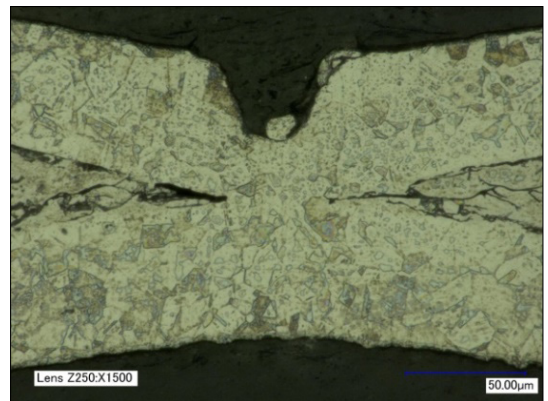


**Figure 7.** Sectional metallographic image of a seam created with a laser beam with an average power of 16.65 W and a welding speed of 55 mm/s.

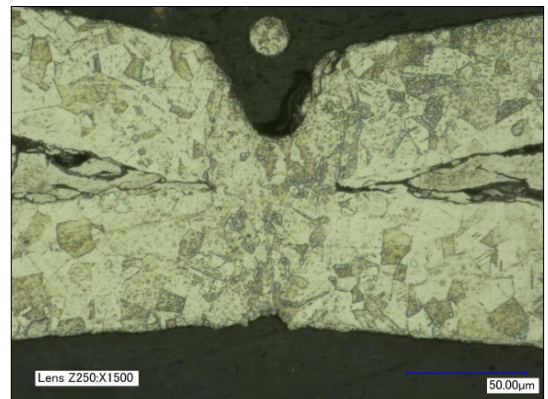


**Figure 8.** Sectional metallographic image of a seam created with a laser beam with an average power of 17.58 W and a welding speed of 55 mm/s.

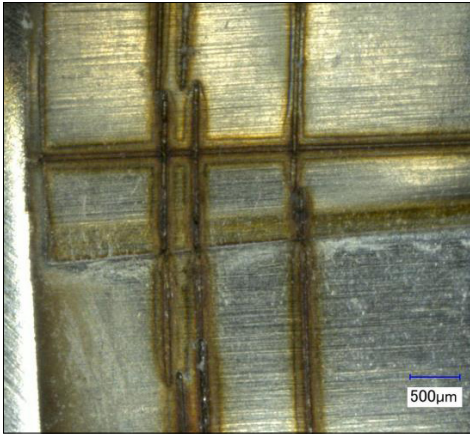


**Figure 9.** Weld seams at the overlap of the mantle and flange.



**Figure 10.** Waterproof cover with three seams.

### Acknowledgments

This research was supported by the European Union and the Hungarian State, co-financed by the European Regional Development Fund in the framework of the GINOP-2.2.1-15-2017- 00090 project, titled „E-mobility from Miskolc: Improvement of Coolant Pump and Engine Cooling Fan Taking into Account the Higher Quality Requirements in Electric Vehicles.

### References

- [1] Pakmanesh M. R., Shamanian M.: *Optimization of pulsed laser welding process parameters in order attain minimum underfill and undercut defects in thin 316L stainless steel foils*. Optics and Laser Technology, 99. (2018) 30–38.  
<https://doi.org/10.1016/j.optlastec.2017.09.047>
- [2] Abe N., Funada Y., Imanaka T., Tsukamoto M.: *Micro welding of thin stainless steel foil with a direct diode laser*. Transactions of JWRI, 34/1. (2005).
- [3] Ventrellaa V. A., Berrettab J. R., Rossib W.: *Pulsed Nd:YAG laser seam welding of AISI 316L stainless steel thin foils*. Journal of Materials Processing Technology, 210/14. (2010) 1838–1843.  
<https://doi.org/10.1016/j.jmatprotec.2010.06.015>

# Design and Manufacture of a Microfluidic Cell To Be Used With a Spectroscopic Ellipsometer

Tamás BÍRÓ<sup>1</sup>, József Bálint RENKÓ<sup>2</sup>

<sup>1</sup> Budapest University of Technology and Economics, Department of Materials Science and Engineering, Budapest, Hungary, [biro.tamas@edu.bme.hu](mailto:biro.tamas@edu.bme.hu)

<sup>2</sup> Budapest University of Technology and Economics, Department of Materials Science and Engineering, Budapest, Hungary, [renko.jozsef@edu.bme.hu](mailto:renko.jozsef@edu.bme.hu)

---

## Abstract

In material testing and manufacturing processes, creating thin layers is a widely used method for structure development or for surface treatment purposes. Despite its widespread use, the physical background of the layer development process is currently under-researched. Its examination requires the development of procedures and tools that, in combination with the existing tools, can help to understand these processes. The development of microfluidic cells is a way to solve this problem. In this paper, a newly developed microfluidic cell is presented, which also offers a solution to several problems encountered when using previous designs.

**Keywords:** *microfluidic cell, design, manufacture, spectroscopic ellipsometry.*

---

## 1. Introduction

Various etching methods are widely used in metallography. One of the most common types of these is colour etching [1]. During colour etching, the etchant reacts with the surface of the polished sample to form a thin transparent layer. The light reflected from the surface of this film interferes, causing a visible, cyclic colour change of the individual grains. The orientation of these grains can be calculated using the etching speed [2], [3]. During the etching process, microfluidic cells are used to record surface colour change. The phenomenon occurring on the surface can be observed not only with an optical microscope but also with a spectroscopic ellipsometer [3]. Concepts aimed at achieving this were previously put forward, but they could not be put into practice due to manufacturing limitations [1]. In our work, we aimed to design and manufacture a microfluidic cell that allows the observation of the rapid exchange of the surface and extends the use for nanometer-precision spectroscopic ellipsometry [4] while eliminating the errors of previous concepts. In addition, the positioning of the sample can be performed with an optical microscope.

## 2. Design and manufacture

The work began with defining the requirements. The dimensions of the embedded sample to be examined and the geometrical parameters of the Woollam M-2000DI spectroscopic ellipsometer used for the tests were given. The following size constraints posed a major design challenge. The height of the device could not exceed 45 mm. A channel at least 3 mm in diameter had to be provided along the path of the light, in which the border between different phases had to be perpendicular to the path of the light. Otherwise the ellipsometer could not detect the previously diffracted light. Finally, the aim was to create the smallest possible internal cavity, as it had to be filled with etchant before any measurement. However, the production of mechanical parts becomes cumbersome within this small size range.

### 2.1. The device

The schematic structure of the device is shown in **Figure 1**. It can be divided into three main parts: the polydimethylsiloxane (PDMS) cell, the welded frame structure, and the sample tray.

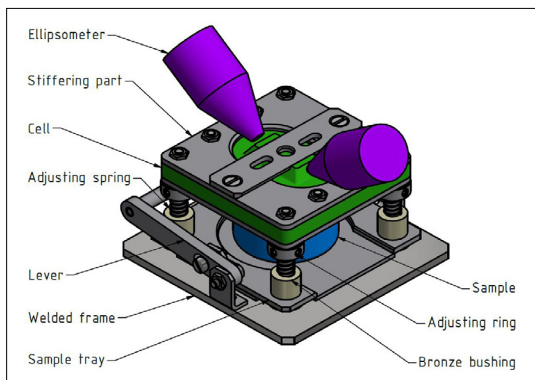


**Figure 1.** The schematic structure of the device.

## 2.2. Microfluidic cell

The most important part of the device is the cell, where the etching process and the examination occur (Figure 2). It must be made of a chemically inert, preferably transparent, dimensionally stable material. The choice has been made for the previously used PDMS [1]. The PDMS cell was made by molding, so the geometry had to be manufactured with high precision while avoiding undercut surface elements. In addition, the molds must be heat resistant up to 180 °C. Due to their design, molds can be made by different methods such as additive manufacturing [5] or 5-axis CNC machining [6]. For economic reasons, the mold created with additive manufacturing was chosen.

Several aspects had to be considered while designing the cell. One of the main disadvantages of the previous models was that the initial stage of the etching process was not observable, as the filling of the cavity took a relatively long time [1]. Its volume has been reduced from 851 mm<sup>3</sup> to 90 mm<sup>3</sup>. Thus, filling the main cavity under the same flow conditions takes only a few seconds within the new design. By forming surfaces perpendicular to the path of the light beam, refraction at the boundaries of the different media can be avoided or minimized.

In spectroscopic ellipsometry, the maximum intensity of the light beam reflected from the surface of the sample can be obtained at an angle of incidence of 55° [7], [8]. The light beam enters and leaves the cell, as shown in section A-A of Figure 2. The inner cavities for the light beam are closed with a laminated glass plate. The channels to introduce and drain the etchant are formed perpendicular to the previous direction, indicated by section B-B in Figure 2. The two channels in section B-B are offset relative to each other, which

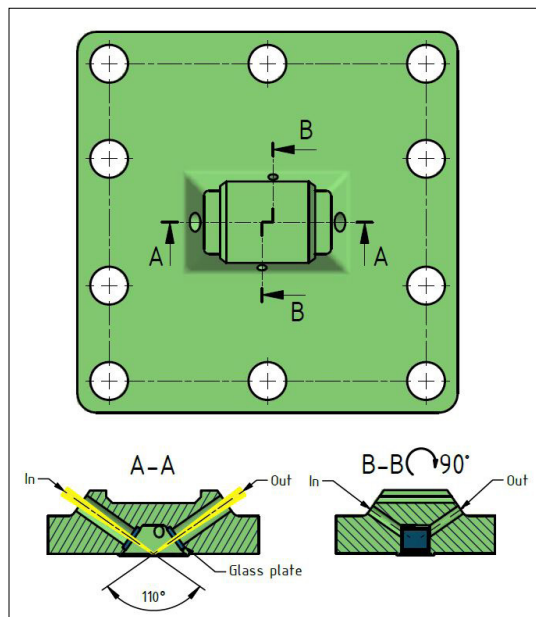


**Figure 2.** PDMS cell; Section A-A: the path of the light beam; Section B-B: the path of the etchant.

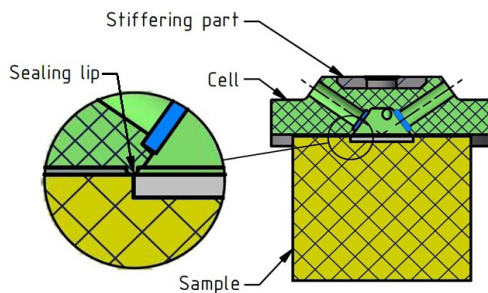


**Figure 3.** The sealing lip between the sample and the cell.

prevents the etchant from stagnating.

The seal between the sample surface and the cell is provided by a 0.3 mm high sealing lip formed in the PDMS. As a result of the spring pressure, the plane of the sample thus enters the point of intersection of the optical axes of the ellipsometer (Figure 3).

## 2.3. Frame structure

The elastic deformation of the cell, and thus the change of the geometrical conditions necessary for the measurement, is prevented by a rigid, welded frame structure made of steel. The precise positioning was ensured by plane grinding the bottom plate after welding, compensating the thermal deformation caused by welding.

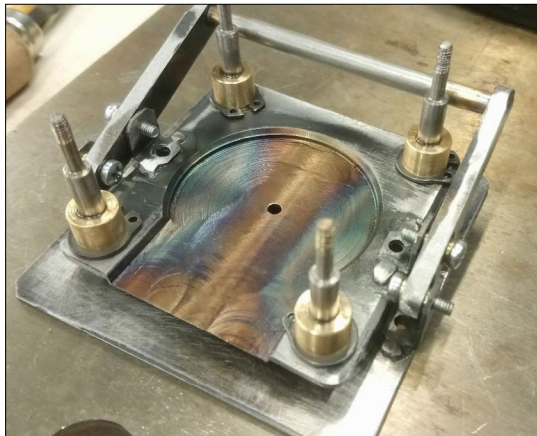


**Figure 4.** The sample tray and the lifting mechanism are built into the frame structure.

The frame ensures the parallelism and precise running of the sample tray with the microfluidic cell. The exchange and positioning of the sample are facilitated by the developed spring mechanism (Figure 4). The correct tightness can be adjusted by changing the spring force by prestressing the pairs of springs connected in parallel below and above the sample tray.

The positioning on the surface of the sample is possible by an inspection hole formed in the upper stiffening part. This can be combined even with an optical microscope to increase accuracy. Any arbitrary location can be found on the surface area, so the ellipsometer can precisely target any point on the prepared sample.

Another design consideration was for the frame structure to form a whole assembly unit even without the cell. This allows the combination of the frame with different cell structures as part of a further development process (Figure 5).

### 3. Results

As a result of our work, a prototype of the microfluidics cell was created. After assembling the mechanical parts, the device was adjusted, which meant that the springs ensured the sealing between the sample and the cell. The construction mechanically satisfies the needs arising during the design. The sample tray and the sample can be moved, changed, and positioned without moving the device.

### 4. Conclusions

Using previous experience of microfluidic cells, a redesigned experimental unit was created to



**Figure 5.** The assembled device without the PDMS cell.

study the etching processes. The new device can be combined with both optical microscopy and spectroscopic ellipsometry. The manufactured frame structure is easy to install, so it can be suitable for inserting new, possibly modified cells. Subsequent, repeated improvements to the construction can provide for metallography, a tool that can open a new chapter in the examination of etching processes.

### Acknowledgement

The publication of the work reported herein has been supported by the NTP-SZKOLL-20-0067 National Talent Programme of the Ministry of Human Capacities.

### References

- [1] Renkó J. B., Bonyár A., Szabó P. J.: *Mikrofluidika cella fejlesztése folyadékfázisú vékonyréteg leválasztás nyomkövetésére*. Acta Materialia Transylvanica, 3/2. (2020) 94–98. <https://doi.org/10.33924/amt-2020-02-08>
- [2] A. Bonyár, P. J. Szabó: *Correlation between the grain orientation dependence of color etching and chemical etching*. Microscopy and Microanalysis, 18/6. (2012) 1389–1392. <https://doi.org/10.1017/S1431927612013554>
- [3] Bonyár A., Renkó J., Kovács D., Szabó P. J.: *Understanding the mechanism of Beraha-I type color etching: Determination of the orientation dependent etch rate, layer refractive index and a method for quantifying the angle between surface normal and the <100>, <111> directions for individual grains*. Materials Characterization, 156. (2019) 109844. <https://doi.org/10.1016/j.matchar.2019.109844>
- [4] Tompkins H. G.: *A User's guide to Ellipsometry*. Academic Press, Inc., Mesa, Arizona, 1993. XIII–XV.

- [5] Bonyár A., Sántha H., Ring B., Varga M., Kovács J. G., Harsányi G.: *3D Rapid Prototyping Technology (RPT) as a powerful tool in microfluidic development*. Procedia Engineering, 5. (2010) 291–294.  
<https://doi.org/10.1016/j.proeng.2010.09.105>
- [6] H. D. Cho, Y. T. Jun, M. Y. Yang: *Five-axis CNC milling for effective machining of sculptured surfaces*. International Journal of Production Research, 31/11. (1993) 2559–2573.  
<https://doi.org/10.1080/00207549308956883>
- [7] Tompkins H. G. , Hilfiker J. N.: *Spectroscopic ellipsometry: Practical application to thin film characterization*. Momentum Press, LLC, New York, 2016. 31–55.
- [8] Fujiwara H.: *Spectroscopic Ellipsometry: Principles and Applications*. John Wiley & Sons Ltd, Chichester, 2007. 81–120.

# Production of Biopolymer Foams Based on Polylactic Acid Plasticized With Lactic Acid Oligomer

Katalin LITAUSZKI,<sup>1</sup> Ákos KMETTY<sup>1,2</sup>

<sup>1</sup> *Budapest University of Technology and Economics, Faculty of Mechanical Engineering, Department of Polymer Engineering, Budapest, Hungary, [litauskik@pt.bme.hu](mailto:litauskik@pt.bme.hu)*

<sup>2</sup> *MTA–BME Research Group for Composite Science and Technology, Budapest, Hungary, [kmetty@pt.bme.hu](mailto:kmetty@pt.bme.hu)*

## Abstract

In our work, we modified polylactic acid biopolymer using oligomeric lactic acid. We have successfully plasticized polylactic acid compounds with 5, 10, 20 wt% oligomeric lactic acid using a liquid dosing system connected to a compounder extruder. The produced compounds were foamed with an exothermic chemical foaming agent. The density of the foams was measured and the fracture surfaces were examined by electron microscopy to assess the homogeneity of the cell structure. Based on this, we believe that the plasticising effect of oligomeric lactic acid is undeniable, but a processing temperature of 190 °C is not optimal for the foaming process. In the future, the production of biopolymer foam structures with a higher density reduction can be achieved by reducing and optimizing the foam processing temperature.

**Keywords:** *poly lactic acid, plasticised, extrusion, foam.*

## 1. Introduction

Nowadays, polymers play a very important role. In 2019 368 million tons of polymer raw material was produced [1]. The high use of polymers, almost 40% in the case of packaging, raises serious waste management issues. Biopolymers offer a potentially promising raw material type in terms of environmental impact. Biopolymers are biodegradable polymers that can be produced from a renewable resource, but are also biodegradable. Because of these benefits, they are at the forefront of research into promising alternatives to petroleum-based polymers, specifically for short-life-cycle products. Polylactic acid (PLA) is one of the most promising biopolymer feedstocks, being produced in large quantities (140,000 tonnes/year), thus having a relatively low price (~2 \$/kg) compared to other biopolymers [2], in addition it can be processed with conventional polymer processing equipment. In order to expand the applicability of polylactic acid, it is necessary to modify its disadvantageous properties. One of the biggest disadvantages of PLA is its brittleness and low elongation at break. A suitable method to improve these properties is the internal or external

plasticisation of PLA. In this case, after polymerization, the properties of the polymer are modified without any chemical reaction. In a system internally plasticised in this way, we did not change the polymer chain but the plasticizer molecules are incorporated between the polymer chains that interact with the polymer molecules, thus changing the PLA's properties [3]. In connection with the plasticisation of PLA, several plasticizers have been tested, such as poly (ethylene glycol) with different molecular weights [4, 5] and citrate ester [5]. One of the most promising plasticizers is the oligomeric version of polylactic acid itself. The repeating unit of oligomeric lactic acid (OLA) and PLA is the same, the only difference is in the number of repeating unit, i.e. in its molecular weight. While an average polymer contains repeating unit in the order of one hundred thousand, in the case of oligomers it is only a few thousand, therefore their molecular weight is lower. The production of polylactic acid-based foam, the reduction of the brittleness of the produced foams and the increase of their energy absorption capacity are still actively researched areas. In terms of foaming, the less well-researched chemical foaming is

typically carried out with an exothermic foaming agent [6]. The most common exothermic foaming agent is azodicarbonamide [6]. One of the advantages of the chemical foaming process is that it is not necessary to modify the extruder. Blending polylactic acid with oligomeric lactic acid may be suitable for reducing the brittleness of foam, so foaming of PLA/OLA blends may be the focus of particular interest.

## 2. Materials, processing and methods

For the experiment, we selected NatureWorks LLC's Ingeo 4032D biopolymer. This polylactic acid is recommended for extrusion processing. The D-lactide content of this PLA is 1.4 % and it is a crystalline polymer [7]. It has a density of 1.24 g/cm<sup>3</sup> [8]. The lactic acid oligomer was Glyplast OLA 2 manufactured by Condensia with ester content >99 %. Its density is 1.10 g/cm<sup>3</sup>. Its viscosity at 40 °C is 90 mPas. The selected OLA type was added to the PLA at 5, 10 and 20 % by weight. The foaming agent was Tracel IM 3170 MS, manufactured by Tramaco GmbH, in the form of granules. This foaming agent is an exothermic chemical foaming agent containing azodicarbonamide (ADCA). Its thermal decomposition is between 147 and 212 °C [9].

For compounding we used a Labtech LTE 26-44 twin-screw extruder equipped with a Labtech IZ-120/VS liquid dispenser, which was used to deliver the liquid directly into the melt. The plasticiser was preheated to 70 °C. OLA was injected into the polylactic acid melt at the 3rd zone of the twin screw extruder to promote homogeneous mixing. The temperature profile was 180/185/185/190/190/190/195/195/200/200/200 °C. The extruder screw speed was 25 rpm and the feeder speed was 8.5 rpm. The extruded cord was granulated with a Labtech LZ-120/VS type granulator, which was used as a raw material for the extrusion foaming. In each case, the raw materials were dried at 80 °C for 6 hours before manufacture using a WGL-45B (Huanghua Faithful Instrument Co., China) dryer.

A Collin Teach-Line ZK-25T twin-screw extruder was used to produce the foam. Based on our preliminary experiments [10], Tracel IM 3170 MS type CBA was mixed with 2 % by weight of PLA granules by dry mixing. The temperature profile was 155/160/175/190/190 °C. The screw speed was 10 rpm.

Differential scanning calorimetry (DSC) measurements were performed using TA Instruments Q2000 DSC equipment. The test temperature range was (-20) to 200 °C, which was determined

based on the expected glass transition temperature according to the literature. The heating rate was 5 °C/min. The weights of the samples were between 3 and 6 mg. The measuring atmosphere was nitrogen.

Thermogravimetric analysis (TGA) was performed using TA Instruments Q500 equipment. The temperature range was 50 to 600 °C. The heating rate was 10 °C/min. The weight of the samples was between 3 and 6 mg. The measuring atmosphere was industrial grade air at a flow rate of 60 mL/min.

An AR2000 type oscillation rheometer manufactured by TA Instruments (USA) was used for rheological analysis of the raw materials. The measurement was performed between parallel discs of steel. The test temperature was 190 °C. The tested frequency range was 1-100 Hz, the applied stress was 10 %. The diameter of the specimen was a 25 mm with the thickness of 1-2 mm.

We created a cryogenic fracture surface of the foam structures therefore, we were able to examine the cross section of the foams. We created scanning electron microscopy (SEM) images. SEM images were taken with a JEOL JSM 6380LA scanning electron microscope manufactured by Jeol Ltd. We used an accelerating voltage of 10 kV. The cryogenic fracture surface of the samples was coated with a gold-palladium alloy under vacuum with an Argon gas purge at 10 mA/Pa.

The density of the compounds and foams was measured with a 10 ml graduated cylinder in 0.1 ml increments. The measuring medium was distilled water. We used an OHAUS Explorer type of balance with a weighing range of 110 g and a measuring accuracy of 0.1 mg.

Cell population density ( $N_c$ ) was calculated based on Equation (1), where  $n$  is the number of cells in the microscopic image of the fractured surface,  $M$  is the magnification, and  $A$  is the cross section of the foam [cm<sup>2</sup>]. ER denotes expansion [11].

$$N_c = \left( \frac{n \cdot M^2}{A} \right)^{\frac{3}{2}} \cdot ER \quad (1)$$

## 3. Characterisation of the compounds

We performed several measurements on the produced compounds to evaluate their morphological, thermal, and rheological properties. The morphology of the manufactured compound was evaluated by DSC analysis to investigate the effect of plasticizer content on the glass transition ( $T_g$ ), cold crystallization ( $\Delta H_{cc}$ ) and crystal melting ( $T_m$ )

temperatures. The resulting set of DSC curves is shown in **Figure 1**, which shows the DSC curves obtained during the first heating of compounds softened to varying degrees of OLA. One of the easy-to-detect and quantifiable properties of plasticizers is that the glass transition temperature is shifted to a lower temperature. There is a clear tendency for the glass transition temperature to shift towards lower temperatures, and the peak temperature for cold crystallization and the peak temperature for crystal melting show a similar trend. This effect was observed as a result of plasticising with OLA. The  $T_g$  change is the biggest in the case of 20 wt% OLA content (from 61 °C to 26 °C) as expected.

Furthermore, with the addition of 5 wt% OLA, it can be observed that no glass transition temperature (62 °C) has occurred as a result of this OLA addition. Compared to its results in the literature, we managed to achieve a lower  $T_g$  than reported by Sinclair [12], but we failed to achieve the glass transition temperatures of 37 and 18 °C described by Martin and Avérous with the addition of 10 and 20 wt% OLA, respectively [13]. The  $T_g$  temperature between 36–40 °C was achieved by Burgo et al. with the use of 15 wt% OLA. These values are consistent with our measurement results.

The TGA curves of the compounds made of PLA and PLA/OLA are shown in **Figure 2**. As we added lower molecular weight chains to our PLA matrix in the form of oligomeric lactic acid the temperature at the initial 5 % weight loss is decreased as we expected. The reason for this is that these lower molecular weight chains are more mobile and decompose under lower temperature. It is also important to note that the temperature for 50% weight loss changed only slightly, in which case the curves run together with only a small deviation and their final decomposition temperature is the same, so these values are related to the PLA values and do not depend on plasticizer content.

Adequate melt strength is of paramount importance during foaming, since with low melt strength the polymer matrix cannot retain the formed cells, they collapse. In contrast, if the melt strength is too high, the foaming agent will not be able to expand the nucleated cell sufficiently. Therefore, the viscosity of the manufactured compounds was investigated. **Figure 3** shows the absolute value of the complex viscosity of compounds made from PLA as a function of angular velocity. The values corresponding to an angular velocity of 100 rad/s have been highlighted, as this value corresponds in order of magnitude to

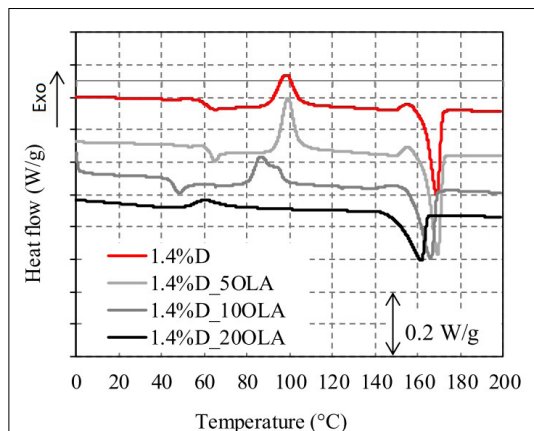


**Figure 1.** Heat-flow curves as the function of temperature in the case of PLA and OLA containing samples based on DSC measurements.

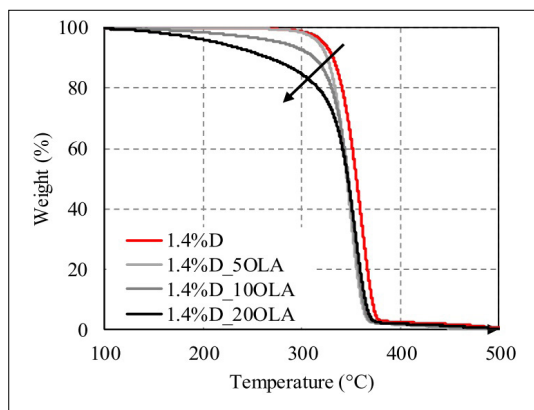


**Figure 2.** Weight loss curves as the function of temperature in the case of PLA and OLA containing samples based on TGA measurements.

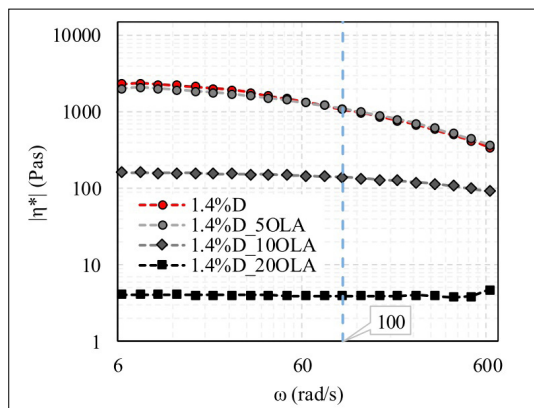


**Figure 3.** Complex viscosity curves as the function of angular velocity in the case of PLA and OLA containing samples based on oscillation rheometer measurements.

the shear rate occurring during extrusion. This 100 rad/s is lower than the shear rate of an average extrusion, but due to the low screw speed, it can be approximated in this case. It can be observed that the addition of 5 wt% OLA does not significantly affect the viscosity of the sample, in contrast to the 10 wt% and 20 wt% compounds, a significant decrease results, it can be concluded that a compound containing 5 wt% of OLA is expected to be suitable for stable foaming, and it is possible to form a foam from the system containing 10 wt% of OLA with other foaming agents at lower temperatures.

#### 4. Characterisation of the compounds

During foaming, reference samples and PLA-based foams containing 2 wt% CBA were produced in a continuous operation with a twin-screw extruder. We first examined the density of the foams. The results of the density measurements are shown in Figure 4. There is a clear tendency that an increase in plasticiser content causes an increase in density due to the effect of OLA on viscosity. The lower polymer melt strength is unable to maintain the cell structure, so they collapse and coalesce. The mixture containing 20 wt% OLA also proved to be unmanageable, unprocessable during foaming. The lowest density was obtained with the PLA without OLA using 2 wt% CBA ( $0.6 \text{ g/cm}^3$ ).

Figure 5 shows scanning electron micrographs of cryogenic fractured surfaces of foams. The effect of the increasing plasticizer content on viscosity can be observed. Compared to the reference foam, 5 wt% OLA did not significantly change the cell structure, but 10 wt% plasticizer reduced the

melt viscosity of the polymer to such an extent that the collapse of the cells led to the formation of the giant bubble shown in the picture and the production was not continuous. The melt could not contain the generated foaming gas. It can also be observed that as a result of cooling, smaller cells formed in an outer layer, while larger cells could form inside the sample because, they did not solidify as quickly as the outer ones.

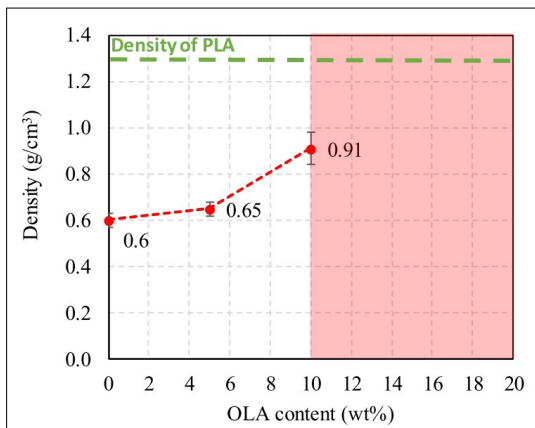


Figure 4. Density results of foams containing PLA and OLA as a function of OLA content.

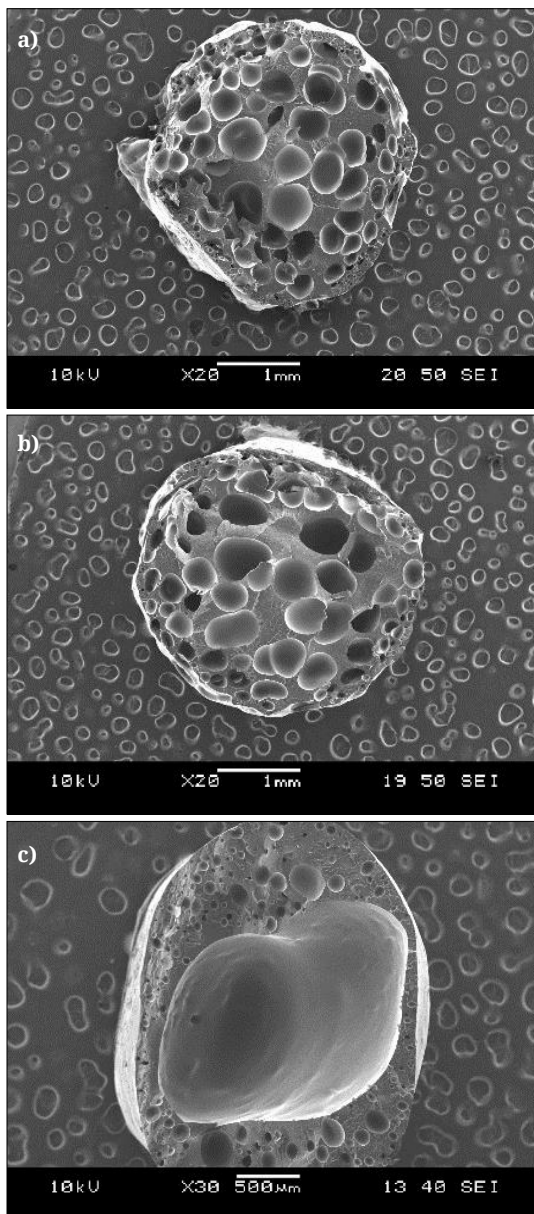
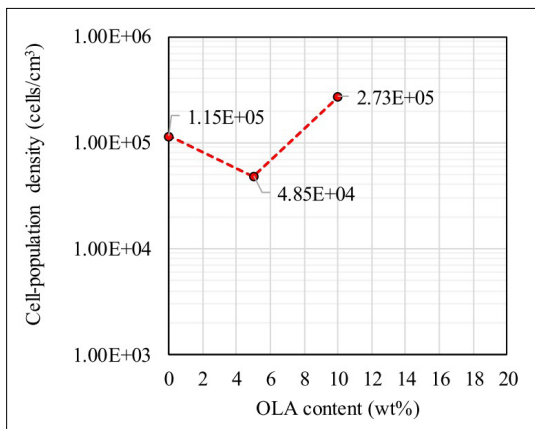


Figure 5. SEM imaged of foams from top to bottom: with a) 0, b) 5, c) 10 wt% OLA content.



**Figure 6.** The cell-population density values of foams containing 0, 5, 10 wt% OLA.

Based on SEM images, cell population density was calculated. **Figure 6** shows the cell-population density as a function of OLA content. The highest cell population densities resulted in the samples containing 10 wt% OLA, and then, with slightly lower cell population densities in the case of reference foam. The cell-population densities calculated by us achieved a cell-population density of the order of  $10^5$ , which was in the same order that was achieved by Julien et al. in the case of chemically foamed PLA [14]. However, this alone does not characterise the foamed structures. It should be treated in conjunction with SEM images, because it does not provide specific information on the homogeneity, size and distribution of the cell structure. In this case, this will be especially true. Since at 10 wt% OLA dosing a large number of small cells were formed, but no homogeneous foam structure was formed. However, at a dose of 5 wt% OLA, the cell structure shows a favourable homogeneity.

## 5. Conclusions

We successfully produced PLA compounds plasticised with 5, 10, 20wt% OLA using a liquid dispenser. We pointed out, using DSC measurements, that the glass transition temperature-lowering effect of OLA is in line with the results presented in the literature. The highest rate of  $T_g$  reduction was achieved at 20 wt% OLA administration (26 °C). This shift was also observed at in the case of  $T_{cc}$  and  $T_m$ . Thermogravimetric analysis was used to examine the thermal stability of the manufactured compounds and, as expected, their decomposition temperatures shifted in the direction of the lower ones under the influence of OLA.

Furthermore, rheological measurements were performed to characterise the viscosity of the different PLA/OLA formulations, as this is closely related to the foamability of the given compound. Rheological measurements and subsequent foamability were consistent with each other. The density of the formed foams were measured, and the fracture surfaces were examined by scanning electron microscopy to assess the homogeneity of the cell structure and the cell-population density. Based on all this, it is believed that the plasticisation efficiency of OLA is undeniable, but the processing temperature of 190 °C is not suitable for foaming PLA/OLA compounds. In future, reducing and optimizing the production temperature could be a promising step forward.

## Acknowledgment

We would like to thank Tramaco GmbH (Germany) and INTERDIST Kft. for the Tracel IM 3170 MS foaming agent, the National Office for Research, Development and Innovation for the funds K-132462 and NVKP\_16-1-2016-0012 and János Bolyai Research Scholarship of the Hungarian Academy of Sciences.

## References

- [1] PlasticsEurope: Plastics - the facts 2019: An analysis of European plastics production, demand and waste data, (2020).
- [2] Plastics Insight: *Polylactic Acid Properties, Production, Price, Market and Uses*. (accessed on: 2020.12.12.)  
<https://www.plasticsinsight.com/resin-intelligence/resin-prices/polylactic-acid/>
- [3] Edmund H. I., Herman F. M.: *Principles of Plasticization* In: *Plasticization and Plasticizer Processes* (eds.: Platzer N. A. J.) American Chemical Society, Philadelphia, USA, Vol 1, (1965).
- [4] Pillin I., Montrelay N., Grohens Y.: *Thermo-mechanical characterization of plasticized PLA: Is the miscibility the only significant factor?* *Polymer*, 47/13. (2006) 4676–4682.  
<https://doi.org/10.1016/j.polymer.2006.04.013>
- [5] Kulinski Z., Piorowska E.: *Crystallization, structure and properties of plasticized poly(l-lactide)*. *Polymer*, 46/23. (2005) 10290–10300.  
<https://doi.org/10.1016/j.polymer.2005.07.101>
- [6] Lee S.-T., Park C. B.: *Foam Extrusion: Principles and Practice*. CRC Press, Boca Raton (2014).
- [7] Kolstad J. J., Vink E. T. H., Wilde D. B., Debeer L.: *Assessment of anaerobic degradation of Ingeo polylactides under accelerated landfill conditions*. *Polymer Degradation and Stability*, 97. (2012) 1131–1141.  
<https://doi.org/10.1016/j.polymdegradstab.2012.04.003>

- [8] Huang C., Thomas N. L.: *Fabricating porous poly(lactic acid) fibres via electrospinning*. European Polymer Journal, 99. (2018) 464–476.  
<https://doi.org/10.1016/j.eurpolymj.2017.12.025>
- [9] Kmetty Á., Litauszki K., Réti D.: *Characterization of Different Chemical Blowing Agents and Their Applicability to Produce Poly(Lactic Acid) Foams by Extrusion*. Applied Sciences, 8. (2018) 1–17.  
<https://doi.org/10.3390/app8101960>
- [10] Litauszki K., Kmetty Á.: *Characterization of chemically foamed poly(lactic acid)*. In: ,OATK. Balatonkenese, Materials Science and Engineering 903. (2020) 012018.  
<https://doi.org/10.1088/1757-899X/903/1/012018>
- [11] Xu X., Park C. B., Xu D., Pop-Iliev R.: *Effects of die geometry on cell nucleation of PS foams blown with CO<sub>2</sub>*. Polymer Engineering & Science, 43/7. (2003) 1378–1390.  
<https://doi.org/10.1002/pen.10117>
- [12] Sinclair R. G.: *The Case for Polylactic Acid as a Commodity Packaging Plastic*. Journal of Macromolecular Science, Part A, 33. (1996) 585–597.  
<https://doi.org/10.1080/10601329608010880>
- [13] Martin O., Avérous: L.: *Poly(lactic acid): plasticization and properties of biodegradable multiphase systems*. Polymer, 42/14. (2001) 6209–6219.  
[https://doi.org/10.1016/S0032-3861\(01\)00086-6](https://doi.org/10.1016/S0032-3861(01)00086-6)
- [14] Julien J., Bénézet J., Lafranche E., Quantin J., Bergeret A., Lacrampe M., Krawczak P.: *Development of poly(lactic acid) cellular materials: Physical and morphological characterizations*. Polymer, 53/25. (2012) 5885–5895.  
<https://doi.org/10.1016/j.polymer.2012.10.005>

# Future Structural Materials of High Speed Generators Used in Supercritical CO<sub>2</sub> Based Power Plant Applications

András NAGY,<sup>1</sup> István JANKOVICS,<sup>2</sup> Márton MÁTÉ<sup>3</sup>

<sup>1</sup> University of Dunaújváros, Hungary, [nagyandras@uniduna.hu](mailto:nagyandras@uniduna.hu)

<sup>2</sup> Budapest University of Technology and Economics, Hungary, [ijankovics@vrht.bme.hu](mailto:ijankovics@vrht.bme.hu)

<sup>3</sup> Sapientia Hungarian University of Transylvania, Romania, [mmate@ms.sapientia.ro](mailto:mmate@ms.sapientia.ro)

## Abstract

The aim of this paper is to present the applicability of one of the promising achievements in the fields of materials science and mechanical engineering, which provides a solution to one of the problems of the new generation power plants. One promising area of research aimed at increasing the efficiency of electricity generation is discussed in this article on the characteristics of super-critical carbon dioxide power plant cycles and the properties of high-speed generators that can be used in such power plants. The applicability of amorphous materials in the construction of high-speed electrical machines can solve the efficiency problem of such machines, enabling its use in new generation power plants.

**Keywords:** *supercritical CO<sub>2</sub>, electromagnetic machine, amorphous material.*

## 1. Introduction

The world's demand for electricity is constantly increasing [1]. The rapid spread of industrial automation and electromobility requires the development of an electrical grid. In order to do development near moderate emission of harmful substances, attention must also be paid to increasing the efficiency of power plants in addition to the development of power plant capacity. Today's steam-powered Rankine cycle power plants have more than 100 years of history, but the efficiency of modern power plants is just over 30 % [2]. Further increase in efficiency is only possible with the introduction of new technologies. One promising technology is the use of supercritical carbon dioxide (sCO<sub>2</sub>) as a working fluid in the power cycle. The sCO<sub>2</sub> working fluid promises an excellent opportunity to achieve higher thermodynamic efficiency, up to 47 %, mostly using the Brayton thermodynamic cycle [3]. Due to the properties of sCO<sub>2</sub>, it requires the development of revolutionary power plant equipment, for example, the sCO<sub>2</sub> turbine provides the same capacity as a steam turbine with significantly smaller geometry. As a result, the turbine speed is notably higher, whereas a conventional generator would be driven through a reduction gearbox. In the

case of power plant performance, the efficiency of the transmission impairs the overall efficiency of the energy conversion chain, although the installation and operating costs are also significant. A better solution is to use a high-speed generator, which can be directly driven by the high-speed turbine. With the help of modern power electronic devices, it is possible to generate either 50 Hz or DC voltage from the voltage produced by the generator at a higher frequency than the mains frequency with good efficiency. To bridge long distances, several direct current electric power transmission lines (HVDC) have been built in recent decades. These have the advantage of higher energy transfer, lower losses (no skin effect, interference, etc.) and no need for synchronization, so the distance is not limited by stability problems [4].

The stator of high-speed generators is made of Fe-Si soft magnetic materials, which have unfavourable high-frequency magnetic properties. Due to this, the electromagnetic machine operated at a higher frequency (speed) dissipates more heat due to the increased iron loss; therefore, its efficiency is lower. Materials science research shows [5], that iron-based soft magnetic materials with amorphous structure have significantly

better high-frequency magnetic properties, so that they can be used to build high-efficiency electromagnetic machines with increased efficiency. Generators built using amorphous materials are able to convert mechanical energy from a high-speed sCO<sub>2</sub> turbine into electricity with good efficiency, thus contributing to the industrial application of sCO<sub>2</sub> technology.

## 2. Properties of supercritical carbon dioxide power plants

A thermal cycle using supercritical carbon dioxide (sCO<sub>2</sub>) can help combat climate change and its impact, as the working medium results in higher thermal efficiency at lower investment costs than state-of-the-art steam (Rankine) power cycles. Power plants using the sCO<sub>2</sub> cycle process are compact, it is projected to require a tenth of the space [6]. The unique characteristics of the sCO<sub>2</sub> working fluid are attracting widespread interest, many research groups are dealing with the applications of the technology [7].

If carbon dioxide is kept above its critical temperature and pressure, it enters a supercritical state. In this state, it is characterized by a density close to liquids and a viscosity close to gases, which parameters can also be dramatically modified by a small change in temperature or pressure, so that sCO<sub>2</sub> is a highly efficient working fluid for power cycle. The phase diagram of CO<sub>2</sub> is shown in Figure 1.

The fields of applications of the sCO<sub>2</sub> cycle, which promise to be extremely wide, can be used more efficiently than conventional steam cycles in converting high-temperature thermal energy into electricity.

It can be used, for example, for the development of energy storage systems [8], for the construction of a concentrated solar power plant [9], novel hybrid geo-solar thermal power plant [21], or for waste heat recovery equipment [10].

A further application area is the use in 4<sup>th</sup> generation nuclear power plants as a working fluid for the power cycle. It can be used to build smaller, more efficient nuclear power plants, which is a significant advantage for military nuclear-powered ships and submarines, for instance. The efficiency of such power plants is calculated to reach 47 % [3], and a very significant natural convection flow of sCO<sub>2</sub> is also beneficial from a safety point of view [11]. Several studies have focused on the selection of a high-efficiency power cycle that meets the requirements of 4<sup>th</sup> generation nu-

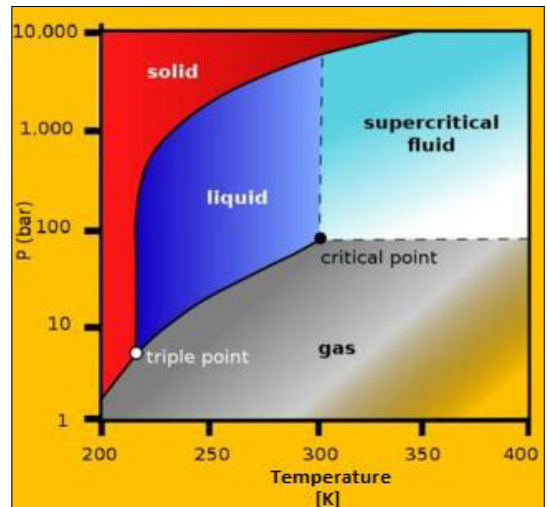


Figure 1. Phase diagram of CO<sub>2</sub>. [13]

clear power plants, and research has shown that the sCO<sub>2</sub> working medium is the best choice in terms of both feasibility and cost, as well as efficiency [12].

The Brayton power cycle is the most suitable cycle for the sCO<sub>2</sub> working fluid. Due to the low pressure ratio (2-3), arrangements with heat exchangers, multistage compressors and intercoolers in several arrangements are investigated by simulations and experiments. Figure 2. shows the arrangement of a heat exchanger Brayton cycle with two compressors, which was also investigated in [15] by measurement and simulation.

Using sCO<sub>2</sub>, the size of power plant equipment is significantly reduced [16], due to the use of high-density working fluid. The sizes of power cycle components are about one-fifth to one-tenth compared to steam-powered plants; Figure 3. shows a proportional comparison of 10 MW sCO<sub>2</sub> and a steam turbine.

Such a reduction in size brings a number of technical problems into account. A group of problems is due to the higher speed of the turbine, which raises the issue of balance and sealing. The seal of the high-speed turbine shaft must seal a large pressure difference at high surface speed, for which non-contact seals (e.g. dry gas seal [17]) are the most suitable.

The use of sCO<sub>2</sub> has the following advantages and disadvantages [19]:

- Simpler and more compact design;
- Higher efficiency;
- Potentially lower investment cost;
- Large heat exchanger surface required;

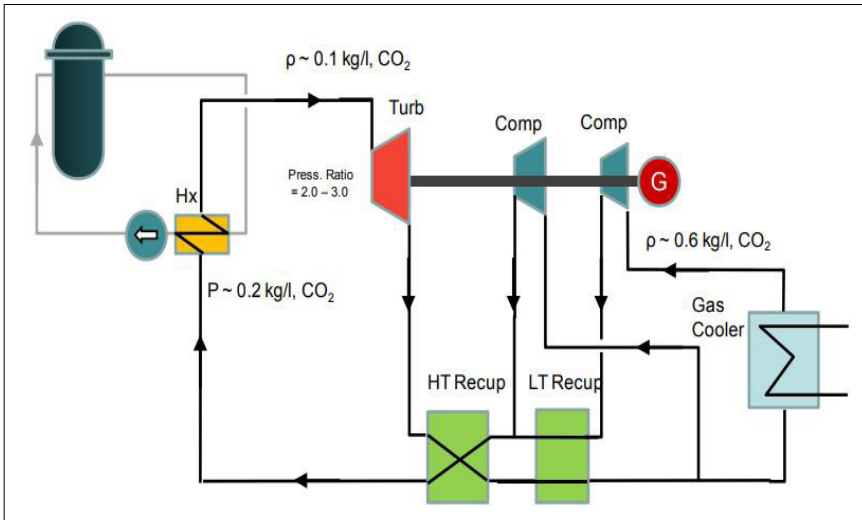


**Figure 2.** Recompression Brayton cycle with sCO<sub>2</sub> working fluid for high temperature nuclear power plants. [14]

- Thick-walled pipes and equipment due to high pressure;
- Turbine and compressor construction difficulties, new types of sealing solutions are required;
- Higher operating costs.

### 3. Losses of high-speed electromagnetic machines

For electromagnetic machines, like generators and electric motors, the increase in power and speed may be limited by mechanical strength limitations, and a significant increase in electric and magnetic losses.

Increasing losses mean increasing heat generation and the requirement for more intensive, more efficient, complex and expensive cooling systems.

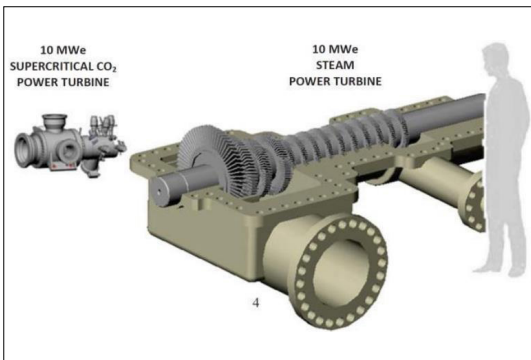


**Figure 3.** Comparison of the size of a 10 MWe steam turbine and a sCO<sub>2</sub> turbine. [18]

Iron loss is an energy loss associated with heat production during alternating magnetization, which increases with AC frequency. According to their physical nature, iron loss can be broken down into three losses:

- hysteresis loss
- eddy current loss, which is negligible in the case of ferrites compared to other losses’,
- loss due to domain wall movement.

A typical B-H curve of Fe-Si soft magnetic material can be seen in Figure 4. [20].

After magnetization of the ferromagnetic materials by excitation, the remnant induction ( $B_r$ ) that appears upon the termination of excitation can only be eliminated by excitation in the opposite direction. The point of intersection of the curve B-H with the horizontal axis is the coercive force ( $H_c$ ), which is the value of the magnetic field

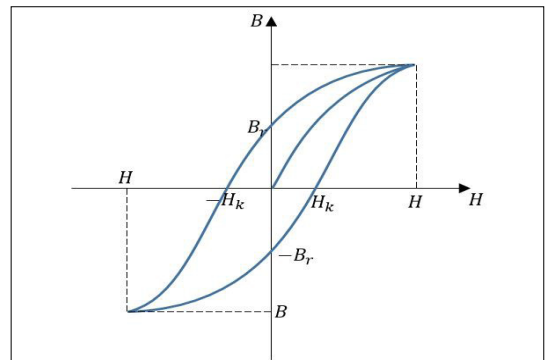


**Figure 4.** B-H curve of ferromagnetic materials.

required to eliminate the remanence induction of the magnet.

In the case of an iron core that is placed in an alternating magnetic field, the change in induction does not take place without loss, the amount of energy required for magnetization is proportional to the area enclosed by the hysteresis curve (Figure 4). In the case of electromagnetic machines, the number of magnetizations in a certain time is proportional to the speed of the machine, so the resulting power loss is also proportional to it. The magnitude of the hysteresis loss is directly correlated with frequency (1).

$$P_{hiszt} = k_{hiszt} \cdot \Psi^2 \cdot f, \quad (1)$$

where  $k_{hiszt}$  coefficient highly depends on the geometry of the iron core.

An effective reduction of the hysteresis loss is possible by reducing the value of the coercive force, which is primarily a function of the material characteristic. In electromagnetic machines, therefore, soft magnetic materials are widely used due to their lower coercive force values and lower hysteresis losses.

A loss is caused also by the eddy current induced in the iron core due to variable flux. The magnitude of the loss caused by the resulting eddy current is inversely proportional to the resistance of the iron core [20].

The power loss of eddy current increases with the square of the frequency and flux (2)

$$P_{\ddot{r}rv} = k_{\ddot{r}rv} \cdot \Psi^2 \cdot f^2. \quad (2)$$

A proven method of reducing eddy current loss is to assemble the stator or core from electrically insulated thin sheets.

In the presence of a magnetic field, the boundaries of the domains in ferromagnetic materials move, which is called domain motion. Displacement consists of translational motion and, near the saturation limit, the turning of moments toward the outer space. As a result of this movement, the size of some domains increases, some decrease. In an alternating magnetic field, the change of these domains happens periodically, which results in a loss of energy and consequent heating. The power loss due to the movement of the domain wall is linearly proportional to the frequency.

In the case of high-speed electric motors and generators, the rate of iron loss due to high frequency starts to increase dramatically, as shown in Table 1. [5].

**Table 1.** Iron loss of soft magnetic materials NO10 and NO12. [5]

| Class | Thickness (mm) | Iron loss at 400 Hz (W/kg) | Iron loss at 2500 Hz (W/kg) |
|-------|----------------|----------------------------|-----------------------------|
| NO10  | 0.10           | 13.0                       | 135                         |
| NO12  | 0.12           | 13.5                       | 132                         |

The reason for the significant increase can be seen in Figure 5. The change in the shape of the BH curve due to the increase in frequency can be significant, which is due to the fact that the change in the magnetic orientation of the domains cannot follow the rate of magnetic field change. The coercive force of the material increases significantly [5].

Despite the efforts of soft magnetic plate manufacturers, the high-frequency limit in usability of crystalline magnetic materials has reached its limit.

The need to increase efficiency e.g. in the case of electric motors, it is unquestionable due to the increasingly stringent regulations.

In the case of electromagnetic machines, one of the promising possibilities for increasing the degree of efficiency is the use of iron-based amorphous alloys. In these materials, a significant decrease in coercive force is observed due to the change in the inverse relationship between grain size and coercive force. The coercive force showing a decreasing trend as a function of particle size, resulting in a significant reduction in iron loss.

In the case of electromagnetic machines, the so-called loss power density is obtained as the quotient of the electrical loss power and the motor volume. For machines with air cooling, this limit is approximately 300 W/litre.

Figure 6. illustrates the power density of a HITPERM nanocrystalline alloy (blue dotted line) as a function of frequency compared to similar properties of other widely used crystalline materials. It can be seen that using HITPERM nanocrystalline materials, the same loss occurs at a frequency of 1 order of magnitude.

In addition to the lower coercive strength of HITPERM alloys, another advantage is the manufacturability of 0.005-0.050 mm thick sheets, which causes a further reduction in iron loss through a reduction of eddy current [20].

The use of FINEMET alloy is also promising in these applications, with the help of several heat treatment methods to further improve the properties [23].

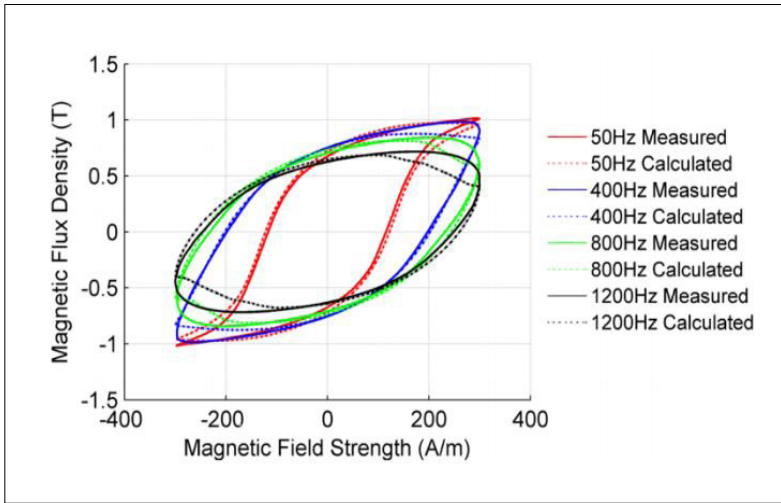


**Figure 5.** Distortion of B-H curve due to high frequency changing of magnetic field. [22]

The use of nanocrystalline materials may be limited by the fact that the improvement of magnetic properties is accompanied by a deterioration of the mechanical properties, which means that the material becomes brittle. This places a special limit on the mechanical manufacturability of such thin sheets, and the use of new manufacturing processes becomes necessary, e.g. the use of laser cutting technology, which has being widely researched [5] [24].

**4. Summary and conclusions**

Due to the characteristics of supercritical carbon dioxide (sCO<sub>2</sub>) power cycles, it is necessary to use a small but high speed turbine, which makes

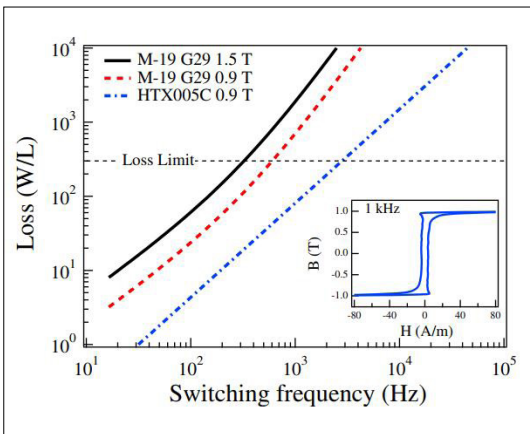


**Figure 6.** Example of iron loss dependency to frequency [20]

it necessary to solve complex technical problems. The speed of the high-speed shaft of the turbine must be reduced to convert the mechanical energy into electrical energy with a conventional synchronous generator. In addition to power plant capacities (100 MW), the use of such speed deceleration gears is a rather inefficient, and involves high investment and high operating cost. In order to improve the efficiency of such applications, it is necessary to introduce other new technologies in order to eliminate the use of speed deceleration gearbox.

The efficiency of electromagnetic machines decreases with increasing speed. This can be explained, among other things, by the increase in iron loss, the coercive force in soft magnetic materials increases with the frequency, and the B-H curve becomes wider. Depending on the material, this causes significant loss in efficiency above a certain frequency, with a significant heating of the electromagnetic machine. Reducing the iron loss at high speed (frequency) allows the reducing gearbox between the turbine and the generator to be omitted in the sCO<sub>2</sub> application, so the turbine can drive the generator directly. With this direct drive, the highest energy conversion efficiency can be achieved, so energy efficiency can be increased and the environmental load can be reduced.

Among the soft magnetic materials, the amorphous metallic glasses have the lowest coercive force in high-frequency magnetic fields, so their application has yielded great results in reducing the

iron losses of high-speed E-motors and generators. The use of such amorphous materials in the construction of an electromagnetic machine requires the development of new types of manufacturing processes and material testing technologies due to the characteristics of the raw material. Summarizing the results of several domestic and international researches, it can be seen that it is possible to build a high-speed electrical machine with increased efficiency using amorphous materials.

### Acknowledgments

The research presented in this paper has been carried out within the framework of the “New Széchenyi Plan” as part of the EFOP-3.6.2-16-2017-00016 project. For the results presented in this article, EFOP-3.6.1-16-2016-00003 “Long-term strengthening of R&D&I processes at the University of Dunaújváros”. research funded by the project contributed. The research was supported by the European Union and co-financed by the European Social Fund.

### References

- [1] R. G. Newell, D. Raimi, G. Aldana: *Global Energy Outlook 2019: The Next Generation of Energy*. Report 19-06/2019. <http://www.econ2.jhu.edu/courses/101/GlobalEnergyOutlook2019.pdf>, 2020.10.05
- [2] A. Zandian, M. Ashjaee: *The thermal efficiency improvement of a steam Rankine cycle by innovative design of a hybrid cooling tower and a solar chimney concept*. *Renewable Energy*, 51. (2013) 465–473. <https://doi.org/10.1016/j.renene.2012.09.051>
- [3] C. Geng, Y. Shao, W. Zhong, X. Liu: *Thermodynamic Analysis of Supercritical CO<sub>2</sub> Power Cycle with Fluidized Bed Coal Combustion*. *Coal and Biomass Combustion*, 2018. Article ID 6963292, <https://doi.org/10.1155/2018/6963292>
- [4] K. Meah, S. Ula: *Comparative Evaluation of HVDC and HVAC Transmission Systems*. IEEE Power Engineering Society General Meeting, 2007. 1–5, <https://doi.org/10.1109/PES.2007.385993>
- [5] Szabó A.: *Gondolatok egy ígéretes lágymágneses anyagról*. Magyar Acél, 2017. ősz, 41–43. <http://www.mvae.hu/kiadvanyok/mvae-szeptember-web.pdf>
- [6] T. Conboy, S. Wright: *Experimental Investigation of the S-CO<sub>2</sub> Condensing Cycle*. Supercritical CO<sub>2</sub> Power Cycle Symposium, May 24-25, 2011, Boulder, CO, SAND2011-2690C
- [7] Yoonhan Ahn, et. al.: *Review of supercritical CO<sub>2</sub> power cycle technology and current status of research and development*. *Nuclear Engineering and Technology*, 47/6. (2015) 647–661. <https://doi.org/10.1016/j.net.2015.06.009>
- [8] S. Hameer, J. L. van Niekerk: *A review of large scale electrical energy storage*. *International Journal of Energy Research*, 39/9. (2015) 1179–1195. <https://doi.org/10.1002/er.3294>
- [9] Y. Sun et al.: *Coupling supercritical carbon dioxide Brayton cycle with spray-assisted dry cooling technology for concentrated solar power*. *Applied Energy*, 251. (2019) <https://doi.org/10.1016/j.apenergy.2019.113328>
- [10] M. Mohagheghi, J. Kapat: *Thermodynamic optimization of recuperated sCO<sub>2</sub> Brayton cycles for waste-heat recovery applications*. The 4<sup>th</sup> International Symposium – Supercritical CO<sub>2</sub> Power Cycles 2014, Pittsburgh, USA.
- [11] K. Brun, P. Friedman, R. Dennis: *Fundamentals and applications of supercritical carbon dioxide (sCO<sub>2</sub>) based power cycles*. Woodhead Publishing, 2017.
- [12] V. Dostal, P. Hejzlar, M.J. Driscoll: *The Supercritical Carbon Dioxide Power Cycle: Comparison to Other Advanced Power Cycles*. *Nuclear Technology*, 154/3. (2006) 283–301. <https://doi.org/10.13182/NT06-A3734>
- [13] Ideen Sadrehaghighi: *Multiphase Flow*. CFD Open Series, Report number: 2.11, aug. 2020. [https://www.researchgate.net/profile/Ideen-Sadrehaghighi/publication/320107451\\_Multiphase\\_Flow/links/5f4741df458515a88b706909/Multiphase-Flow.pdf](https://www.researchgate.net/profile/Ideen-Sadrehaghighi/publication/320107451_Multiphase_Flow/links/5f4741df458515a88b706909/Multiphase-Flow.pdf)
- [14] S. A. Wright et. al.: *Modeling and Experimental Results for Condensing Supercritical CO<sub>2</sub> Power Cycles*. Sandia Report. SAND2010-8840, 2011.
- [15] S. A. Wright, et. al.: *Operation and Analysis of a Supercritical CO<sub>2</sub> Brayton Cycle*. Sandia Report. SAND2010-0171, 2010.
- [16] Q. Zhu: *Innovative power generation systems using supercritical CO<sub>2</sub> cycles*. *Clean Energy*, 1/1. (2017) 68–79. <https://doi.org/10.1093/ce/zkx003>
- [17] Z. M. Fairuza, I. Jahn: *The influence of real gas effects on the performance of supercritical CO<sub>2</sub> dry gas seals*. *Tribology International*, 102. (2016) 333–347.
- [18] S. A. Wright, M. Anderson: *Supercritical CO<sub>2</sub> cycle for advanced NPPs*. Workshop on New Cross-cutting Technologies for Nuclear Power Plants, 2017. [https://energy.mit.edu/wp-content/uploads/2017/02/2-5-U-Wisc-SCT-MIT\\_slides\\_V4b-min.pdf](https://energy.mit.edu/wp-content/uploads/2017/02/2-5-U-Wisc-SCT-MIT_slides_V4b-min.pdf)
- [19] G. Stefan et. al.: *Evaluation of sCO<sub>2</sub> power cycles for direct and waste heat applications*. 2<sup>nd</sup> European sCO<sub>2</sub> Conference 2018, <https://doi.org/10.17185/duerpublico/46074>
- [20] J. M. Silveyra et. al.: *High speed electric motors based on high performance novel soft magnets*. *Journal of Applied Physics* 115/17. 17A319 (2014), <https://doi.org/10.1063/1.4864247>
- [21] S. Duniyam, F. Sabri, K. Hooman: *A novel hybrid geo-solar thermal design for power generation in Australia*. *Journal of the Taiwan Institute of Chemical Engineers*, 27 March 2021. <https://doi.org/10.1016/j.jtice.2021.03.023>
- [22] Du Ruoyang, Robertson P.: *Dynamic Jiles-Atherton Model for Determining the Magnetic Power Loss at*

- High Frequency in Permanent Magnet Machines*. IEEE Transactions on Magnetics, 51/6. (2015) <https://doi.org/10.1109/TMAG.2014.2382594>
- [23] Szabó A., Sánta R., Lovas A., Novák L.: *A FINE-MET-ötvözet tulajdonságváltozásának vizsgálata hagyományos, impulzusos és mechanikai feszültség alatt végzett hőkezelést követően*. Acta Materialia Transylvanica, 3/1. (2020) 43–49., <https://doi.org/10.33923/amt-2020-01-08>
- [24] A. Szabó, A. Nagy, G. Kozsely: *Laser cutting technology development for Fe based metallic glass*. 2019 IEEE 17<sup>th</sup> International Symposium on Intelligent Systems and Informatics (SISY). <https://doi.org/10.1109/SISY47553.2019.9111604>
- [25] Berta I., Kádár I., Szabó L.: *Váltakozó áramú rendszerek*. 2012. [https://regi.tankonyvtar.hu/hu/tartalom/tamop425/0048\\_VIVEM111/index.html](https://regi.tankonyvtar.hu/hu/tartalom/tamop425/0048_VIVEM111/index.html) (2020. 11. 10.)
- [26] M. Persichilli et al.: *Supercritical CO<sub>2</sub> Power Cycle Developments and Commercialization: Why sCO<sub>2</sub> can Displace Steam*. Presented at Power-Gen India & Central Asia 2012, New Delhi, India.

# The Effect of Chemical Composition and Production Technology on the Mechanical Properties of EN AW-8006 Alloy

Judit PÁZMÁN,<sup>1</sup> Jánosné FEHÉR,<sup>2</sup> Viktor GONDA,<sup>3</sup> Balázs VERŐ<sup>4</sup>

<sup>1</sup> University of Dunaujvaros, Institute of Technology, Department of Materials Science, Dunaujváros, Hungary, pazman@uniduna.hu

<sup>2</sup> University of Dunaujvaros, Institute of Technology, Department of Materials Science, Dunaujváros, Hungary, feherjanosne@uniduna.hu

<sup>3</sup> Óbuda University, Bánki Faculty of Mechanical and Safety Engineering, Institute of Materials and Manufacturing, Budapest, Hungary, gonda.viktor@bgk.uni-obuda.hu

<sup>4</sup> University of Dunaujvaros, Institute of Technology, Department of Materials Science, Dunaujváros, Hungary, verob@uniduna.hu

## Abstract

Aluminum alloys EN AW-8006 with three different Fe:Mn ratios were studied. In the experiments, the temperature of the intermediate soft-annealing between the cold rolling processes and the final soft-annealing at the end of the production technology were varied. The processed samples were subjected to tensile testing and hardness measurements. The effect of chemical composition, based on the test results, showed that for samples without intermediate softening, only the increase of iron content has a significant effect on the yield stress, and the change of iron content refined the final grain structure compared to the reference material.

**Keywords:** EN AW-8006, chemical composition, intermediate annealing, tensile test.

## 1. Introduction

The 8xxx category of aluminum alloys includes special alloys of aluminum. The most important types are EN AW-8006 (AlFeMn), Al8011 (AlFeSi), and Al8018 (Al-FeSiCu) [1]. By evaluating the conditions of the Hume-Rothery rule for unlimited solubility, it is clear that these alloying elements are not – or only to a limited extent – soluble in solid aluminum. The limited solubility, in turn, induces the formation of compound phases, even as a first step in crystallization. Iron and manganese as transition elements promote the formation of intermetallic phases to which diamond latticed silicon contributes too. Thus, in the dendritic spaces in the 8xxx alloys, there are intermetallic phases, the amount and shape of which also strongly determine the manufacturing technology and end use of the selected product itself. The present work deals with the EN AW-8006 alloy in such a way that, on the one hand, chemical compositions within the standard are changed

and, on the other hand, the production technology is optimised. The difference between the chemical composition modifications is the ratio of iron and manganese in the two main alloying elements, which determine the type of Al-Fe-Mn compounds in the interdental spaces and thus their morphology. Considering the two-component phases at the aluminum-rich corner of the Al-Fe-Mn ternary system; FeAl<sub>3</sub>, MnAl<sub>6</sub> and AlMn<sub>4</sub> phases are formed during crystallization. However, manganese can replace the site in MnAl<sub>6</sub> with iron and form a tricomponent compound with FeMnAl<sub>12</sub> contents of 13% Fe and 14% Mn [2-3]. This is the so-called (Fe, Mn) Al<sub>6</sub> phase. The shape, size and number of phases during crystallization are determined by the rate of cooling; in terms of chemical composition, it is also influenced by the presence of additional and micro alloying elements, the total amount of Fe, Mn and Si, and the grain refining process [4]. Among the alloying elements, the incorporation of copper into the lattice of the intermetallic phase is able to stabilize the

lamellar structure characteristic of Al-Fe phases, as well as high heat treatment at high temperatures, e.g. during homogenization, it prevents the phases from redissolving and spheroidizing, thus complicating the processing, i.e. hot and cold rolling (Figure 1.) [5].

Large lamellar phases cause the formation of so-called “pencil phases” during the plastic forming process, the grouping of which easily lead to rupture of the final product, such as the rupture of a 200 µm thick foil (Figures 2–3.) [6].

Remaining within the standard range of composition, chemical composition was slightly changed to create the most favourable phase structure as possible. The aim is to identify the phases that reduce the volume fraction of the pencil phases in the formed alloy.

Figure 4. shows the phase stages of the Fe:Mn ratio, and the chemical composition variants were developed accordingly. On the selected chemical alloys, homogenization, hot rolling, cold rolling, and between the cold rolls were achieved with intermediate soft-annealing in one half of

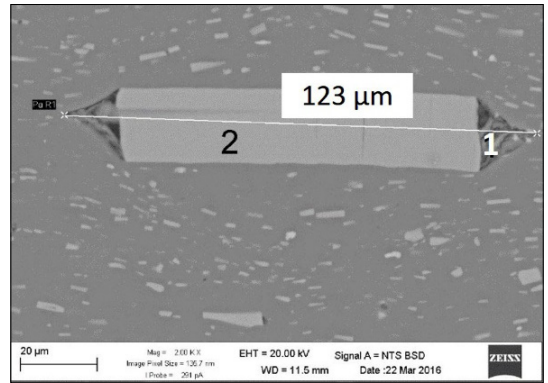


Figure 2. Large „pencil” phase in EN AW-8006 alloy  
1 – hole with the resin;  
2 – 73,8w% Al, 19,5w% Fe, 6,7w%Mn.

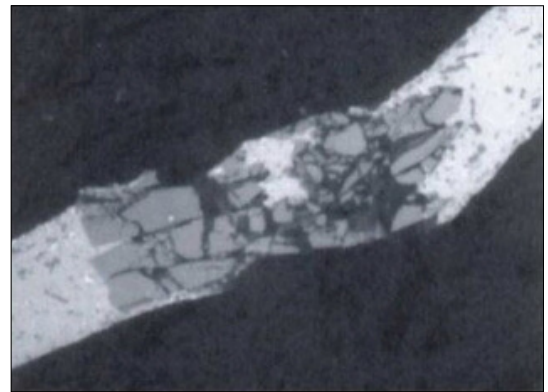


Figure 3. The rupture of foil due to the agglomeration of „pencil” phase.

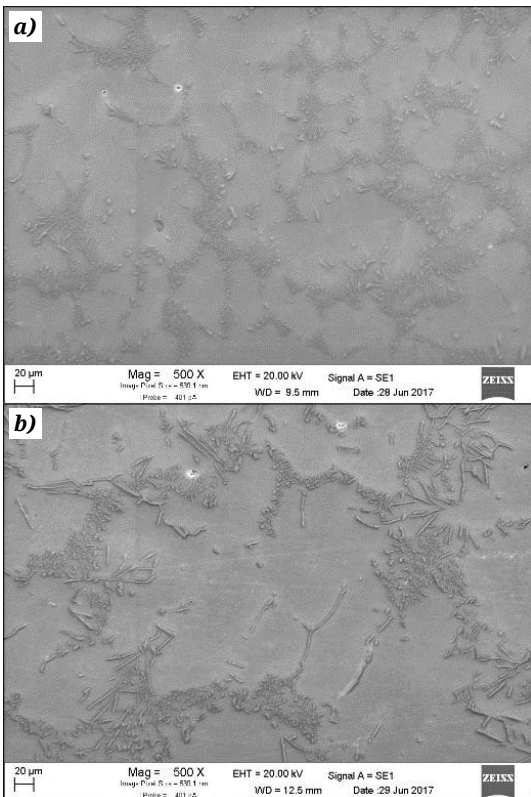


Figure 1. A the phase structure of EN AW-8006 alloy  
a) EN AW-8006 alloy without Cu;  
b) EN AW-8006 alloy with Cu.

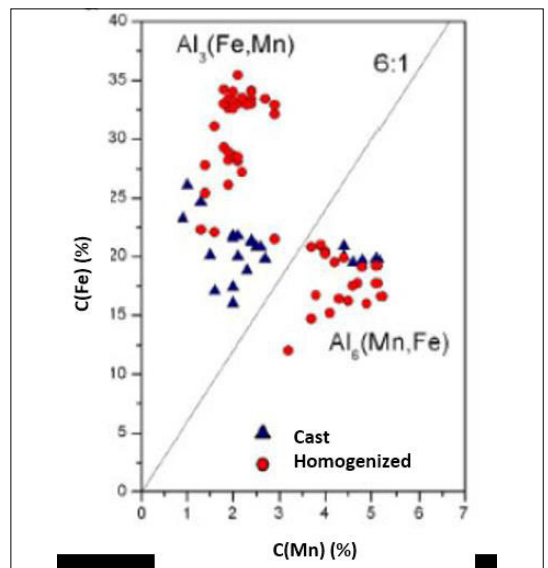


Figure 4. The compound forming role of Fe:Mn ratio in EN AW-8006 alloy.

the samples and no intermediate soft-annealing in the other half. The last step in the technological sequence of operations was soft-annealing at the final thickness.

## 2. Experimental

To select the chemical composition of the alloy, the Standard starting chemical composition of EN AW-8006 alloy was used, according to which 1.2–2% Fe, max. 0.4% Si, max. 0.3%Cu, 0.3–1% Mn, max. 0.1% Mg, max. 0.1%Zn, others Al.

Based on findings in the literature and our preliminary homogenization experiments, the following basic concept was developed to determine the chemical composition variants:

1. The copper-free EN AW-8006 alloy is considered as the reference material, hereinafter referred to as EN AW-8006\_R as the reference material.
2. The amount of contaminants is minimized, so that a purer alloy is produced in order to reduce the amount of secondary phases formed from the contaminants.
3. In the case of the composition variants, the Fe/Mn ratio is varied, even without modifying the amount of Mn, because increasing this alloying element induces foundry problems, e.g. slurry formation. So the amount of iron was increased or decreased **Table 1.** shows the alloys variants compositions.

Thus, the ratio of the two elements in the first case, where the notation is R, is the Fe/Mn ratio: 3.15. In the second case, where the notation is csFe - reduced iron content: Fe/Mn ratio = 3. In the third case, where the Fe/Mn ratio = 3.875, denoted by nFe - increased iron content. Table 1 shows the amounts of alloying elements.

In addition to the modification of the chemical composition, the production process of the alloys was also changed in such a way that, after the hot rolling, cold rolling was carried out with and without intermediate soft-annealing. In this way, the effect of intermediate soft-annealing was

**Table 1.** Chemical composition of EN AW-8006 alloy variants

| Sample name     | Fe (%) | Mn (%) |
|-----------------|--------|--------|
| EN AW-8006_R    | 1.05   | 0.3    |
|                 | 1.15   | 0.4    |
| EN AW-8006_csFe | 1.15   | 0.3    |
|                 | 1.25   | 0.4    |
| EN AW-8006_nFe  | 1.3    | 0.3    |
|                 | 1.5    | 0.4    |

studied on the particle structure and mechanical properties of the final product. The intermediate soft-annealing was accomplished with different temperature and time parameters on the samples of the selected composition, so that the best set of soft-annealing parameters for the given composition could be given. Also, the optimum for this technological step by changing the temperature and time parameters of the final thickness softening was investigated.

From the alloys of different chemical compositions, 50 mm thick small blocks were cast, homogenized at 605°C, then hot-rolled at 500°C to a thickness of 5.2 mm, and then some of the samples were cold-rolled without intermediate soft-annealing until 0.5 mm final thickness. The other half of the samples were cold-rolled to a thickness of 1 mm after hot forming, at which point they received the intermediate soft-annealing, and then the cold forming was completed at 0.5 mm. The intermediate soft-annealing temperatures at 1 mm were 320°C, 340°C, 360°C and 380°C. Final soft-annealing temperature at 0.5 mm was 220°C, 260°C, 300°C, 340°C and 380°C. The soft-annealing time was 2 h at each temperature. The samples thus prepared were subjected to tensile testing, as well as microhardness measurements and microstructural analysis.

**Figure 5.** shows the effect of intermediate softening on the hardness values of the alloy compositions, based on which, it is clear that the alloy already shows partial softening at 320°C and the hardness changes only slightly with increasing temperature. There are no substantive differences between the chemical composition variations. The complete softening occurs at 340°C.

The intermediate softened piece was formed to final thickness and then final soft-annealed.

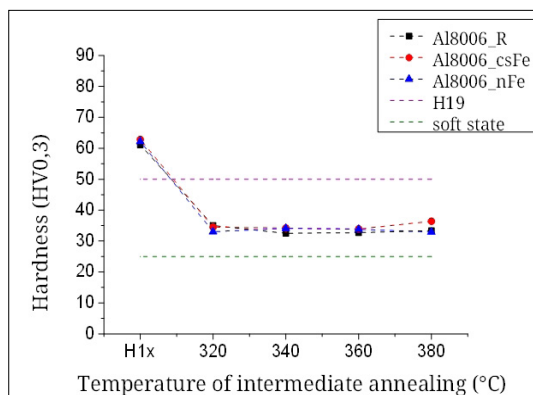


**Figure 5.** The effect of intermediate annealing on the hardness of deformed samples.

It can be clearly seen from the diagrams of Figure **Figure 6**. that the alloy partially softens at 260°C, regardless of the chemical composition variants, and the hardness changes only slightly with increasing temperature. Complete softening occurs at 300°C.

For samples without intermediate softening, the diagrams in **Figure 7**. show the hardness values after final softening.

According to the diagrams of Figure **Figure 7** , if the intermediate softening is removed from the technological step sequence, the alloy will soften at 300°C as in the case of the intermediate softened samples, but the degree of partial softening – based on the hardness measurement data – is significantly lower than for intermediate softened samples. No substantial difference can be detected between the chemical composition variants.

Reviewing the results of the tensile test, the samples without intermediate softening produce higher values at the yield strength values, which

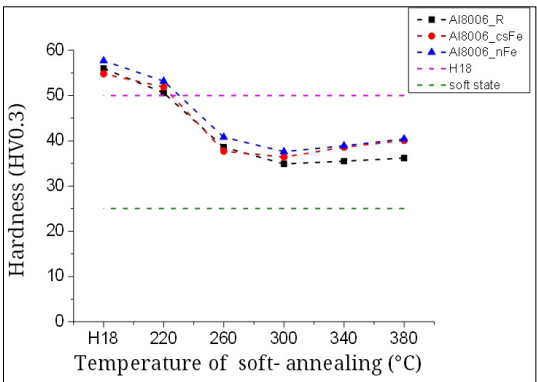


**Figure 6.** The effect of final soft-annealing on the hardness of intermediate annealed samples.

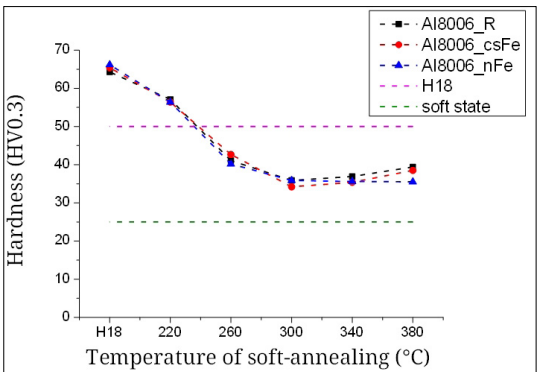


**Figure 7.** The effect of final soft-annealing on the hardness of deformed samples.

results from the formed state. Considering the chemical composition variants, the alloy with increased iron content shows a higher value, while the other two compositions are nearly identical. These differences in tensile strength and elongation at break are not observed, nor is the effect of softening or differences in chemical composition. (**Figure 8.**) The dashed lines in the diagram (**Figure 8.**) show the values of the standard required

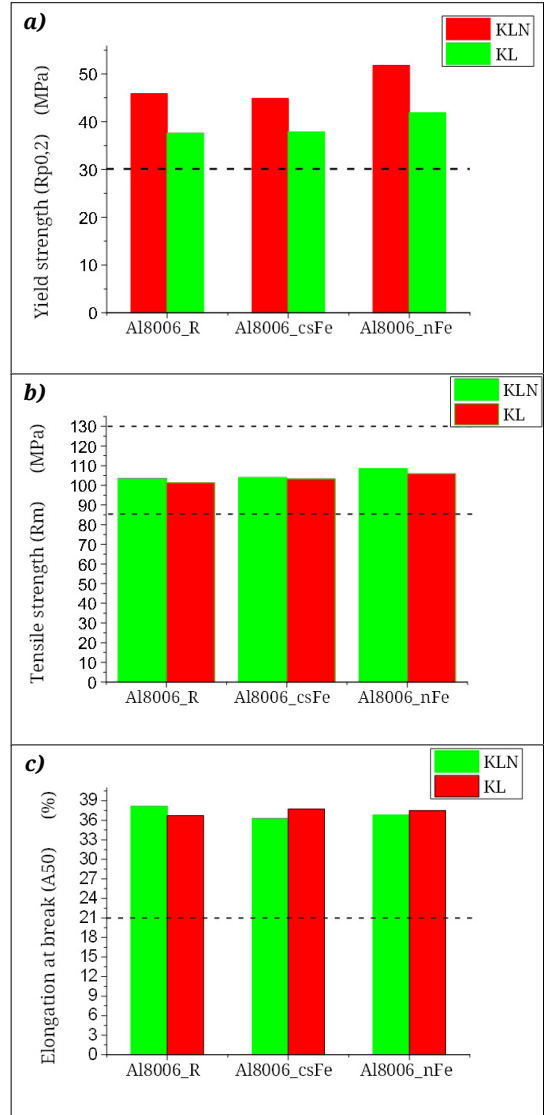


**Figure 8.** The effect of the chemical composition and intermediate soft-annealing on the mechanical properties  
a) Yield strength;  
b) Tensile strength;  
c) Elongation at break.

mechanical properties for the soft state of a given alloy, on the basis of which all three chemical composition variants reach or even exceed the desired values

In addition to the mechanical tests, a microstructural analysis was also performed. Metallographic images show the microstructure of the samples without intermediate soft-annealing (Figure 9.) and of the intermediate soft-annealed (Figure 10.), already rolled to final thickness as a function of the chemical composition. Analysing the effect of intermediate softening for each composition, the grain structure – according to ASTM E112-96 standards – is significantly larger in the

case of sample R ( $G = 6.5-7$ ) but this significant difference is no longer observed in the case of alloys with reduced ( $G = 7.5-8$ ) and increased ( $G = 8-8.5$ ) iron content (Figure 9.). It should be noted that there is an increase in particle size here as well, but not to the same extent as for the reference material. Regarding the effect of the chemical composition, the difference is not noticeable in the samples without intermediate softening. A larger difference and a much finer microstructure can be observed in the intermediate softened samples, where changing the iron content, i.e. changing, increasing and decreasing the Fe/Mn ratio, causes a significant grain refinement,

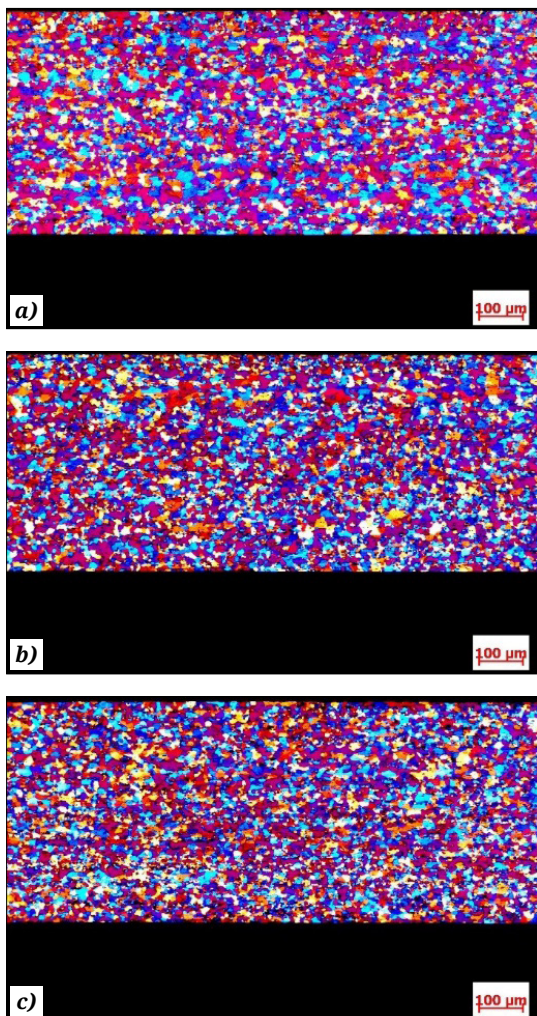
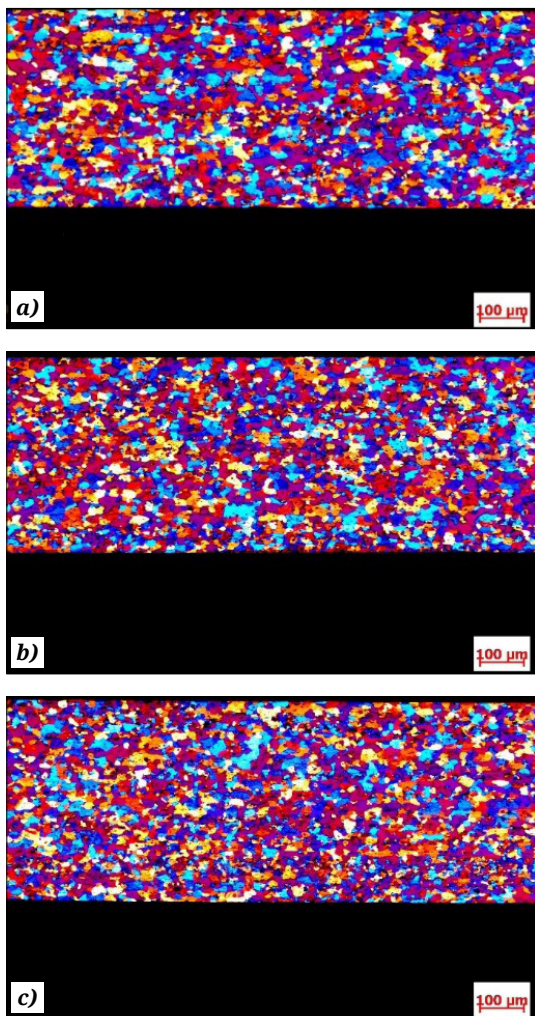


**Figure 9 .** Microstructure without the applying of soft-annealing  
 a) reference material;  
 b) alloy with decreased iron concentration;  
 c) alloy with increased iron concentration.



**10. ábra.** Microstructure with applying of soft-annealing  
 a) reference material;  
 b) alloy with decreased iron concentration;  
 c) alloy with increased iron concentration.

it means  $G=6-6.5$  for sample of R,  $G=6.5-7$  for sample of csFe, and  $G=7-7.5$  for sample of nFe, which can be attributed to the changed primary phase structure (Figure 10).

### 3. Conclusions

In this study, the EN AW-8006 alloy was tested by preparing three chemical composition variants and performing homogenization, hot rolling, cold rolling and intermediate softening in one half of the samples, and final softening in each case. Based on the results of tensile tests, hardness measurements and microstructure analysis performed on samples of different chemical composition and manufacturing technology, the following conclusions can be made:

1. Differences in chemical composition generate significant differences in yield strength values, with increased iron content yield yields above 50 MPa can be achieved without intermediate softening. No significant difference can be detected in either the tensile strength or the elongation at break by changing the chemical composition or by using intermediate softening.
2. The increased or decreased iron content, ie the change of the Fe:Mn ratio, has an effect on the particle structure of the intermediate softened and then softened samples, a finer structure with a smaller particle size can be created.

### Acknowledgement

The authors would like to thank GINOP-2.2.1-15-2016-00018 “Development of the technology of new, marketable rolled aluminum products, based on the latest results of technical materials science, the market-leading Hungarian industrial company, ARCONIC-Köfém Kft. + In cooperation with

the universities’, furthermore and EFOP-3.6.1-16-2016-00003 project “Long-term strengthening of R & D & I processes at the University of Dunaújváros” and EFOP-3.6.2-16-2017-00016 Dynamics and control of autonomous vehicles in synergy with the requirements of automated transport systems for the feasibility of experiments. The project was supported by the European Union and co-financed by the European Social Fund.

### References

- [1] Moldovan P., Popescu G., Miculescu F.: *Microscopic study regarding the microstructure evolution of the 8006 alloy in the plastic deformation process*. Journal of Materials Processing Technology, 153–154. (2004) 408–415. <https://doi.org/10.1016/j.jmatprotec.2004.04.345>
- [2] Englera O., Lapyteva G., Wang N.: *Impact of homogenization on microchemistry and recrystallization of the Al-Fe-Mn alloy AA 8006*. Materials Characterization, 79. (2013) 60–75. <https://doi.org/10.1016/j.matchar.2013.02.012>
- [3] Warmuzek M., Gazda A., Sieniawski J.: *Processes of the formation of the Fe(Mn)-bearing intermetallic phases in the Al-Fe-(Mn)-Si alloys*. Advances in Materials Science, 4/2(4). (2003). 81–91. [bwmeta1.element.baztech-article-BPG5-0015-0041](http://www.bwmeta1.element.baztech-article-BPG5-0015-0041).
- [4] Lentz M., Lapyteva G., Enger, O.: *Characterization of second-phase particles in two aluminium foil alloys*. Journal of Alloys and Compounds, 660. (2016) 276–288. <https://doi.org/10.1016/j.jallcom.2015.11.111>
- [5] Mundson D.: *A clarification of the phases occurring in aluminium-rich aluminium-iron-silicon alloys, with particular reference the ternary phase  $\alpha$ -AlFeSi*. Journal of the Institute of Metals, 95. (1967) 217–219.
- [6] Keles O., Dundar M.: *Aluminum foil: Its typical quality problems and their causes*. Journal of Materials Processing Technology, 186. (2007) 125–137. <https://doi.org/10.1016/j.jmatprotec.2006.12.027>

# The formation and stability of bulk amorphous and high entropy alloys

Attila SZABÓ,<sup>1</sup> Krisztián BÁN,<sup>2</sup> József HLINKA,<sup>3</sup> Judit PÁSZTOR,<sup>4</sup> Antal LOVAS<sup>5</sup>

<sup>1</sup> University of Dunaujvaros, Department of Mechanical Engineering, Dunaujvaros, Hungary, [szaboattila@uniduna.hu](mailto:szaboattila@uniduna.hu)

<sup>2</sup> Budapest University of Technology and Economics, Faculty of Transportation Engineering, Department of Automotive technologies, Budapest, Hungary, [ban.krisztian@kjk.bme.hu](mailto:ban.krisztian@kjk.bme.hu)

<sup>3</sup> Budapest University of Technology and Economics, Faculty of Transportation Engineering, Department of Automotive technologies, Budapest, Hungary, [hlinka.jozsef@kjk.bme.hu](mailto:hlinka.jozsef@kjk.bme.hu)

<sup>4</sup> Sapientia Hungarian University of Transylvania Faculty of Technical and Human Sciences, Târgu-Mureş, Romania, [pjudit@ms.sapientia.ro](mailto:pjudit@ms.sapientia.ro)

<sup>5</sup> Budapest University of Technology and Economics, Faculty of Transportation Engineering, Department of Automotive technologies, Budapest, Hungary, [antal.lovass@gjt.bme.hu](mailto:antal.lovass@gjt.bme.hu)

## Abstract

Two kinds of phase stabilization mechanism are discussed and compared: the first is characteristic of the formation of bulk amorphous alloys, in which the high supercooling ability of multicomponent liquids is responsible for the glassy phase stabilization. Here the hindered nucleation of crystalline phases is the center phenomenon. The origin of this hindering is the slowing atomic mobility in the supercooling melt. In contrast the melt supercooling is negligible during the high entropy alloy formation. It is believed that stability of the crystalline single fcc phase is the consequence of the characteristic of high configurational entropy at high temperatures. However, the significance of this entropy-dominated stabilization is overestimated in several references. It has been concluded that transition metal contraction (arising from the d electron participation in the overall bonding state) does also contribute to the high temperature stability of fcc single phase in the high entropy alloys.

**Keywords:** *bulk metallic glass, high entropy alloy.*

## 1. Introduction

During the past few decades of metal physics (1980 -2020) the non-equilibrium metallic systems have become the center of interest. Two important magnetic properties: the excellent high frequency magnetic permeability and, the high saturation induction [1] are successfully unified in the glassy alloys, resulting in the development of new types of amorphous alloy transformers and motors with reduced power loss, and several types of other inductive elements [2, 3]. Recently, scientific interest has turned towards two groups of materials: the bulk amorphous alloys (BMGs) and the high entropy alloys (HEAs), as these group of materials promise a breakthrough in the improvement of high temperature mechanical properties [4]. The bulk amorphous alloys with

high glass forming ability and high phase stability [4] exhibit some similarity to the high entropy alloys [5]: both groups of alloys consist of several chemical elements. The numerous components play a dominant role in the phase stabilization of these materials.

In this paper we point to the significance of the strength of individual chemical bonds in the retardation of atomic diffusivity towards the fully thermodynamic equilibrium structure.

## 2. Results and discussion

### 2.1. Similarity and difference in the formation mechanism of BMGs and HEAs

Both BMGs and HEAs are formed from a liquid state consisting of several chemical components.

The main difference between them is the degree of melt supercooling ability. The difference between the supercooling results in fundamentally different solidified structures, i.e., the supercooling is a central phenomenon from the point of view of solidified structure.

Bulk Metallic Glasses (BMG) is a class of multi-component metallic materials, at which crystallization is kinetically suppressed by a number of factors such as atomic diameter difference, high natural supercooling, negative heat of constituent elements mixing, etc. Material systems with high Glass-Forming Ability (GFA) are thermodynamically unstable, and then subsequent heating („turning on” of diffusion) may cause their crystallization.

On the other hand, High Entropy Alloys (HEA) exist in single-phase solid solution, the crystalline state characterized by high configurational entropy. They just have a strong thermodynamically dictated tendency to avoid formation of ordered solid solutions as well as inter-metallic compounds. The main term which is responsible for their stability is the entropy term, so their heating improves their stability.

The supercooling phenomena is illustrated in the **Figure 1** where the entropy change is depicted during the cooling of two liquid types. BMGs and HEAs basically differ from the point of view of their supercooling ability, hence also the temperature range of thermodynamic stability of the resulting solid phases also differ. When the single component liquid is cooled, at  $T_m$  (equilibrium melting point) the liquid starts to crystallize, and crystallization finishes at the same temperature, so a supercooled state does not appear prior to and during crystallization. In this case the total free enthalpy change is identical to the entropy change. Nevertheless, the liquid-crystalline transformation can also happen at significantly lower temperatures between  $T_m$  and  $T_K$  where  $T_K$  is the Kauzmann-temperature, which is the limit of supercooling. In this temperature range non-equilibrium solidification occurs, so the resulting structure is metastable.

It has also been pointed out that the supercooling ability of high entropy alloys in liquid is negligible.

Compared to the liquids of HEAs, the BMGs are able to deeply super-cool. The entropy of liquid within this range approaches the solid phase, and at  $T_K$  the entropy of the two phases will be identical (**Figure 1**).

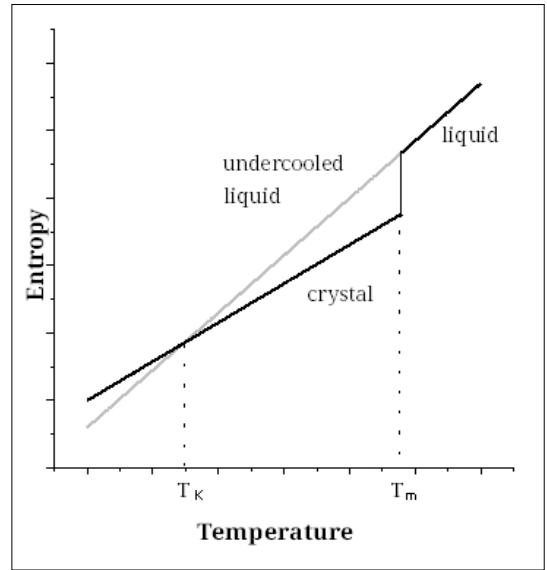


**Figure 1.** The temperature dependence of entropy in the liquid and crystalline phases: the meaning of Kauzmann temperature. [6]

The degree of supercooling-ability exhibits a great variety in liquids. This phenomenon can be described successfully by the temperature dependence of viscosity. The kinetic aspects in submicroscopic scale is represented by the change of atomic mobility during supercooling: The key concept is the time-scale of elementary atomic motions, which increases as the temperature of liquid decreases, being described by the Stokes-Einstein equation:

$$\frac{1}{\eta} = \lambda^2 \cdot \left( \frac{A}{l \cdot k \cdot T} \right) \quad (1)$$

It expresses phenomenological coupling between displacements in atomic level and viscosity, which can be derived from macroscopic measurements ( $A = \text{constant}$ ,  $k = \text{Boltzmann constant}$ ,  $T = \text{absolute temperature}$ ,  $\lambda$  and  $l = \text{molecular level distances}$ ,  $\eta = \text{viscosity}$ ).

The frequency of elementary step of atomic motion is the vicinity of melting point (around  $10^{-13}$  sec), prolonged residence time (preferential contacts) between hetero-atoms is not developed, so the components distribution is nearly random.

The characteristic of temperature dependence of viscosity  $\eta(T)$  is used for the description of dynamic phenomena during the process of super-cooling. Two basic type of T-dependence are known (i.e. two liquid types exist from this point of view (see **Figure 2**):

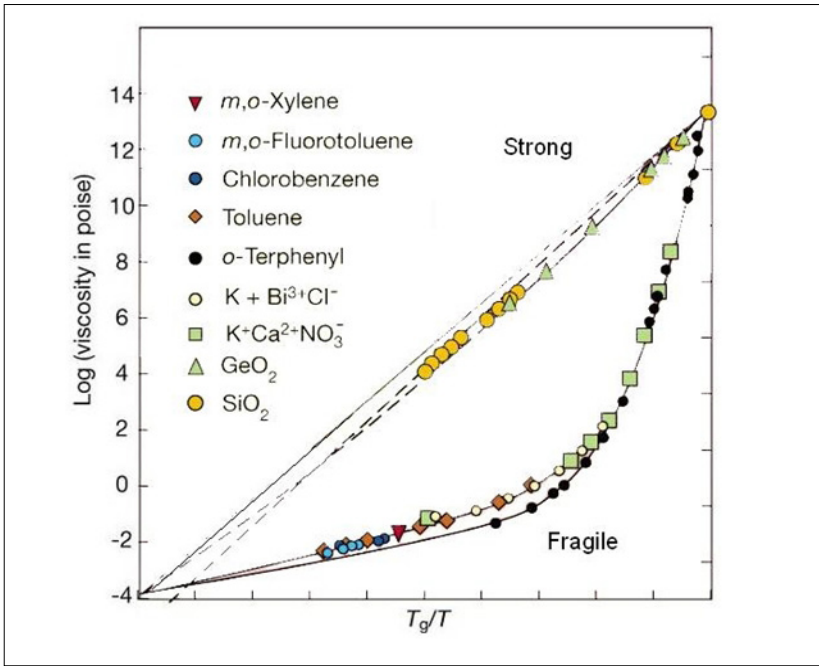


Figure 2. The comparison of  $\eta(T)$  for “strong and “fragile” glass forming liquids. [7]

– Arrhenius type:

$$\eta = A \cdot \exp[E/(T - T_0)] \text{ (strong liquid),} \quad (2)$$

with high GFAM,

– Vogel–Fulcher type:

$$\eta = \eta_0 \cdot \exp[B/(T - T_0)] \text{ (fragile liquid)} \quad (3)$$

with low GFAM.

It is believed that Arrhenius functionality with single activation energy represents single motion type in the elementary atomic scale over the whole range of supercooling (strong liquids with high glass forming ability) This high glass forming ability is pronounced in the formation of bulk amorphous alloys. (strong liquids in Figure 2).

In contrast, when two or more motion types co-exist and one of them is dominant within a given temperature range, such liquids are termed as „fragile” liquids. The glass forming ability is low in these liquid types. The temperature dependence of viscosity of these liquid types is also illustrated in Figure 2.

From Figures 2 and 3 is clear that the majority of „strong liquids” are multicomponent alloys, in which the strong covalent bond is dominant between the components (oxide glasses or, multicomponent alloys, with tendency towards inter-metallic compound formation in the solid state).

The majority of bulk metallic glasses are formed from Arrhenius-type melts. In Figure 3 different

liquids are collected exhibiting the transition between the strong and fragile liquids. All of the liquids are Arrhenius-type at low temperature range. Though, at higher temperatures (beyond  $T_g$ ) increasing deviation is observed, which strongly correlates with their glass forming ability. In Figure 4 the glass forming ability (the critical cooling rate,  $R_c$ ) and the resulting maximum of amorphous sample thickness are compared for

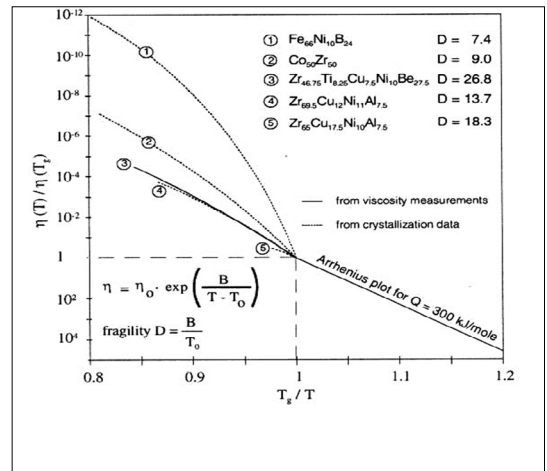
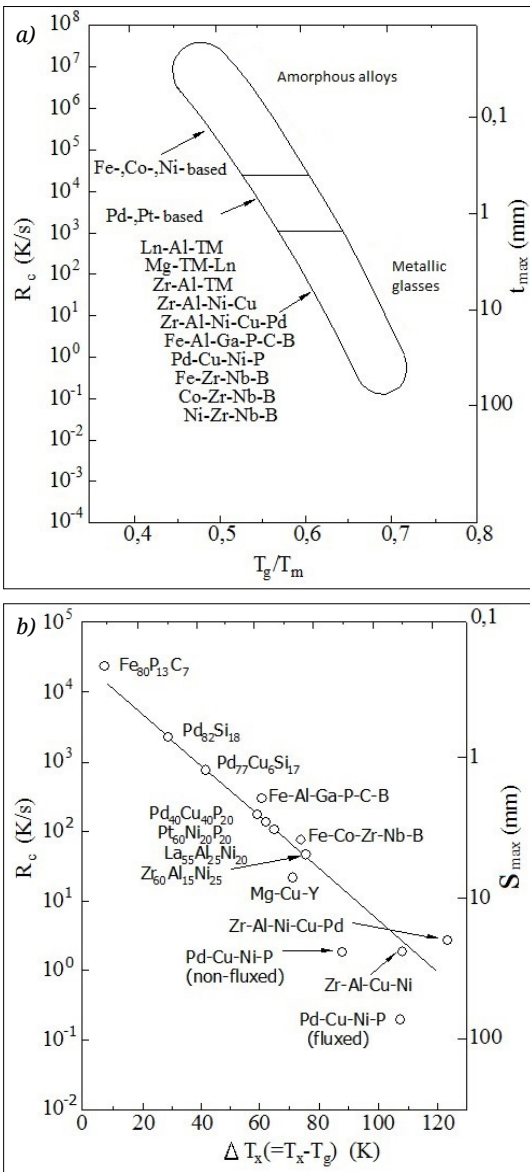


Figure 3. The viscosity temperature dependence for various glassforming ability liquids. [8]



**Figure 4.** Critical cooling rate and the resulting sample thickness ( $t_{max}$ ,  $S_{max}$ ) for several bulk glassy alloys versus the reduced ( $T_g/T_m$ ) (a) or  $\Delta T_x = T_x - T_g$  (b). [9]

various bulk amorphous alloys, and soft magnetic amorphous ribbons (produced by rapid solidification).

Compared to the bulk metallic glasses, the glass forming ability for traditional glassy soft magnetic alloys is low, therefore the necessary critical cooling rate is high ( $R_c$  (K/s) is  $\approx 105$ ) (see **Figure 4**).

## 2.2. Cluster formation in the glass-forming supercooled liquids

The interpretation of glass forming ability is in close connection with the cluster formation tendency in liquids [10, 11]. It is supposed that cluster formation in the supercooled melts represents kinetic hindering to the formation of crystalline nuclei. The clusters, which are associated groups of atoms, are considered as a molecule described with  $A_jB_j$  formula, but with a flexible structure in which the atomic distances between the unlike atoms are nearly constant, but the bonding angle is variable over a wide range.

According to the regular solution model conception [12], such liquid types, the entire mixing enthalpy of alloy formation ( $\Delta H$ , which can be directly determined, by calorimetry), consists of two terms:  $\Delta H^{reg}$  which is due to the preferential interaction between the hetero-atoms (components), and  $\Delta H_{A_jB_j}^{as}$  arising from the interaction between the atoms within the associates. This term represents the extra stabilization of the melt, compared to the regular solution model. This consideration leads to the formation of associates, according to (4).

$$\Delta H = \Delta H^{reg} + \Delta H_{A_jB_j}^{as} \quad (4)$$

In the first approximation, the structure of supercooled glass-forming melt can be described as a flexible assembly of associates and the remaining components are distributed randomly. The amorphous alloys can be regarded as a cluster assemble, in which the predominantly compound-like bonding state is cumulated [13]. The local bonding state hinders the diffusion leading to the formation of critical crystalline nuclei. The cluster level chemical short range order is developed at sufficient supercooling [14, 15]. As the cooling proceeds, approaching the  $\approx 2/3 T_m$  (jumping temperature, initial temperature of cluster formation) [9], the local composition (TM/M ratio) in compound-like associates is close to that in metastable inter-metallic compound and the local bonding strength between the hetero-atoms is higher. So the translation mobility is lower within the clusters, the time-scale of relaxation inside these covalent-like environments and in the remainder volume of liquid is different.

In conclusion, in the bulk amorphous alloys, which exhibit significant kinetic and thermal stability, the extended clusterization is responsible for the stabilization of amorphous state, due to the local diffusion break down of atoms, hin-

dering the critical nuclei formation of crystalline phases.

### 2.3. The formation mechanism and stability of high entropy alloys (HEA)

The study of HEA began in 2004. The reason for scientific interest is their high mechanical stability in high temperature ranges coupled with excellent corrosion resistivity. HEAs are also formed from liquid, but their formation does not require a special processing technique. Their denomination originates from the numerous components: the alloys consist of at least five “principal elements” which should have a concentration between 5–35 at%. Besides the principal elements HEA can also contain “minor elements” each below 5 at%. It is believed that high stability originates from the high mixing entropy at high temperatures:

$$S_{mix} = R \sum x_i \ln x_i \quad (5)$$

where  $x_i$  is the mole fraction of its component.

In contrast to the bulk amorphous alloys, the HEA are stabilized by configuration entropy at high temperatures. According to  $G = H - TS$ , (where  $G$  is the Gibbs free energy,  $H$  is enthalpy,  $T$  is temperature,  $S$  is entropy) the competition between enthalpy and entropy  $S$  determines the phase relation. Hence  $S$  can be a stabilizing factor, provided the temperature is sufficiently high. For example, in Co-Cr-Fe-Mn-Ni alloys (which is the best known composition) Ni, Fe, and Co exert a stabilizing effect to the fcc structure, while the opposite structure (bcc) is exerted by Cr and Mn.

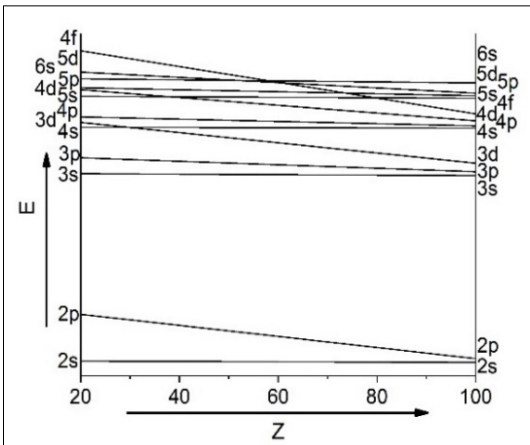


**Figure 5.** The energy level (ionization energy) of s, p and d electrons versus the position in the periodic table. [18]

The mechanism of the resulting preferred high temperature phase stabilization governed by the high entropy is not fully verified yet [16].

Therefore, further activity, directed at a deeper understanding of phase relation, mainly the conditions of single fcc-phase stabilization, is on-going. Recently, some research work has turned to the application of basic metallurgical principles defined earlier by Hume-Rothery [17]. It is surprising, that no correlation is found between the formation enthalpy and the temperature range of the fcc phase stability.

When compared with the ionization energy in the elements of periodic system, (including the s, p, and d electrons) it was found, that ionization energy for the d-electrons is the highest (Figure 5). This means that the bonding strength of d-electrons in the electron band is the highest. Therefore, attractive force between the core and electrons increases, resulting a net contraction of atomic radii.

As a consequence, specially compact, high density structures are developed in the HEAs, when the majority of components are transition metals. In this case, the participation of d-electrons is dominant in the valence band. One can suppose therefore that the well-known principle of transition metal contraction can also participate in the development of dense, random (fcc) structure, when the crystallization from liquid has started. As Figure 6 shows, the atomic radii gradually decrease with the increasing number of 3d, 4d, and 5d-electrons in the valence band. We can suppose therefore that simultaneous participation of Fe,

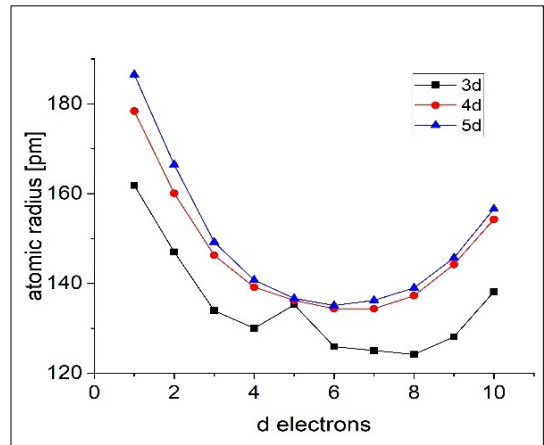


**Figure 6.** The change of atomic radius versus the increasing number of d-electrons in the valence band in the transition elements. [19]

Co, Ni principal elements enhance the development of the densest (fcc) structure, therefore, no significant supercooling is required for the critical nuclei formation of fcc solid phases i.e., the stabilization of single phase in wide temperature range.

In spite of the dense structure (which is a disordered solid solution) characteristic of the transition metals, the chemical interaction between the neighbouring TM atoms is not excluded. This interaction does not necessarily result in the formation of inter-metallic compound. This can also manifest as a net local charge shift between various neighbouring atoms, as proposed by Miedema [20], according to (6):

$$\Delta Z_a = 1.2 \cdot (1 - c_a) \cdot \Delta\Phi^* \quad (6)$$

$\Delta Z_a$  charge shift happens between the neighbouring atoms which is determined by the electro-negativity difference between the neighbouring atoms,  $\Delta\Phi$  is the difference (work function) ionization potential, which express the electro-negativity difference between two metal components in solid solution,  $c_a$  is the concentration of the atom  $a$ .

### 3. Conclusions

Two alloy systems, the BMGs and the single phase HEAs are compared from the point of view of their formation mechanism and their phase stability.

Both alloy systems are formed from liquids, containing more than five components.

Though both alloy systems are multicomponent, the spectra of components exhibit significant differences in their chemical properties: while the BMGs consist of various type of metal as well as metalloids, the main components of HEAs are predominantly transition metals.

While the BMGs are formed from deeply under-cooled liquids, the HEAs solidify in single phase crystalline solid solutions without melt supercooling. This single fcc phase disorder solid solutions fulfilled the high entropy requirement.

While the glassy state in BMGs is stabilized by the extended cluster formation, induced by the strong bonding between the metallic and metalloid components, the stability of HEA originates rather from the strong bonding character of d-electrons due to the dominant participation of d-electrons in the band structure, and resulting dense atomic distribution.

The stability in both systems arises from the local bonding stability between the components

(localized covalent-like bonding within the individual clusters). In the case of HEA the strong d-electron-bonding between the atoms of principal elements, results in a dense packing structure.

### Acknowledgements

The research presented in this paper was carried out as part of the EFOP-3.6.2-16-2017-00016 project in the framework of the New Széchenyi Plan. The completion of this project is funded by the European Union and co-financed by the European Social Fund.

The research presented in this paper was carried out as part of the EFOP-3.6.1-16-2016-0003 project in the framework of the New Széchenyi Plan. The completion of this project is funded by the European Union and co-financed by the European Social Fund.

### References

- [1] Makino A., Inoue A., Masumoto T.: *Nanocrystalline soft magnetic Fe-M-B (M=Zr, Hf, Nb) alloys produced by crystallization of amorphous phase (overview)*. Materials Transactions, JIM, 36/7. (1995) 924–938.  
<https://doi.org/10.2320/matertrans1989.36.924>
- [2] Nagy A.: *Electric aircraft-present and future*. Production Engineering Archives, 23. (2019) 36–40.
- [3] Luborsky F. E.: *Application oriented magnetic properties*. In: *Amorphous Metallic Alloys* (ed.: Luborsky F. E.) Butterworths Monographs in Materials, London, 1984. 360–379.
- [4] Tsai M. H., Yeh J. W.: *High-entropy Alloys: A Critical Review*. Materials Research Letters, 2/3. (2014) 107–123.  
<https://doi.org/10.1080/21663831.2014.912690>
- [5] Inoue A.: *Stabilization of Metallic Supercooled Liquid and Bulk Amorphous Alloys*. Acta Materialia, 48/1. (2000) 279–306.  
[https://doi.org/10.1016/S1359-6454\(99\)00300-6](https://doi.org/10.1016/S1359-6454(99)00300-6)
- [6] Kauzman W.: *The Nature of the Glassy State and the Behavior of Liquids at Low Temperatures*. Chemical Reviews, 43/2. (1948) 219–256.  
<https://doi.org/10.1021/cr60135a002>
- [7] Angell C. A.: *Structural instability and relaxation in liquid and glassy phases near the fragile liquid limit*. Journal of Non-Crystalline Solids, 102/1–3. (1988) 205–221.  
[https://doi.org/10.1016/0022-3093\(88\)90133-0](https://doi.org/10.1016/0022-3093(88)90133-0)
- [8] Köster U., Janlewing R.: *Fragility parameter and nanocrystallization of metallic glasses*. Materials Science and Engineering: A, 375–377 (2004) 223–226.  
<https://doi.org/10.1016/j.msea.2003.10.083>
- [9] Inoue A.: *Bulk Amorphous Alloys*. In: *Non-Equilibrium Processing of Materials* (ed.: Suryanarayana C.) Pergamon Materials Series, Pergamon Amsterdam–Lausanne–New York, 1999. 375–415.
- [10] Dimitrov V. I.: *Theory of Fluidity of Liquids, Glass*

- Transition and Melting*. Journal of Non-Crystalline Solids, 352/3. (2006) 216–231.  
<https://doi.org/10.1016/j.jnoncrysol.2005.11.026>
- [11] Lovas A., Ramasamy P. Kováč J., Novák L., Szabó A., Eckert J.: *Cluster-related phenomena in the properties and transformations of transition metal-based glassy alloys*. Metals, 10/8. (2020) 1025.  
<https://doi.org/10.3390/met10081025>
- [12] Richardson F. D.: *Physical Chemistry of Melts in Metallurgy*. Academic Press London, New York, 1. (1974) 142.
- [13] Predel B.: *Thermodynamic stability of amorphous alloys*. Key Engineering Materials, 40–41. (1990) 17–38.
- [14] Debenedetti P. G.: *Metastable Liquids Concepts and Principles*. Princeton Univ. Press, Princeton, 1996.
- [15] Debenedetti P. G., Stillinger F. H.: *Supercooled liquids and the glass transition*. Nature, 410/8. (2001) 259–267.  
<https://doi.org/10.1038/35065704>
- [16] Zhang F., Zhang C., Chen S. L., Zhu J., Cao W. S., Kattner U.R.: *An understanding of high entropy alloys from phase diagram calculations*. CALPHAD, 45. (2014) 1–10.  
<https://doi.org/10.1016/j.calphad.2013.10.006>
- [17] Tropearevsky M. C., Morris J. R., Daene M., Wang Y., Lupini A. R., Malcolm G.: *Beyond Atomic Sizes and Hume-Rothery Rules: Understanding and Predicting High-Entropy Alloys*. JOM, 67. (2015) 2350–2363.  
<https://doi.org/10.1007/s11837-015-1594-2>
- [18] Barnard A. K., Sykes P.: *Theoretical Basis of Inorganic Chemistry*. New York (N.Y.): McGraw-Hill, 1965.
- [19] Khandelwal B. L.: *Inorganic Chemistry of Transition Elements*. Disha Institute of Management and Technology, Raipur, 2007.
- [20] Miedema A. R., Boom R., De Boer F. R.: *On the heat of formation of solid alloys*. J. Less-Common Met. 41 (1975) 275–284.

# Modeling the Deformation and the Failure Process of Glass Woven Fabrics Based on the Fibre-Bundle-Cells Theory

Ábris Dávid VIRÁG,<sup>1</sup> László Mihály VAS,<sup>2</sup> Kolos MOLNÁR<sup>3</sup>

<sup>1</sup> *Budapest University of Technology and Economics, Faculty of Mechanical Engineering, Department of Polymer Engineering, Budapest, Hungary, viraga@pt.bme.hu*

<sup>2</sup> *Budapest University of Technology and Economics, Faculty of Mechanical Engineering, Department of Polymer Engineering, Budapest, Hungary, vas@pt.bme.hu*

<sup>3</sup> *Budapest University of Technology and Economics, Faculty of Mechanical Engineering, Department of Polymer Engineering, Budapest, Hungary and MTA–BME Research Group for Composite Science and Technology, Budapest, Hungary, molnar@pt.bme.hu*

---

## Abstract

In this study, we modeled the deformation and failure behavior of different glass woven fabrics under uni-axial tension using the Fibre Bundle Cells-modeling method. The difference between the analytical, phenomenological model curve and the mean curve calculated from the measurement results was classified by the relative mean squared error (RMSE), which is closely related to the coefficient of determination. This value was less than 3.6% in all the examined cases, which indicated good modeling.

**Keywords:** *FBC modeling, glass woven, tensile test.*

---

## 1. Introduction

Nowadays, the application fields of polymer composites are constantly expanding, and in addition to fiber-reinforced polymer composites [1] research on nano- [2], and biocomposites [3], as well as on the destruction of composite structures [4], is gaining prominence. The high use of polymer composites is well illustrated by the fact that more than 50% of the raw materials used in aircraft manufacturing are polymer composites (excluding engines) [5].

A significant part of these are fabric-reinforced composites, hence there is a huge demand for models which can properly describe the mechanical and failure behavior of fabrics and fabric-reinforced composite materials and products already in the design phase. However, this requires fabric models that allow a sufficiently accurate description of the mechanical behavior of the fabrics. Continuous or discrete element models are basically used to model the behavior of woven fabrics.

### 1.1. Continuum models

Most woven fabric models are continuum models that treat fabric as a continuum material. Traditionally, layer models of composite mechanics are used to model fabrics. In order to describe the fabric-reinforced composites more accurately, several analytical and finite element 2D and 3D models have been developed that already take into account the fibrous structure of the fabrics and the structure resulting from the weaving technology. Examples are the mosaic model developed by Ishikawa [6], and the fiber undulation model [7]. The mosaic model first divides the fabric into two layers perpendicular to each other and then separates the warp and weft yarns within the layers. The fiber undulation model takes into account the continuity, the unevenness of the yarns and the intersection of warp and weft yarns as well. It describes the fabric with a repeating unit consisting of three parts: a two-layer element where the two layers are oriented perpendicularly (which is also used at the yarn intersections of the mosaic model), a corrugated element (which describes the

actual intersection of warp and weft yarns), and an element assuming pure matrix material. Later, 2D and 3D modeling have developed from these basic models, and the models applied today can be used to describe time- and temperature-dependent behaviors as well [8].

## 1.2. Discrete element models

Discrete element models define fabric as a network of a finite number of nodes (typically mass points), and nodes are usually connected by mechanical elements with specific properties (e.g., springs, dashpots, etc.). One such model is based on a network of springs and dashpots connected in parallel by Gräff and Kuzmina [9]. In the model, discrete points of mass are connected by different springs (structural, bending and shear). However, these are not simple springs, but essentially Kelvin-Voigt elements (since the spring branches also contain dashpots). The model considers the springs to have a linear characteristic and the dashpots to be proportional to the speed, while not taking into account the friction between the yarns.

Another discrete element model suitable for describing woven fabrics is the Vas's fiber bundle cell model [10, 11]. The Fiber Bundle Cell-based modeling method offers a set of model elements that can be used to build a system for describing the behavior of fibrous structures and composites reinforced with fibrous structures. The Fiber Bundle Cell model is a discrete element model that takes into account that the fabric used as a composite reinforcement is not a continuum structure. The model also considers that the yarns (as fibers) that constitute the fabric form fiber bundles (fiber bundle cells) at the microscopic level. When describing fabrics, the model considers the warp and weft yarns of the fabric as fiber bundles. At the macroscopic level, it describes woven fabrics as a concentrated parameter network of mechanical elements (fiber bundle cells) with discrete, statistical, linear, or nonlinear characteristics. The model assumes that the fibers in a partially ordered fiber bundle of the same type of fibers can be classified based on their initial state and environmental properties (gripping conditions) and can be shifted along with their environment (or into a similar environment). Fibers in the same classes form a sub-fiber bundle (i.e. a fiber bundle cell). The system of fiber bundle cells produced in this way, parallel to the direction of stretching, models the structure and strength of the original bundle.

## 2. The applied model

In the model, the real fabric of warp and weft yarns was replaced by a model with only warp yarns. This was possible because during the warp direction strip tensile tests, the weft yarns essentially do not take up the load, only modify the spatial arrangement and deformation behavior of the warp yarns. Therefore, a model bundle is required whose elements are virtual warp yarns that also include the effect of weft yarns. For  $0^\circ$  specimens, "strong" model yarns are obtained. This step can also be done for  $45^\circ$  specimens, but in this case there is no yarn in the direction of the load. Therefore, as a result of waviness and obliquity modifying the deformation behavior, "weak" (warp) model yarns are obtained.

### 2.1. Modeling with one nonlinear E-bundle

A nonlinear E-bundle from the model set was used to model the tensile tests on the  $0^\circ$  fabric bands. The E-bundle is a well-arranged, elastic, breaking bundle with independent fibers, ideal grips at both ends (i.e., the fibers do not slip out of the grip and do not break in the grip), the fibers are parallel to each other and to the direction of pulling and are not pre-stressed (i.e. they are stress-free but not loose). In this case, the tensile characteristic ( $f(\varepsilon)$  ( $\text{N}\cdot\text{g}^{-1}\cdot\text{m}^2$ )) is described by Equation (1), where  $\varepsilon$  denotes the relative elongation,  $a > 0$  ( $\text{N}\cdot\text{g}^{-1}\cdot\text{m}^2$ ),  $b > 0$  ( $\text{N}\cdot\text{g}^{-1}\cdot\text{m}^2$ ) are the parameters representing the influence of the waviness of the yarn and the wrinkling of the woven strip on the tensile characteristic, and  $c > 0$  ( $\text{N}\cdot\text{g}^{-1}\cdot\text{m}^2$ ) is the asymptotic tensile stiffness:

$$f(\varepsilon) = c\varepsilon + a(1 - e^{-b\varepsilon}) \quad (1)$$

It can be seen that for  $a = 0$  and/or  $b = 0$ , Equation (1) also includes the linear case. However, Equation (1), like the tensile characteristics in general, only describes the intact operation, which can be determined for most mechanical models. Fiber bundle cell-based modeling, on the other hand, assumes that there are defects in the test material. These are considered with a so-called reliability function ( $g(\varepsilon)$ ) (2), where  $\varepsilon$  is the specific elongation of the model yarn,  $\varepsilon_S$  is the specific elongation at break of the model yarn, and  $Q_{\varepsilon_S}$  is the distribution function of the specific elongation at break:

$$g(\varepsilon) = (1 - Q_{\varepsilon_S}(\varepsilon)) \quad (2)$$

In this case, the reliability function is a complementary distribution function of the specific elongation at break. The reliability function gives

the ratio of the still operating, i.e. intact fibers at the given load level ( $\varepsilon$ ). In the present case, we assumed the specific elongation at break ( $\varepsilon_b$ ) of the model yarns to be normally distributed. Using equations (1) and (2), the tensile stress  $\sigma(\varepsilon)$  can be produced as the product of the tensile characteristic  $f(\varepsilon)$  and the reliability function  $g(\varepsilon)$  (3), which significantly reduces the operation of the calculations for more complex calculations:

$$\sigma(\varepsilon) = f(\varepsilon) \cdot g(\varepsilon) \quad (3)$$

## 2.2. Modeling with two nonlinear E-bundles connected in parallel

Two parallel-connected nonlinear E-bundles were used in each case to model the mean curves describing the deformation and failure behavior of 45 ° angled woven strips under uniaxial tension. The use of the two bundles was necessary due to the shape of the curves, as a very inaccurate result would have been obtained with a single bundle model. The two-bundle case is very similar to the single bundle case, however, the tensile characteristic is described not by Equation (1) but by Equation (4), where  $p_1$  and  $p_2$  are weights for which it is true that  $p_1 + p_2 = 1$ :

$$f(\varepsilon) = p_1 \cdot f_1(\varepsilon) + p_2 \cdot f_2(\varepsilon) \quad (4)$$

where the characteristic of each bundle is (5):

$$f_i(\varepsilon) = \begin{cases} c_i \cdot (\varepsilon - d_i) + a_i(1 - e^{-b_i(\varepsilon - d_i)}), & \text{if } \varepsilon \geq d_i \\ 0, & \text{if } \varepsilon < d_i \end{cases} \quad (5)$$

where  $i \in \{1, 2\}$ , } and  $d$  is an offset that is zero in one or both cases. It can be seen that Equation (5) also includes the single bundle case, where  $d = 0$ . In the two-bundle case, for example, for one bundle  $d > 0$ , and for the other  $d = 0$ . Thus, in the two-bundle case, the tensile characteristic has four parameters. In this case the specific tensile stress also can be obtained as the weighted sum of the product of the tensile characteristic and the reliability function on the two nonlinear bundles  $E(E_1$  and  $E_2)$  :

$$\begin{aligned} \sigma(\varepsilon) &= \sigma_{E_1}(\varepsilon) + \sigma_{E_2}(\varepsilon) \\ &= p_1 \cdot \sigma_1(\varepsilon) + p_2 \cdot \sigma_2(\varepsilon) \\ &= p_1 \cdot f_1(\varepsilon) \cdot g_1(\varepsilon) + p_2 \cdot f_2(\varepsilon) \cdot g_2(\varepsilon) \end{aligned} \quad (6)$$

## 3. Materials and methods

In the research, UTE195P from the manufacturer Unique Textiles (area density: 195 g/m<sup>2</sup>, weave: plain) and UTE195T (area density: 195 g/m<sup>2</sup>, weave: twill) glass fabrics were tested. Warp-directional and  $\pm 45^\circ$  samples were prepared from the woven fabrics, with a width and length of 50 and 200 mm, respectively. Uniaxial tensile testing

of the samples was performed on a universal tensile machine (manufacturer: Zwick, type: Z005). The grip length was 100 mm and the test speed was 25 mm/min, during the test, the force and the crosshead displacement were recorded. FBC modeling was performed based on tensile tests. The five force-crosshead displacement curves were first parameterized to the specific stress (ratio of the measured force and the area density of the specimen) – specific elongation (ratio of the actual and initial clamping length of the specimen) curve, and then determined in each case by the so-called smoothed mean curve (this was obtained by moving average smoothing, where the width of the smoothing window was  $\varepsilon = 0.01$ ). The resulting mean curves were used for modeling. Using Equations (1) - (6), we performed the FBC modeling for the total specific stress -specific elongation curve. The model parameters ( $a_p$ ,  $b_p$ ,  $c_p$ ,  $d_p$  and  $p_i$ ) in Equations (1) and (5) were optimized by an iteration method, so that the difference between the model curve and the mean curve should be optimized to get a minimum RMSE value (Eq. 7), which is closely related to the coefficient of determination:

$$RMSE = \sqrt{\frac{1}{n} \cdot \sum_{i=1}^n (\sigma_{measured}(\varepsilon_i) - \sigma(\varepsilon_i))^2} \quad (7)$$

where  $n$  is the number of measuring points,  $\sigma_{measured}$  is the specific stress calculated from the measured force values, and  $\varepsilon_i$  is the elongation value corresponding to the stress measured at the given point.

## 4. Results and discussion

The specific stress ( $\sigma$ )-specific elongation ( $\varepsilon$ ) curves calculated from the tensile tests for the tested woven fabrics are shown in [Figures 1-4](#). In the figures, the dashed line indicates the smoothed mean curve required for the modeling.

The curves show that there is no significant difference between the force maxima of the test specimens of the same size but with different weaves in the warp direction. However, in the case of  $\pm 45$  degrees, there is an order of magnitude difference. Since there is no yarn in the direction of the load in this test, the maximum force is determined by the weave of the fabrics, since all their other parameters are the same. These measurement results also prove that twill weaving results in a much looser structure, which also implies that it is much easier to transform into

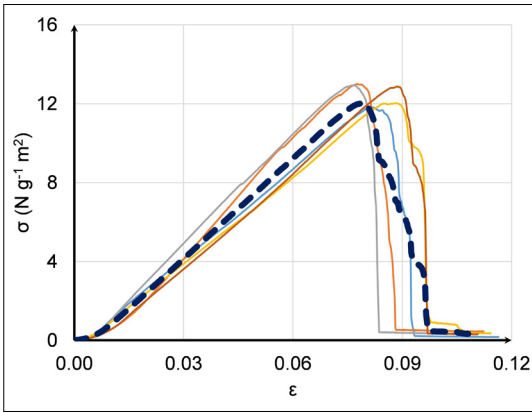


**Figure 1.** Warp directional tensile curves and the smoothed mean curve (dashed line) of plain fabric.

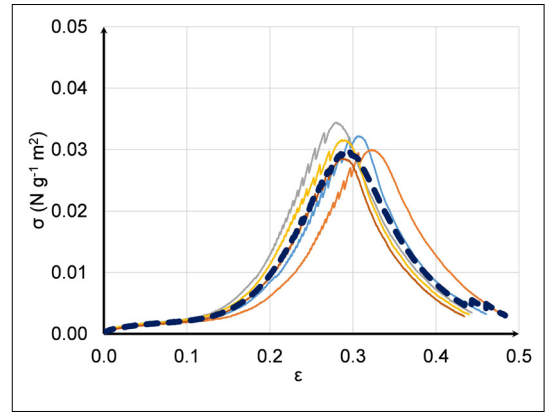


**Figure 3.**  $\pm 45^\circ$  directional tensile curves and the smoothed mean curve (dashed line) of plain fabric.

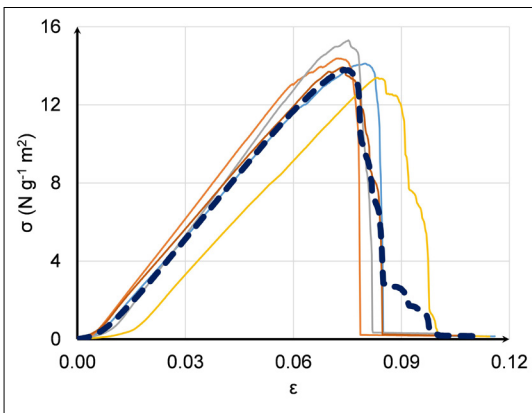


**Figure 2.** Warp directional tensile curves and the smoothed mean curve (dashed line) of twill fabric.

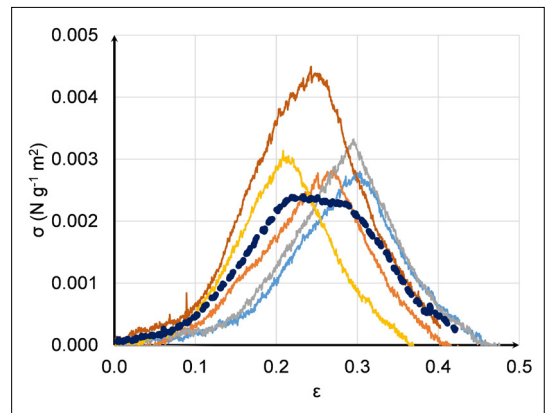


**Figure 4.**  $\pm 45^\circ$  directional tensile curves and the smoothed mean curve (dashed line) of twill fabric.

complex 3D shapes. Of course, this difference also occurs in the mechanical properties when used as an embedded reinforcement. The relationship between the smoothed mean curves determined from each measurement curve and the modeled curves is shown in **Figures 5–8**.

The quantified results of the modeling are shown in **Table 1**. In the table, parameters  $a$ ,  $b$ ,  $c$ ,  $d$  are the variables in Equations (1) and (5), and  $E(\varepsilon_s)$ ,  $D(\varepsilon_s)$  and  $V(\varepsilon_s)$  are the expected value, standard deviation, and relative standard deviation, respectively. To characterize the relationship between the model curves and the smoothed mean curves, i.e. to determine the goodness of the modeling, we used the relative mean squared error (RMSE).

It can be seen from **Table 1**, that the relative mean squared error between the smoothed mean

curve and the curve calculated by the Fiber Bundle Cell theory is less than 3.6% in every case. Based on these results, the modeling can be considered exceptionally good, as the modeled curve approximates the smoothed mean curve well enough.

## 5. Conclusions

Using the Fiber Bundle Cell theory, we created a discrete element, analytical, phenomenological model suitable for the mechanical modeling of the deformation and failure behavior of the investigated composite reinforcing fabrics during uniaxial tensile testing. The relative mean squared error between the smoothed mean curve determined from 5 tensile tests per material and the curve calculated from the model was less than 3.6% in each case.

**Table 1.** Parameters characterizing the modeling of woven fabric strips

| Sample and grip |                    |                    | MODEL PARAMETERS       |  |                                    |                                    |     |                 |                 |                     |          |
|-----------------|--------------------|--------------------|------------------------|--|------------------------------------|------------------------------------|-----|-----------------|-----------------|---------------------|----------|
|                 |                    |                    | Model-structure        | Tensile characteristics - intact functioning |                                    |                                    |     | Failure         |                 |                     | Fitting  |
| Sam-ple         | Grip distance (mm) | Azi-muth angle (°) | Com-ponent weight, $p$ | $a$ ( $N \cdot g^{-1} \cdot m^2$ )           | $b$ ( $N \cdot g^{-1} \cdot m^2$ ) | $c$ ( $N \cdot g^{-1} \cdot m^2$ ) | $d$ | $E(\epsilon_s)$ | $D(\epsilon_s)$ | $V(\epsilon_s)$ (%) | RMSE (%) |
| Plain           | 100                | 0                  | 1.00                   | -220   | 1.5                                | 330                                | 0   | 0.09            | 0.008           | 9.0                 | 3.05     |
| Twill           | 100                | 0                  | 1.00                   | -267   | 1.5                                | 400                                | 0   | 0.08            | 0.006           | 7.1                 | 3.49     |
| Plain           | 100                | 45                 | 0.40                   | 0.3  | 2.0                                | 0.08                               | 0   | 0.44            | 0.033           | 7.5                 | 2.10     |
|                 |                    |                    | 0.60                   | -8.3   | 0.1                                | 0.92                               | 12  | 0.33            | 0.033           | 10.0                |          |
| Twill           | 100                | 45                 | 0.12                   | 0.3  | 0.5                                | 0.01                               | 0   | 0.34            | 0.063           | 18.5                | 3.59     |
|                 |                    |                    | 0.88                   | -0.6   | 0.1                                | 0.06                               | 6   | 0.29            | 0.063           | 21.7                |          |

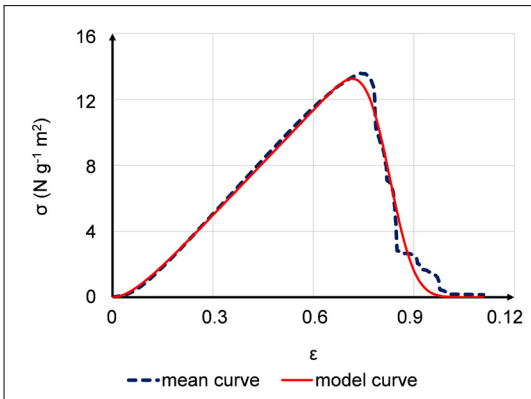


**Figure 6.** Warp directional mean curve and model curve of twill fabric obtained from tensile tests.

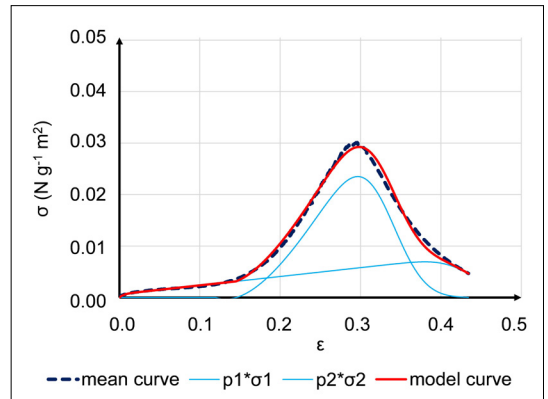


**Figure 7.**  $\pm 45^\circ$  directional mean curve and model curve of plain fabric obtained from tensile tests.

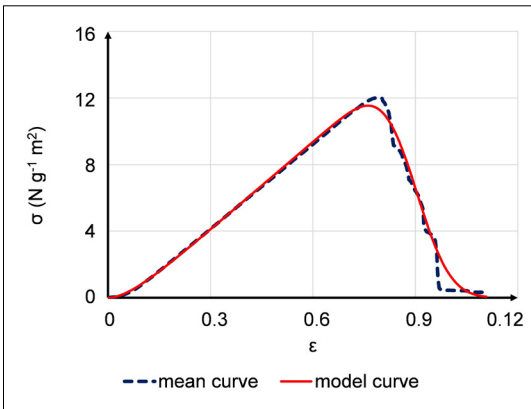


**Figure 5.** Warp directional mean curve and model curve of plain fabric obtained from tensile tests.

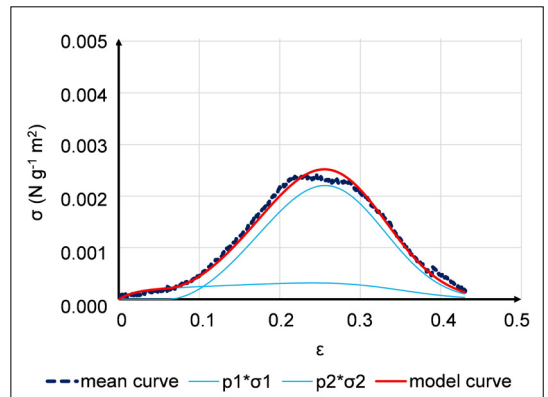


**Figure 8.**  $\pm 45^\circ$  directional mean curve and model curve of twill fabric obtained from tensile tests.

Based on the results, the modeling method is proven to be exceptionally good. It can be stated that the FBC modeling is a fast, simple method with a small computing capacity, which is suitable for describing the deformation and failure behavior of fabrics under uniaxial tension.

### Acknowledgements

This research was supported by the ÚNKP-20-3 and ÚNKP-20-5 New National Excellence Program of the Ministry for Innovation and Technology. The research reported in this paper and carried out at BME has been supported by the NRD Fund (TKP2020 NC, Grant No. BME-NC) based on the charter of bolster issued by the NRD Office under the auspices of the Ministry for Innovation and Technology.

### References

- [1] Rajak D. K., Pagar D. D., Menezes P. L., Linul E.: *Fiber-Reinforced Polymer Composites: Manufacturing, Properties, and Applications*. Polymers, 11/10. (2019) 1667.  
<https://doi.org/10.3390/polym11101667>
- [2] Singh R., Shrivastava A. K., Bajpai A. K.: *CdSe reinforced polythiophene nanocomposites as excellent materials for diode applications*. eXPRESS Polymer Letters, 15/1. (2021) 45–57.  
<https://doi.org/10.3144/expresspolymlett.2021.6>
- [3] Akintayo O. S., Olajide J. L., Betiku O. T., Egho A. J., Adegbesan O. O., Daramola O. O., Sadiku E. R., Desai D. A.: *Poly(lactic acid)-silkworm silk fibre/fibroin bio-composites: A review of their processing, properties, and nascent applications*. eXPRESS Polymer Letters, 14/10. (2020) 924–951.  
<https://doi.org/10.3144/expresspolymlett.2020.76>
- [4] Takács L., Szabó F.: *Experimental and Numerical Failure Analysis of Adhesive Joint of Glass Fiber Reinforced Polymer Composite*. Periodica Polytechnica Mechanical Engineering, 64/1. (2020) 88–95.  
<https://doi.org/10.3311/PPme.15106>
- [5] 1001Crash.com: *Worries about new composite made airplane*, 2011. (letöltve: 2021. február 17.).  
<http://www.1001crash.com/index-page-composite-lg-2.html>
- [6] Ishikawa T.: *Anti-symmetric Elastic Properties of Composite Plates of Satin Weave Cloth*. Fiber Science and Technology, 15/2. (1981) 127–145.  
[https://doi.org/10.1016/0015-0568\(81\)90066-X](https://doi.org/10.1016/0015-0568(81)90066-X)
- [7] Ishikawa T., Chou T. W.: *One-dimensional Micro-mechanical Analysis of Woven Fabric Composites*. AIAA, 21/12. (1983) 1714–1721.  
<https://doi.org/10.2514/3.8314>
- [8] Shrotriya P., Sottos N. R.: *Viscoelastic Response of Woven Composite Substrates*. Composites Science and Technology, 65/3–4. (2005) 621–634.  
<https://doi.org/10.1016/j.compscitech.2004.09.002>
- [9] Gräff J., Kuzmina J.: *Cloth Simulation Using Mass and Spring Model*. In: Material Science. Mechanical Engineering 2004. Proceeding of 4<sup>th</sup> Conference on Mechanical Engineering, Budapest, Hungary, Budapest, BUTE, (2004) 443–447.
- [10] Vas L. M.: *Idealizált statisztikus szálkötegcéllák és alkalmazásuk szálas szerkezetek, kompozitok modellezésére*. MTA doktori értekezés (2007).
- [11] Vas L. M., Tamás P.: *Modelling Method Based on Idealised Fibre Bundles*. Plastics, Rubber and Composites, 37/5–6. (2008) 233–239.  
<https://doi.org/10.1179/174328908X309411>